

https://dspace.org/

Synthesis and characterization of Cu-based telluride semiconductor materials for application in photovoltaic cells

Ntholeng, Nthabiseng

2017

http://hdl.handle.net/10539/23532

Ntholeng, Nthabiseng (2017) Synthesis and characterization of Cu-based telluride semiconductor materials for application in photovoltaic cells, University of the Witwatersrand, Johannesburg, <http://hdl.handle.net/10539/23532>

Downloaded from a DSpace repository. https://dspace.org/

Synthesis and characterization of Cu-based telluride semiconductor materials for application in photovoltaic cells

By

Nthabiseng Ntholeng

Submitted to the Faculty of Science,

School of Chemistry at University of the Witwatersrand, in partial fulfilment of the requirements for the degree of

Doctor of Philosophy

Supervisor: Prof Nosipho Moloto

DECLARATION

I declare that the study titled "Synthesis and characterization of Cu-based telluride semiconductor materials for application in photovoltaic cells is my own, unaided work submitted for the degree Doctor of Philosophy in the University of the Witwatersrand, Johannesburg. It has not been submitted for any degree or examination in any other University, and all sources used or quoted here have been indicated and acknowledged by means of references.

Name: Nthabiseng Ntholeng (Ms) Date: 05 June 2017

Signature: 

Abstract

The colloidal method has extensively been used to synthesize ternary and quaternary copper sulfides and selenides. Although tellurides form part of the chalcogenides, little has been reported on them particularly the synthesis of these nanostructures. Achieving high-quality nanocrystals through colloidal synthesis requires thorough monitoring of parameters such as time, solvent, precursor as they affect nucleation and growth of the nanocrystals. Herein, we report on the colloidal synthesis of ternary $CuInTe_2$ and quaternary $CuIn_{1-x}Ga_xTe_2$ nanostructured semiconductor materials. A typical synthesis of $CuInTe_2$ entailed varying reaction temperature. At temperatures below 250 °C, no formation of $CuInTe_2$ was seen. At 250 °C formation of $CuInTe_2$ could be observed with the formation of binary impurities. A change in the sequence in which precursors were added at 250 °C yielded pure $CuInTe_2$. Applying different surfactants aided in achieving differently structured morphologies of $CuInTe_2$ nanocrystals. Morphology varied from rods, cubes, nanosheets etc. Different morphologies resulted in different optical properties with the high optical band gap of 1.22 eV measured for 1D rods. Different precursors were employed in the synthesis of quaternary $CuIn_{1-x}Ga_xTe_2$. Precursor 2 (entailed the use of Cu $(acac)_2$, In $(acac)_3$ and $Ga(acac)_3$) yielded pure $CuIn_{1-x}Ga_xTe_2$ phase with no formation of impurities. Variation in reaction time influenced the optical properties of the quaternary $CuIn_{1-x}Ga_xTe_2$ with high band gap obtained at low reaction time (30 min). A change in Ga and In concentration resulted in reduced lattice parameters ***a*** and ***c*** with lowest values obtained with the highest Ga concentration. However, achieving the intended concentration proved challenging due to the loss of the material during synthesis. Increasing the Ga concentration resulted in a high optical band gap. Conducting the reaction with Hexadecylamine (HDA) resulted in a relatively high optical band though the formation of impurities was evident. The obtained band gap can be attributed to small sized particles as evident from TEM results.

Heterojunction ZnO/CIT and ZnO/CIGT solar cell devices were fabricated through a simple solution approach. The performance of ZnO/CIGT device was superior to that of ZnO/CIT in which efficiency increased from 0.26-0.78%. In the ZnO/CIT device, high V_{oc} of 880 mV was recorded while 573.66 mV was measured for ZnO/CIGT device. Chemical and thermal treatments were performed on the ZnO/CIGT devices. The efficiency increased from 0.78-1.25% when the device was chemically treated with a short-chain EDT ligand. A high conversion efficiency of 2.14% was recorded for devices annealed at 300 °C. High annealing temperatures resulted in poor device performance with the lowest efficiency of 0.089% obtained at annealing temperatures of 500 °C attributed to the leaching out of In and Ga into the ZnO layer.

DEDICATION

TO MY LATE MOTHER THAKANE SHEILA NTHOLENG

Acknowledgements

I would like to thank my supervisor Professor Nosipho Moloto for her advice and guidance in this research. I am grateful to NRF for funding the project. I also thank the School of Chemistry, University of the Witwatersrand and the University of Manchester for giving me the opportunity to conduct this research in their premises. Thanks also go to the MMU and XRD facilities at Wits.

Table of Contents

Declaration ii
Abstract iii
Dedication iv
Acknowledgements v
Chapter 1: Introduction 1
1.1 Motivation and rationale 1
1.2 Aims and objectives of the study 3
1.3 References 4
Chapter 2: Literature Review 5
2.1 Introduction 5
2.2 Copper chalcogenide semiconductor materials 6
2.3 Synthesis of Copper chalcogenide semiconductor materials 8
2.3.1 Colloidal synthesis: nucleation and growth of nanocrystals 9
2.3.1.1 Nucleation process 9
2.3.1.2 Growth process 12
2.3.2 Shape and morphology of nanocrystals 14
2.4 Optical properties 19
2.5. Photovoltaic applications 22
2.6 References 26
Chapter 3: Colloidal synthesis of pure $CuInTe_2$ crystallites based on the HSAB theory 32
3.1 Introduction 32
3.2 Experimental 34
3.2.1 Materials and reagents 34
3.2.2 Synthesis of $CuInTe_2$ 34
3.2.3 Characterization 35
3.3 Results and discussion 35
3.1 Effect of temperature on the formation of $CuInTe_2$ 35
3.1.1 XRD studies. 35
3.1.2 Raman studies. 37
3.1.3 Microscopy analysis at various reaction temperatures 39
3.2 Effect of order of precursor addition 41
3.2.1 XRD studies 41
3.2.2 Raman studies 43
2.2.3 Optical analysis. 45

3.2.4 Morphological analysis. 48
3.3 The proposed reaction path for the formation of phase pure $CuInTe_2$ 51
3.4 Conclusions 54
3.5 References 55
Chapter 4: Morphology and shape engineering of $CuInTe_2$ nanostructured semiconductor material 58
4.1 Introduction 58
4.2 Experimental section 63
4.2.1 Materials and reagents 63
4.2.2 Synthesis of $CuInTe_2$ 64
4.2.3 Characterization 64
4.3 Results and discussions 65
4 3.1 Effect of coordinating ligands on morphology 65
4 3.2 Effect of reaction time on morphology 77
4.3.3 1D to 2D shape evolution mechanism 84
4.4 Conclusions 88
4.5 References 89
Chapter 5: Time, precursor, surfactant and stoichiometry dependency of quaternary $CuIn_{1-x}Ga_xTe_2$ nanostructured semiconductor materials 92
5.1 Introduction 92
5.2 Experimental section 96
5.2.1 Materials 96
5.2.2 Synthesis Procedure 96
5.2.3 Characterization 97
5.3 Results and discussion 98
5.3.1 The effect of incorporating gallium 98
5.3.1.1 Structural properties 98
5.3.1.2 Morphological properties 100
5.3.1.3 Raman analysis 101
5.3.1.4 Optical properties 102
5.3.2 The effect of metal precursors 104
5.3.2.1 Structural properties 106
5.3.2.2 Optical properties 108
5.3.3.2 Morphological properties 111
5.3.3 The effect of reaction time on CIGT synthesized using precursor 2 112
5.3.3.1 Structural properties 112

5.3.3.2 Optical properties 114
5.3.3.2 Morphological properties 117
5.3.4 The effect of stoichiometry variation 119
5.3.4.1 Structural properties 119
5.3.4.2 Optical properties 124
5.3.4.3 Morphological properties 127
5.3.5 The effect of capping agent 130
5.3.5.1 Structural and morphological properties 130
5.3.4.2 Optical properties 132
5.3.4.3 Morphological properties 134
5.4 Conclusions 136
5.5 References 138
Chapter 6: Heterojunction ZnO/CIT and ZnO/CIGT solar cells 143
6.1 Introduction 143
6.2 Experimental 146
6.2.1 Materials 146
6.2.2 Fabrication of the hybrid solar cells 146
6.2.3 Characterization 147
6.3 Results and discussion 148
6.3.1 Optical properties of sol-gel ZnO thin films 148
6.3.2 Cyclic voltammetry measurements 149
6.3.3 Photovoltaic properties of CIT solar cell device 151
6.3.4 The effect of chemical surface treatment on the $CIGTe_2$ solar cell devices 153
6.4 The effect of thermal treatment on the $CIGTe_2$ thin films 158
6.5 Conclusions 162
6.6 References 164
Chapter 7: Conclusions and Recommendation 168
7.1 Conclusions 168
7.2 Recommendations 170

List of Figures

Figure 2.1: Crystal structures of ternary and quaternary Cu chalcogenide NCs……8

Figure 2.2: The La Mer model of nucleation, where a critical reactant concentration is required for particle nucleation. 10

Figure 2.3: Growth rate dependency on the nanoparticle size for low and high monomer concentration. 13

Figure 2.4: Schematic illustrations showing the role of capping agents in directing the growth of a single-crystal seed made of an fcc metal. 15

Figure 2.5: 1D: nanorods, nanoshuttles, nano bipyramids, nanowires and nanotubule. 2D nanoparticles: triangular nanoplate, nanodisk, ribbons and belts. 3D nanoparticles: nanocubes, tetrapods, star-shaped, nanohexapods and nanocage 16

Figure 2.6: A comparison of the electronic energy states of different types of semiconductor materials 19

Figure 2.7: Possible recombination pathways in$CuInS_2$ nanocrystals.. 21

Figure 2.8: Schematic cross-section of a traditional inorganic solar cell..... 23

Figure 2.9: Quantum-dot-sensitized solar cells with CIS NCs as sensitizers. 24

Figure 3.1: XRD patterns of crystallites synthesized using method 1 at various temperatures ..... ……36

Figure 3.2: Raman spectra of crystallites synthesized using method 1 at various temperatures. 38

Figure 3.3: TEM micrographs of crystallites synthesized using method 1 at 250 °C. 40

Figure 3.4: XRD patterns of $CuInTe_2$ crystallites synthesized at 250 °C using method 1 and 2, ... 42

Figure 3.5: Raman spectra of $CuInTe_2$ crystallites synthesized at 250 °C using method 1 and 2. 44

Figure 3.6: UV–Vis–NIR absorbance spectra and optical bands (insets) gaps of $CuInTe_2$ crystallites synthesized at 250 °C using method 1 and 2 46

Figure 3.7: TEM and HRTEM micrographs of $CuInTe_2$ crystallites synthesized at 250 °C using method
2……49

Figure 3.8: TEM and HRTEM micrographs of $CuInTe_2$ crystallites synthesized at 250 °C using method 1. 50

Figure 3.9: EDS spectra of TEM and HRTEM micrographs of $CuInTe_2$ crystallites synthesized at 250 °C using method 2 and method 1. 51

Figure 3.10: Proposed reaction path for the formation of phase pure $CuInTe_2$…….. 53

Figure 4.1: Schematic illustration of the nucleation and growth process of nanocrystals. 59

Figure 4.2: Temporal evolution of the size distribution of CdSe NCs prepared by a hot injection method and illustration of the focusing and defocusing of size distribution 61

Figure 4.3: Shape control of colloidal nanocrystals. 63

Figure 4.4 Scheme of the different capping agent molecules and their functionalities. 67

Figure 4.5: TEM micrographs of $CuInTe_2$ synthesized at 250 °C using various capping agents. 69

Figure 4.6: XRD patterns of $CuInTe_2$ synthesized at 250 °C using various capping agents 71

Figure 4.7: Schematic diagram of the band structure of chalcopyrite with modified d levels to fit the ordering levels in $CuInTe_2$ 73

Figure 4.8: UV–Vis–NIR absorbance spectrum and optical band gap of $CuInTe_2$ crystallites synthesized at 250 °C using various capping agents..... 75

Figure 4.9: Morphology transition from 1D to 2D Shape of $CuInTe_2$ with increasing reaction time... 79

Figure 4.10: Morphology transition from 1D to 2D Shape of $CuInTe_2$ with increasing reaction time. 81

Figure 4.11: XRD patterns of $CuInTe_2$ synthesized at temperature 250 °C and various reaction. 82

Figure 4.12: UV–Vis–NIR absorption spectra and optical band gap of $CuInTe_2$ crystallites synthesized at temperature 250 °C at various reaction times. 83

Figure 4.13: The proposed self-ripening mechanism of 1D to 2D morphology transformation……87

Figure 5.1: Schematic illustration of anion displacement and tetragonal distortion……..... 93

Figure 5.2: Schematic diagram of experimental set-up 97

Figure 5.3: XRD patterns of $CuInTe_2$ and $CuIn_{1-x}Ga_xTe_2$ at 250 °C with inset of an expanded view of (111) peak. 99

Figure 5.4: TEM micrographs of $CuInTe_2$ and $CuInGaTe_2$ semiconductor materials synthesized at 250 °C. 101

Figure 5.5: Raman spectra of $CuInTe_2$ and $CuIn_{1-x}Ga_xTe_2$ materials synthesized at 250 °C. 102

Figure 5.6: Absorbance spectra of $CuInTe_2$ and $CuIn_{0.8}Ga_{0.2}Te_2$ materials synthesized at 250 °C. ... 104

Figure 5.7: XRD patterns of $CuIn_{1-x}Ga_xTe_2$ synthesized with Precursor 1 and Precursor 2. 107

Figure 5.8: UV-Vis absorption spectra of $CuIn_{0.84}Ga_{0.16}Te_2$ synthesized with Precursor 1 and $CuIn_{0.25}Ga_{0.75}Te_2$ with Precursor 2 110

Figure 5.9: PL emission spectra of $CuIn_{0.84}Ga_{0.16}Te_2$ synthesized with Precursor 1 and $CuIn_{0.25}Ga_{0.75}Te_2$ with Precursor 2 111

Figure 5.10: TEM micrographs of $CuIn_{0.84}Ga_{0.16}Te_2$ and $CuIn_{0.25}Ga_{0.75}Te_2$ synthesized with Precursor 1 and with Precursor 2 respectively. 112

Figure 5.11: XRD patterns of $CuIn_{1-x}Ga_xTe_2$ synthesized at reaction time 30 min and 60 min. 113

Figure 5.12: UV-Vis absorption spectra of $CuIn_{1-x}Ga_xTe_2$ synthesized at reaction time 30 min and 60 min 115

Figure 5.13: PL emission spectra of $CuIn_{1-x}Ga_xTe_2$ synthesized at reaction time 30 min and 60 min 116

Figure 5.14: TEM and SEM micrographs of $CuIn_{1-x}Ga_xTe_2$ synthesized at reaction time 30 min (a-b) and 60 min (c-d). 118

Figure 5.15: Particle size distribution measured from TEM of $CuIn_{1-x}Ga_xTe_2$ synthesized at reaction time 30 min and 60 min. 119

Figure 5.16: EDS spectra of TEM and SEM micrographs of $CuIn_{1-x}Ga_xTe_2$ synthesized at reaction time 30 min and 60 min 120

Figure 5.17: XRD patterns of $CuIn_{1-x}Ga_xTe_2$ synthesized from precursor concentrations of In: Ga ratios of 0.75:0.25, 0.50:0.50 and 0.25: 0.75. 121

Figure 5.18: XRD patterns showing the expanded view of (111) peak of $CuIn_{1-x}Ga_xTe_2$ synthesized from precursor concentrations of In: Ga ratios of 0.75:0.25, 0.50:0.50 and 0.25: 0.75. 122

Figure 5.19: UV-Vis absorption spectra of $CuIn_{1-x}Ga_xTe_2$ with precursor concentrations of In: Ga ratios of 0.84:0.16, 0.64:0.48 and 0.28: 0.74 from ICP. 125

Figure 5.20: PL spectra of CuIn1-xGa_xTe_2 with precursor concentrations of In: Ga ratios of 0.84:0.16, 0.64:0.48 and 0.28: 0.74 from ICP..... 126

Figure 5.21: TEM and SEM micrographs of $CuIn_{1-x}Ga_xTe_2$ with precursor concentrations of In: Ga ratios of (a-b) 0.84:0.16, (c-d) 0.64:0.48 and (e-f) 0.26: 0.74 from ICP. 128

Figure 5.22: EDS spectra of TEM and particle size distribution of $CuIn_{1-x}Ga_xTe_2$ with various concentrations of In: Ga ratios 129

Figure 5.23: XRD patterns of $CuIn_{1-x}Ga_xTe_2$ synthesized from In: Ga ratios of 0.5:0.5 in HDA and DDT. 131

Figure 5.24: UV-Vis absorption spectra of $CuIn_{1-x}Ga_xTe_2$ with In:Ga actual ratios of 0.57:0.43 in HDA and 0.54:0.48 in DDT..... 133

Figure 5.25: PL emission spectra of $CuIn_{1-x}Ga_xTe_2$ with In:Ga actual ratios of 0.57:0.43 in HDA and 0.54:0.48 in DDT. 134

Figure 5.26: TEM micrographs of $CuIn_{1-x}Ga_xTe_2$ with In:Ga actual ratios of (a-b) 0.57:0.43 in HDA and (c-d) 0.54:0.48 in DDT..... 135

Figure 5.27: Particle size distribution of $CuIn_{1-x}Ga_xTe_2$ with precursor concentrations of In: Ga ratios of .57:0.43 in HDA and 0.54:0.48 in DDT 136

Figure 6.1: Synthesis of ZnO via the sol-gel method..... 148

Figure 6.2: UV-Vis absorption and photoluminescence spectra of ZnO 149

Figure 6.3: Cyclic voltammogram of HDA capped $CuIn_{0.25}Ga_{0.75}Te_2$ synthesized using precursor 2. 150

Figure 6.4: I-V curve showing the important parameters. 152

Figure 6.5: Schematic of the solar cell structure ITO/ZnO/CIT or CIGT/Au and (b) device band structure under illumination. Holes meet the barrier height at the Au electrode, and electrons ca flow in either of two opposite directions to electrodes..... 153

Figure 6.6: I-V curve of the EDT capped $CuInTe_2$ nanosheets. 154

Figure 6.7: SEM images of the OLA capped $CuIn_{0.25}Ga_{0.75}Te_2$ synthesized using precursor 2 and EDT treated $CuIn_{0.25}Ga_{0.75}Te_2$ solar cells..... 156

Figure 6.8: I-V curves of OLA capped $CuIn_{0.25}Ga_{0.75}Te_2$ synthesized using precursor 2 and EDT treated $CuIn_{0.25}Ga_{0.75}Te_2$ solar cells..... 157

Figure 6.9: SEM micrographs of EDT treated $CuIn_{0.25}Ga_{0.75}Te_2$ and annealed films 161

Figure 6.10: I-V curves of EDT treated $CuIn_{0.25}Ga_{0.75}Te_2$ and annealed films at 300, 400 and 500 °C. 162

Figure 6.11: Efficiency trend for the annealed devices..... 163

List of tables

Table 3.1: Frequency of the phonon modes in the Cu–In–Te system observed in the present work and their possible symmetry assignment. 43

Table 4.1: Optical properties of $CuInTe_2$ capped with different surfactants…….. 76

Table 5.1: Cell parameters and grain size of $CuInTe_2$ and $CuIn_{1-x}Ga_xTe_2$ 100

Table 5.2: ICP measurements of $CuIn_{1-x}Ga_xTe_2$ synthesized with various precursors 108

Table 5.3: Lattice parameters and shift in peak position of $CuIn_{1-x}Ga_xTe_2$ synthesized in different precursors. 109

Table 5.4: Composition of $CuIn_{1-x}Ga_xTe_2$ calculated from ICP at different reaction times. 114

Table 5.5 Optical properties of $CuIn_{1-x}Ga_xTe_2$ synthesized at various reaction times…….117

Table 5.6: Lattice parameters and shift in peak position of $CuIn_{1-x}Ga_xTe_2$ with various with various molar ratios of In and Ga 123

Table 5.7: ICP analysis of $CuIn_{1-x}Ga_xTe_2$ with various molar ratios of In and Ga 124

Table 5.8: Optical properties of $CuIn_{1-x}Ga_xTe_2$ with various precursor concentrations of In and Ga 126

Table 5.9: Lattice parameters and shift in peak position of $CuIn_{1-x}Ga_xTe_2$ synthesized in various capping agents..... 132

Table 5.10: ICP measurements of $CuIn_{1-x}Ga_xTe_2$ synthesized in various capping agents 132

Table 5.11: Optical properties of $CuIn_{1-x}Ga_xTe_2$ synthesized in various capping agents 133

Table 6.1: Solar cell parameters of the EDT capped $CuInTe_2$ nanosheets..... 154

Table 6.2: Solar cell parameters of OLA capped $CuIn_{0.25}Ga_{0.75}Te_2$ synthesized using precursor 2 and EDT treated $CuIn_{0.25}Ga_{0.75}Te_2$ 158

Table 6.3: Solar cell parameters of EDT treated $CuIn_{0.25}Ga_{0.75}Te_2$ and annealed films at 300, 400 and 500 °C 161

Abbreviations

ECS: energy conversion and storage

FCC: face-centred cubic

NCs: nanocrystals

CVD: chemical vapour deposition

MOCVD: metal–organic vapour chemical deposition

MBE: molecular beam epitaxy

0D: zero dimensional

1D: one dimensional

2D: two dimensional

3D: three dimensional

TEM: transmission electron microscopy

CZTS: copper zinc tin sulphate

VB: valence band

CB: conduction bands

CIS: copper indium sulfide

$CISe_2$: copper indium selenide

Ga: gallium

CIGS: copper indium gallium selenide or copper indium gallium sulfide

FTO: fluorine-doped tin oxide

QDSSCs: quantum-dot-sensitized solar cells

QDs: quantum dots

PV: photovoltaic

XRD: X-ray diffraction

TOP: trioctylphosphine

OLA: oleylamine

HSAB: hard and soft acid base

HDA: hexadecylamine

EDT: 1,2-ethanedithiol

EDA: ethylenediamine

DEA: diethylamine

VBM: valence band maximum

JZW: Jaffe, Wei and Zunger model.

In: indium

$Ga(acac)_3$: acetylacetonate

Cu $(acac)_2$: copper(II) acetylacetonate

In $(acac)_3$: indium(III) acetate

DDT: 1-dodecanethiol

SEM: scanning electron microscopy

ICP-OES: inductively coupled argon plasma emission spectroscopy

CIT: copper indium telluride

CIGT: copper indium gallium telluride

PL: photoluminescence

EDS: electron dispersive spectroscopy

$LiClO_4$: lithium perchlorate

ITO: tin doped-indium oxide

CV: cyclic voltammetry

LUMO: lowest unoccupied molecular orbital

HOMO: highest occupied molecular orbital

GC: glassy carbon

V_{OC}: open circuit voltage

J_{SC}: short circuit current

FF: fill factor

η: power conversion efficiency

List of Publications

1. N. Ntholeng, B. Mojela, S. Gqoba, M. Airo, S. Govindraju, M. J. Moloto, J. Van Wyk and N. Moloto. Colloidal synthesis of pure $CuInTe_2$ crystallites based on the HSAB theory. New J. Chem., (2016), 40, 10259
2. S. Govindraju, N. Ntholeng, K. Ranganathan, M. J. Moloto, L. M. Sikhwivhilu, and N. Moloto. The Effect of Structural Properties of Cu_2Se/Polyvinylcarbazole Nanocomposites on the Performance of Hybrid Solar Cells. Journal of Nanomaterials, (2016), 8
3. M.A. Airo, R. Rodrigues, S. Gqoba, N. Ntholeng, F. Otieno, M. J. Moloto, M.W.C.C. Greenshields, I. A. Hümmelgen, N. Moloto. Colloidal InSe nanostructures: Effect of morphology on their chemical sensitivity to methanol and formaldehyde fumes. Sensors and Actuators B 236 (2016) 116–125
4. S. Gqoba , M. Airo , N. Ntholeng , L. Machogo , R. Sithole , M.J. Moloto , J. van Wyk , N. Moloto. Evolution of In_2S_3 Nanoplates with Time, Materials Today: Proceedings 2 (2015) 3901 – 3908

Manuscripts to be submitted

1. N. Ntholeng, M. J. Moloto, N. Moloto. Morphology and shape engineering of $CuInTe_2$ nanostructured semiconductor material. “To be submitted”
2. N. Ntholeng, M. J. Moloto, N. Moloto. Heterojunction ZnO/CIT and ZnO/CIGT solar cells. “To be submitted”
3. N. Ntholeng, M. J. Moloto, N. Moloto. Time, precursor, surfactant and stoichiometry dependency of quaternary $CuIn_{1-x}Ga_xTe_2$ nanostructured semiconductor materials. “To be submitted”

Oral Presentations

Materials for Advanced Materialization (MAM) conference (2014)

Nano Africa conference (2013)

National Research Fund (NRF) Wits presentations (2013)

Research Visit

The University of Manchester, School of Chemistry, POB research group (July –Sep 2014)

Chapter 1: Synopsis

The aim of the study was to synthesize and characterize ternary and quaternary copper-tellurium based nanocrystals for the application in solution processed photovoltaics. As such, the thesis is therefore presented in the following format:

Chapter 1: is the motivation and rationale for the study as well as aims and objectives.

Chapter 2: interrogates the literature on semiconductor nanostructures, particularly on the ternary and quaternary metal chalcogenides. It further demonstrates the synthesis principles and challenges associated with their application in solar cells.

Chapter 3: offers information on the colloidal synthesis of ternary $CuInTe_2$ nanocrystals. The data presented demonstrates the crystallization mechanism of particles according to HSAB principle.

Chapter 4: entails shape and morphology engineering of $CuInTe_2$ nanocrystals through the use of various capping agents and variation in reaction time. The mechanism for the transition of the morphology from 1D to 2D particles is also discussed.

Chapter 5: the colloidal synthesis and characterization of quaternary $CuIn_{1-x}Ga_xTe_2$ is discussed. Different metal precursors were used to prepare the nanocrystals and the effect of the reaction time on the optical band gap is discussed. Band gap engineering is explored through stoichiometry variation of indium and gallium concentrations.

Chapter 6: the photovoltaic properties of ternary $CuInTe_2$ and quaternary $CuIn_{1-x}Ga_xTe_2$ are discussed. Surface modification and thermal treatments of the quaternary based photovoltaic devices are also discussed.

Chapter 7: gives a summary of the general conclusions from all the work carried out and presented in this thesis.

1.1 Motivation and rationale

The migration to renewable energies due to the depletion of fossil fuels has seen the tremendous industrial development of solar cells. This is due to the solar energy being a resource of choice for renewable energy since it is freely and abundantly available in all countries and regions [1]. The direct conversion of solar energy to electricity is via the photovoltaic effect, in which the absorbed light, excite the electrons creating electron–hole pairs. This result in separation of charge carriers which are collected at opposite electrodes [1]. However, the daunting challenge has been replacing the silicon-based solar cells with high-performance materials which are inexpensive.

As such, development of second generation solar cells came to light, in which the absorber layer constitute of inorganic semiconductor thin films chalcopyrites such as cadmium telluride (CdTe), copper indium gallium selenides (CIGS), kesterites such as copper zinc tin sulfide (CZTS) and amorphous silicon (a-Si) [2]. The inorganic thin film semiconductors proved to be efficient in that a large portion of the sunlight could be absorbed by few nanometers up to few micrometers of the light absorber [1]. Furthermore, the ability to combine the $Cu(In,Ga)(S,Se)_2$ material family internally as well as with other materials to form multi-junctions, leaves the pathway to further increase efficiency, especially for

concentrator concept [1]. Nevertheless, the excitement of the second generation solar cells was short-lived as it was later realized that the fabrication process requires vacuum-based technologies retaining high production costs. In addition, their efficiencies did not match up to that of silicon [1].

The reduced production costs emerged with the third generation solar cells in which solution-processed methods such as electrochemical deposition, spray pyrolysis and more were utilized [3]. These comprise of organic (polymeric), dye-sensitized, perovskite, nanocrystal based solar cells including quantum dot solar cells [4-6]. Amongst the existing inorganic semiconductor materials, the Cu-based ternaries and quaternary have attracted a lot of attention owing to their promising properties such as direct band gap, quantum confinement effects which permit fine tuning of the electrical and optical properties. Much of the work has been reported on the selenides and sulfides [7]. For example, solar energy conversion efficiency of about 20% and 12% have already been reported for $CuInSe_2$ and $CuInS_2$ respectively [8]. However, not much attention has been paid to the tellurides although their properties such as its direct band gap of 1.02 eV, lower degree of ionicity of metal–chalcogenide bonds and larger Bohr radii of excitons which qualify them as potential absorbing material [9].

Amongst the emerging technologies, liquid based synthesis approach has proved to be an efficient way of accomplishing well-defined semiconductor nanocrystals [10]. By dispersing in suitable solvents with aid of capping agents while monitoring parameters such as reaction temperature, reaction time etc., properties of the semiconducting nanostructured materials can be modified and this can result in improved device performance.

1.2 Aims and objectives of the study

The aim of the study was to synthesize and characterize ternary and quaternary copper-tellurium based nanocrystals for the application in solution processed photovoltaics. Hence the following objectives were undertaken:

- Synthesis and characterization of $CuInTe_2$ using the colloidal method
- Optimization of the synthesis of $CuInTe_2$ by varying reaction parameters
- Synthesis and characterization of $CuIn_{1-x}GaxTe_2$ using the colloidal method
- Optimization of the synthesis of $CuIn_{1-x}GaxTe$ by varying reaction parameters
- Application of $CuInTe_2$ and $CuIn_{1-x}Ga_xTe_2$ nanostructures in inverted inorganic heterojunction solar cells
- Compare the solar cell performance of $CuInTe_2$ and $CuIn_{1-x}Ga_xTe_2$
- Study the effect of ligand exchange on the performance of $CuIn_{1-x}Ga_xTe_2$ based solar cells
- Study the annealing effect on the performance of $CuIn_{1-x}Ga_xTe_2$ based solar cells

1.3 References

1. M. Eslamian, *Nano-Micro Letters*, 2017, **9**, 3.
2. N. Ali, A. Hussain, R. Ahmed, M. Wang, C. Zhao, B. U. Haq and Y. Q. Fu, *Renewable, and Sustainable Energy Reviews*, 2016, **59**, 726-737.
3. M. Eslamian, *Coatings*, 2014, **4**, 60-84.
4. Q. Wang, Y. Xie, F. Soltani-Kordshuli and M. Eslamian, *Renewable and Sustainable Energy Reviews*, 2016, **56**, 347-361.
5. M. Ye, X. Wen, M. Wang, J. Iocozzia, N. Zhang, C. Lin and Z. Lin, *Materials Today*, 2015, **18**, 155-162.

6. M. Habibi, F. Zabihi, M. R. Ahmadian-Yazdi and M. Eslamian, *Renewable and Sustainable Energy Reviews*, 2016, **62**, 1012-1031.

7. S. Siebentritt, in *Wide-Gap Chalcopyrites*, Springer, 2006, pp. 113-156.

8. M. A. Green and K. Emery, *Progress in Photovoltaics: Research and Applications*, 1993, **1**, 25-29.

9. N. Ntholeng, B. Mojela, S. Gqoba, M. Airo, S. Govindraju, M. Moloto, J. Van Wyk and N. Moloto, *New Journal of Chemistry*, 2016, **40**, 10259-10266.

10. J. Chang and E. R. Waclawik, *RSC Advances*, 2014, **4**, 23505-23527.

Chapter 2: Literature review

2.1 Introduction

The use of nanostructured materials in solar cells has rapidly increased over the years [1]. This was not only motivated by the ecological problems experienced with the non-renewable fossil fuel but also the ongoing global economy crisis [2]. As such migration to cost-effective, efficient, and environmentally benign energy conversion and storage (ECS) devices is of great importance [3]. Therefore, the use of these materials as absorbing layers in photovoltaic devices has come as a contingency plan to overcome costs incurred during manufacturing of these devices [4]. They also ensure energy devices with high performance relatively close to that of Silicon and polycrystalline solar cells [1].The motivation for utilizing nanostructured materials arises from their specific physical and chemical properties [1]. The nanostructured materials can be used to improve a regular crystalline structure thus result in increased absorbance in spectra of thin film [1]. Secondly, light-generated electrons and holes travel much shorter path thus reducing recombination losses [1]. Thirdly, different layers with various band gaps can be made by changing the size of nanoparticles. This gives room to more design flexibility in the absorber layer of the solar cell. The absorber layer thickness of the nanostructured solar can be as thin as 150 nm which is thinner than 2 mm of the traditional thin film solar cells [1].

Among the various types of materials, the semiconductor nanostructured materials particularly metal Cu chalcogenides (sulfides, selenides, and telluride) have received remarkable attention due to their intriguing chemical, optical, thermal, electrical, mechanical properties and the combination of decent conversion efficiency [5]. Predominantly, semiconductors metal Cu chalcogenides nanostructured are promising due to their narrow

emission [5]. They have low toxicity and are environmentally compatible. They offer a wide range of compositions and crystal structure which can be manufactured at low costs [6]. There are various types of Cu chalcogenides based semiconductors namely: binary, ternary and quaternary copper chalcogenides [6].

2.2 Copper chalcogenide semiconductor materials

Initially, binary CuS/CdS solar cell was developed as an alternative to single crystalline silicon and polycrystalline silicon solar cells to provide low manufacturing costs [7]. Due to severe stability problems they were discontinued in the 1980s [7]. This led to the development of polycrystalline thin films materials. At the time CdTe/CdS was proposed as a better alternative, but it was later found that Cd is toxic and that raised environmental concerns [7]. As such combination of metal chalcogenides particularly of group III and IV was established [7]. Since then a lot of work has been done investigating the properties of these materials [6]. The binary copper combination is $Cu_{2-x}A$; where A = S, Se, and Te [6]. These materials have therefore been implemented into several applications such as solution-processable photovoltaic and nano-plasmonic devices, photocatalysis, photo-thermal therapy and biomedical sensor [6-8,8b]. Among the existing binary copper chalcogenides, Cu_2S is the most studied material [6]. It has a lot of different equilibrium crystal structures characterized by hexagonal or cubic structure. In cubic structure, the S atoms are closely packed with Cu atoms at the interstices. The transformation from cubic to hexagonal goes through metastable phases though it can be very slow. The binary selenides and tellurides also have various crystal structures [6].

The ternary copper chalcogenides are derived from the binary counterparts. They generally have a formula of $CuXA_2$ where (X= In, Sn, Ga, Al; A = S, Se, Te) [6]. At room temperature,

they exist in the chalcopyrite structure though they have another stable phase called the spinel crystal structure (see Fig. 1) [6]. Both these crystal structures have a face-centered cubic (fcc) close packing of the anions [6]. The chalcopyrite lattice is formed by substituting the zinc in the cation sublattice by both high and low valence cations in an ordered manner [8b]. For example, the high valence cation will be In^{3+} and low valence will Cu^{1+}. The phase transformation can occur at high temperatures for both bulk and nanoscale materials [6]. For example, the bulk $CuInS_2$ and $CuInSe_2$ show the chalcopyrite crystal structure at room temperature and the wurtzite structure are only stable at high temperatures [8b]. However, the opposite is observed for nanocrystals (NCs) as they can exhibit both crystal structures at room temperature. To establish nanocrystals in the chalcopyrite structure, the reactivity of both cation precursors must be balanced. This entails the use of appropriate coordinating ligands and reaction temperature [8b].

For quaternary materials, the difference in cation positions and anion distribution within the lattice results in various crystal structures. They adopt kesterite, stannite, and wurtzite structures (see Fig. 2.1) [8b, 9-10]. The tetragonal kesterite structure is made of alternating cation layers while the stannite made of a different composition of cation layers [8b]. However, different synthetic methods will give different crystal structures. Therefore, in order to obtain a specific crystal structure, one has to follow a particular synthesis method. As such this has led to the development of different synthetic methods over the years.

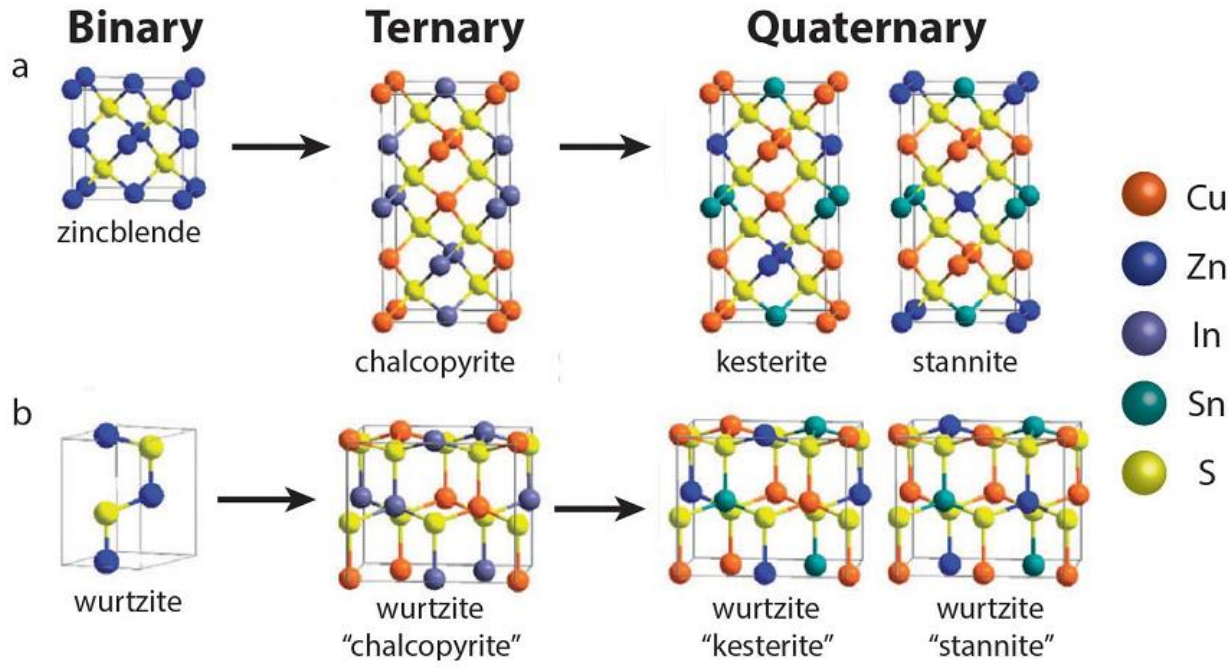


Figure 2.1: Crystal structures of ternary and quaternary Cu chalcogenide NCs. a) If the binary NCs have a zinc-blende-like crystal structure, the resulting ternary NCs have the chalcopyrite crystal structure, whereas the quaternary NCs will have either stannite or kesterite structures. b) If cation-exchange reactions are deployed on wurtzite-like Cu chalcogenides, the resulting ternary and quaternary NCs also have a wurtzite structure [[11]].

2.3 Synthesis of Copper chalcogenide semiconductor materials

In a quest to develop high-quality copper chalcogenides materials with finely tuned properties a lot of chemical synthetic methods have been developed [[12]]. Techniques such as hydro/solvothermal [[8b]], polyol synthesis [[8b]], non-hydrolytic sol-gel process [[8b]], aqueous methods [[8b]], solid phase synthesis [[8b]], chemical vapour deposition (CVD) [[13]], metal–organic vapour chemical deposition (MOCVD) [[14]], molecular beam epitaxy (MBE) [[15]], magnetron sputtering [[14]], laser ablation [[16]] and etc. have previously been applied for syntheses of semiconductor nanocrystals [[12]]. The vapour and solid-phase methods are

reported to be unsuitable for producing high-quality nanocrystals [17]. This is attributed to a limitation in instrumentation and precursors used in these methods [17]. On the other hand, liquid-phase approaches particularly colloidal method have proven to be efficient for establishing well-defined semiconductor nanocrystals [17]. This method was initially discovered by Faraday over 150 years ago [18]. It further evolved from the pioneering work of Henglein and Brus whom discovered CdS colloids [19-20]. The discovery of Murray and co-workers further advanced this method by producing quantum dots by hot-injection synthesis [21]. Since then this method has been utilized to synthesize multitudes of nanocrystals with different sizes, compositions, and shapes [22]. The suitable solvents and capping agents often dispersed in the solution based synthesis allows fine tuning of energy structures, high optical absorption coefficients, large dipole moments and potential multiple generation properties [17].

2.3.1Colloidal synthesis: nucleation and growth of nanocrystals

2.3.1.1 Nucleation process

The formation mechanism of nanocrystals in colloidal synthesis is governed by nucleation and growth processes [22]. It has been shown that nucleation is a crucial parameter for determining the size distribution of the particles [23]. Therefore, it is essential that it takes place very quickly. This may be easily achieved in hot injection methods where nucleation occurs immediately after injection of the precursor into the solvent [24]. The nucleation process can either be homogeneous or heterogeneous [23]. In homogeneous nucleation (see Fig. 2.2), metal ions are reduced in order to create a critical composition of atomic species [23]. Nucleation begins when the concentration of the atomic species is above a critical level [23]. The process will occur by rapid consumption of the reactants [23]. Subsequent to that

growth process will occur on the pre-existing nuclei [23]. Further nucleation is ceased by a drop in the concentration reactants to below the critical limit [22].

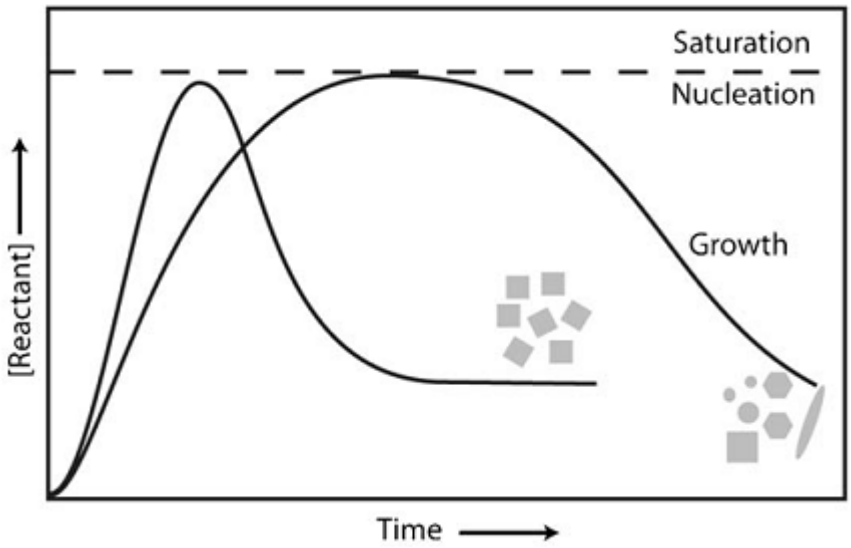


Figure 2.2: The La Mer model of nucleation, where a critical reactant concentration is required for particle nucleation. Homogenous nanoparticle dispersions are favored by a single, rapid nucleation event [25].

On the other hand, if nucleation is allowed over extended periods, a variation in growth rate result [23]. This is due to the reactants being unevenly consumed in the solution. To avoid extended nucleation, fast nucleation can be attained by slow building up of the concentration of metal ions in solution [23]. A sequential injection of metal precursors in the system until nucleation occurs will help achieved this [23]. It is also necessary to avoid fast reduction of metal ions, as it will lead to the limited formation of reactants species failing to reach the critical nucleation concentration [23]. A change in the reactivity of metal precursor will result in the formation of metal complexes which are able to deter the reduction reaction [23]. For example, the solubility of the ionic precursor in the colloidal synthesis of single-crystalline Ag nanocubes was modified by adding Cl^- ions, resulting in a formation of less soluble AgCl which then prevented the reduction of the metal ions [23]. Furthermore, the presence of

competing reduction and oxidation processes is detrimental in that it results in reversible particle nucleation which is mostly observed by a colour change in reaction solution [23]. Moreover, the formation of single crystalline particles is key in homogenous nucleation [23]. This is especially important for controlling shape and growth of the nanocrystals.

For heterogeneous nucleation, the seed particles are formed initially in separate synthetic step [23]. The reaction proceeds by adding preformed seed particles to a reactant mixture, thereby isolating nanocrystal nucleation and growth of the nanocrystals [23]. Growing seed separately significantly lowers the activation energy for the metal reduction which is not the case in homogeneous nucleation [26]. Therefore the barrier to homogeneous nucleation is always much higher than that of heterogeneous nucleation as it requires the formation of a new phase [22]. However, the magnitudes of these barriers are influenced by factors such as binding constants of the employed precursor, the level of supersaturation, the solution temperature; and the concentration of additional ligands (surfactants) in solution, which directly influences both the supersaturation and the surface energy [22]. Though these aforementioned factors play a crucial role, the reaction conditions for shape control are not strict in comparison to homogeneous nucleation [22]. The shape control is such that the reduction of metal ions is facilitated by adding seed particles to growth medium [23]. This, therefore, requires the use of milder reducing agents, lower temperatures, or aqueous solutions to evaluate size [23]. Murphy et al. reported that the nucleation and growth of the particles were isolated by the addition of preformed seeds to a metal precursor in the presence of a weak reducing agent [26]. This has also been reported to aid shape and size control of the nanocrystals [23]. The presence of the reducing agent induces autocatalytic growth on pre-existing nuclei which allows control over the morphology of the particles during the growth stage [23].

2.3.1.2 Growth process

A decline in the nucleation rate will result in the proceeding of the growth stage [22]. The growth of nanocrystals takes place via the diffusion of monomers to the particle surface, followed by incorporation of monomers into the crystal bulk [22]. This may proceed by either the consumption of molecular precursor in the surrounding solution thus forming narrow size distribution or by Ostwald ripening forming wide size distribution [24]. The narrow size distribution is known as the focusing of size distribution while the Ostwald ripening is called the defocusing of the size distribution [27]. Focusing or defocusing of the size distribution is determined by the concentration of monomers available in the system [27]. Monomer concentration in the reaction system determines the critical size with high monomer concentration favoring small critical size and vice versa [27]. However, to fully understand this, a relationship between the growth rate and the radius of nanocrystals needs to be established. The dependence of the growth rate on the radius of the nanocrystals is depicted in Fig. 2.3. From Fig. 2.3, the negative growth rate in the red curve is caused by small unstable crystals [27]. The instability in the crystals is due to a large fraction of surface atoms [27]. As the growth rate further increases the crystals becomes more stable reaching the critical size point [27]. At this point, the crystals neither grow nor shrink [27]. As for the blue curve (Fig. 2.3), the rising growth rate is due to the incorporation of many atoms which result in increased radius of the crystals [27]. Therefore, consumption of monomers as growth takes place will result in the critical size falling in an average size distribution of nanocrystals (Fig. 3 blue curve) [27]. The broad size distribution resulting from Ostwald ripening arises due to small nanocrystals with high chemical potential evolving to monomers and re-dissolving whereas large nanocrystals consume monomers and grow [27]. However, it is possible to reverse this process and recover monodispersity using several techniques [27]. The commonly known and most used technique is called size selective precipitation [21,28].

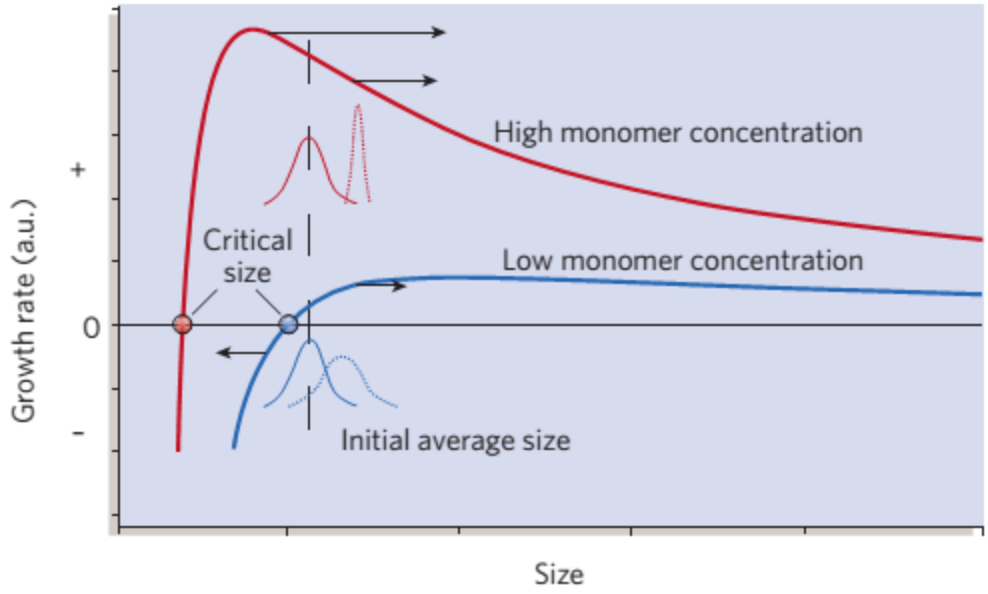


Figure 2.3: Growth rate dependency on the nanoparticle size for low and high monomer concentration [27].

This method entails the stepwise addition of the solvent to gradually reduce the solvating power and allow for aggregation [27]. This results in the precipitation of larger nanocrystals with greater attractive van der Waals or dipolar forces between them first and so on. This can yield nanocrystal fractions with narrow size distributions [27]. The disadvantage of this method is that it only works well with round nanocrystals because the attractive forces between anisotropic nanocrystals are difficult to overcome and they depend on multiple parameters [29]. In a separate study, Howard Reiss proposed that if monomer concentrations are sufficiently high, small nanocrystals will rapidly grow than the larger ones [30]. For example, abruptly increasing monomer concentration by injection under slow growth conditions will not affect the distribution of the nanocrystal sizes but will shift the critical size to a smaller value [30]. If the shift in critical energy is high enough, all the nanocrystals will be larger than the size for which the growth rate peaks [30]. Following that, the size distribution will spontaneously narrow or focus [30]. This concept was later proved

experimentally [31]. The experimental work carried out showed that for optimal size focusing, monomer concentration must be in such a way that the average nanocrystal size is continuously slightly larger than the critical size [31]. The other added advantage of focusing is that large quantities of crystal with a narrow size distribution are produced [27]. In addition to kinetic control over nanocrystal synthesis, it was found that it also enables kinetic shape control [27].

2.3.2 Shape and morphology of nanocrystals

Previously it was reported that shape evolution mechanism of crystals is given by the Gibbs Curie–Wulff theorem [32]. According to the theorem, the surface energy is crucial for predicting the morphology of crystals. Surface energy is defined as excess free energy per unit for a specific crystallographic face [33]. Though this theorem could successfully account for morphological control in most systems, it failed to explain shape evolution in a single system [33]. It was therefore concluded that this theorem is based on thermodynamically grown crystals thus it cannot account for kinetically trapped morphologies [33]. The selective adsorption model was then adopted for shape control in anisotropic crystal growth [34]. Herein, surface free energy of individual crystallographic faces is controlled by selective adsorption of surfactant at different crystallographic faces of the growing crystals [33]. In other words, the faced covered by the capping agent will take a slower growth rate and thus a greater proportion on the surface [35]. Fig. 2.4 illustrates capping agents directing the growth of a single-crystal seed of an fcc metal. For example introducing a capping agent for the {100} facets will result in a change in the order of surface free energies thereby favouring faster growth along the ⟨111⟩ directions than along the ⟨100⟩ directions [35]. The difference in growth rate will enable a gradual increase in the ratio between the areas of {100} and {111} facets on the surface [35]. The shape of the nanocrystal will develop from truncated

octahedron to cuboctahedron, truncated cube, and ultimately a cube enclosed by {100} facets only [35]. In the case of a capping agent for the {111} facet, the specific surface free energy of the {111} facet will be further decrease favouring faster growth rate along the ⟨100⟩ direction [35]. This will continually reduce the proportion of the {100} facet during growth, ultimately leading to the formation of an octahedron enclosed by {111} facet only [35].

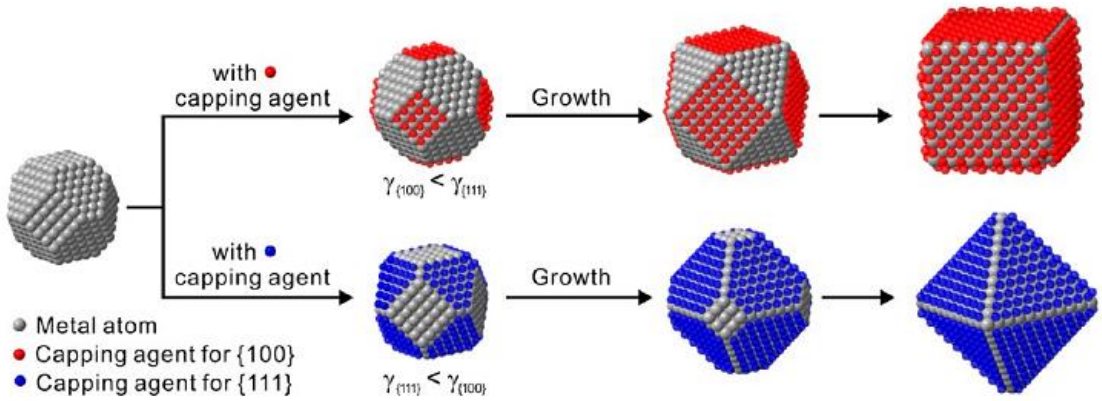


Figure 2.4: Schematic illustrations showing the role of capping agents in directing the growth of a single-crystal seed made of an fcc metal. Introduction of a capping agent (represented by red or blue dots) that can selectively bind to a specific type of facet, altering the order of surface free energies and eventually leading to the formation of a nanocube enclosed by {100} facets and an octahedron enclosed by {111} facets, respectively [35].

The use of various capping agents with different preferential binding will allow the formation of nanocrystals with a myriad of shapes [35]. The preferential binding of a capping agent to a specific surface is influenced by factors such as crystal structure and the functional group(s) of a capping agent, including the electronic and surface structure of the metal [35]. It was further proposed that shape evolution of nanocrystal can be manipulated by sequential injection of effective monomer precursors [31,36-37]. This was proposed especially for the formation of elongated shapes [33]. In this case, morphology evolution is dependent on the

high concentration of monomers which is highly required for anisotropic growth of nanoparticles [33]. Anisometry in morphology is based on the growth confinement or growth in a particular direction of the nanoparticles [38]. Over the years a lot of anisometric nanomaterials classified by growth dimensions such as 0D, 1D, 2D, 3D have been reported. Fig. 2.5 depicts examples of different dimensional nanocrystals. Typically growth of these anisometric particles was as a result of many factors influencing the kinetics of the particle growth.

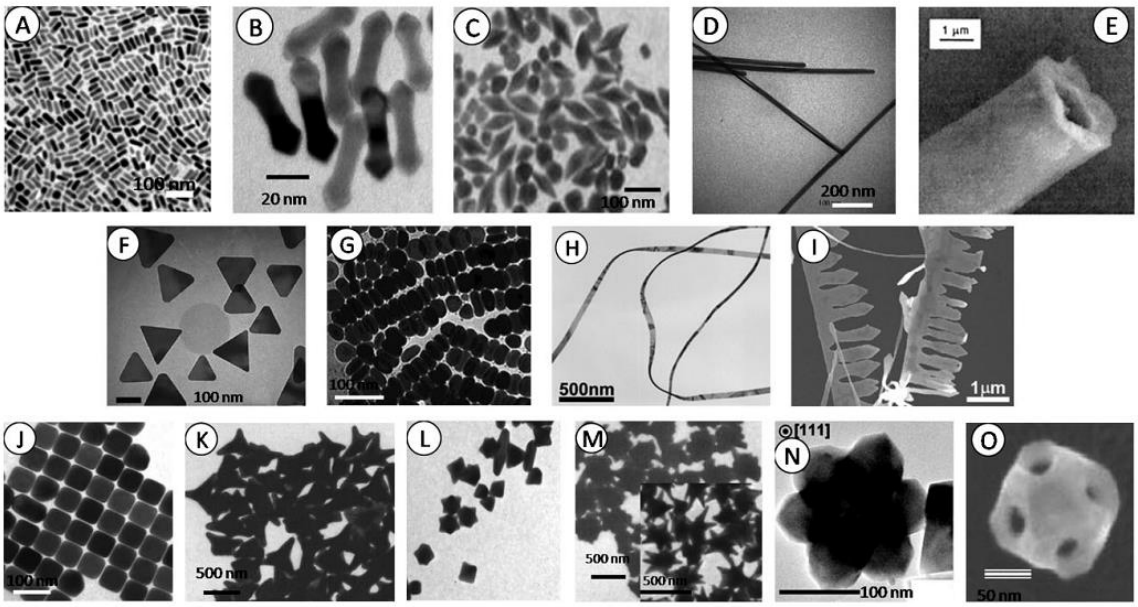


Figure 2.5: 1D: A) nanorods [39], B) nanoshuttles [40], and C)nano bipyramids [41] D) nanowires [42] E) nanotubule [43] 2D nanoparticles: F) triangular nanoplate [44], G) nanodisk [45], and H) ribbons [46]; I) belts [46]. 3D nanoparticles: J) nanocubes [47], K) tetrapods [47], L–M) star-shaped [47] N) nanohexapods [48], and O) nanocage [49].

Reports have shown that the formation of 1D structure requires the formation of defects such as twin defect, stacking faults and etc. [50]. Formation of defects is crucial for breaking the symmetry of the cubic lattice. It is also important to create kinetic conditions favoring a higher growth rate along one axis with respect to those perpendicular [50]. This is mostly

important for the formation of nanorods [38]. Previously, TEM studies showed the formation of fivefold symmetric rods [38]. Formation of these structures was explained as an elongation of penta-twinned decahedral seeds parallel to the twin planes [38]. However, there was a lack of evidence to show that the formation of these structures was due to the presence of reentrant grooves in penta-twinned decahedral seeds parallel to the twin planes [38]. It was speculated that the twinning event on an undeveloped decahedron could regenerate reentrant grooves leading to elongation and rod-shape formation [51]. Additionally, it was indicated that the facet-specific adsorption of additives and relative facet growths of the seed are key for the formation of a rod or wire shapes [52-54].

For 2D structures, a lot of mechanistic explanations were proposed. Zeng et al. attributed the formation of shapes such as nanodisks, triangular nanoplates, and nanospheres to surfactant-crystal-plane interaction energies [55-56]. Other reports suggested that the formation mechanism of nanoplates or nanoprisms could not only be explained by the face-selective binding model, but the internal defect structures also need to be considered [38]. Other authors argued for the seed-structure based mechanism, specifically for the formation of 1D and 2D particles [51]. Their argument was based on the model proposed by Hamilton and Seidensticker which explained the formation of planar germanium crystals and twinned silver halide crystals [57]. They argued that the twin plane in fcc crystals creates reentrant grooves which are favorable sites for the for the attachment of adatoms [38]. The formed reentrant groove will cause rapid crystal growth [38]. This is due to the strong bond between the isolated adatom at a surface site on an (111) plane and adatom at the reentrant groove resulting in higher growth rate [58]. Therefore, a single twin plane in the seed leads to the formation of triangular prisms, whereas the presence of two parallel twin planes forms hexagonal nanoplates [38]. For example, wurtzite Cu_2ZnSnS_4 nanocrystals with prism and

plate shapes were selectively obtained by using different capping ligands [59]. A mixture of DDT and OLA was used as the solvent and ligands for obtaining prism CZTS nanocrystals while oleic acid resulted in the formation of nanoplates [59]. On the other hand, it was found that combining two thiols is critical for the formation and assembly of nanorods [60]. In other studies, the formation of nanobelts goes through a transformation from the sphere, triangle, to belt shapes via Ostwald ripening process [61-63]. Evidently, there are a lot of proposed mechanisms for different 2D nanocrystals.

The growth of three-dimensional shapes such as cubes, octahedra, is dependent on the relative facet growth rates [64]. Evolution of these shapes is based on the surface control conditions as seen in Fig. 4. Subsequently, polyhedral growth shapes are also obtained by fine-tuning the relative growth rates of the different facets [65]. Change in surface energy of the facet is mainly influenced by the composition, coverage, and binding energies of adsorbed species [65]. Therefore by changing reagent concentration and reaction temperature, the growth rate will be affected [64-65]. The obsession over morphology control in nanocrystals is due to its ability to determine the electronic and optical properties of the materials based on quantum confinement.

2.4 Optical properties

The quantum effect resulting from size and shape control occurs when the dimension of a nanocrystal is smaller than the Bohr exciton radius of the material [66-67], thereby resulting in a change of the electronic structure from a continuous band of bulk counterparts to discreet or quantized levels. The characteristics of the discrete bands of semiconductors are similar to those of molecules (Fig. 2.6) [17].

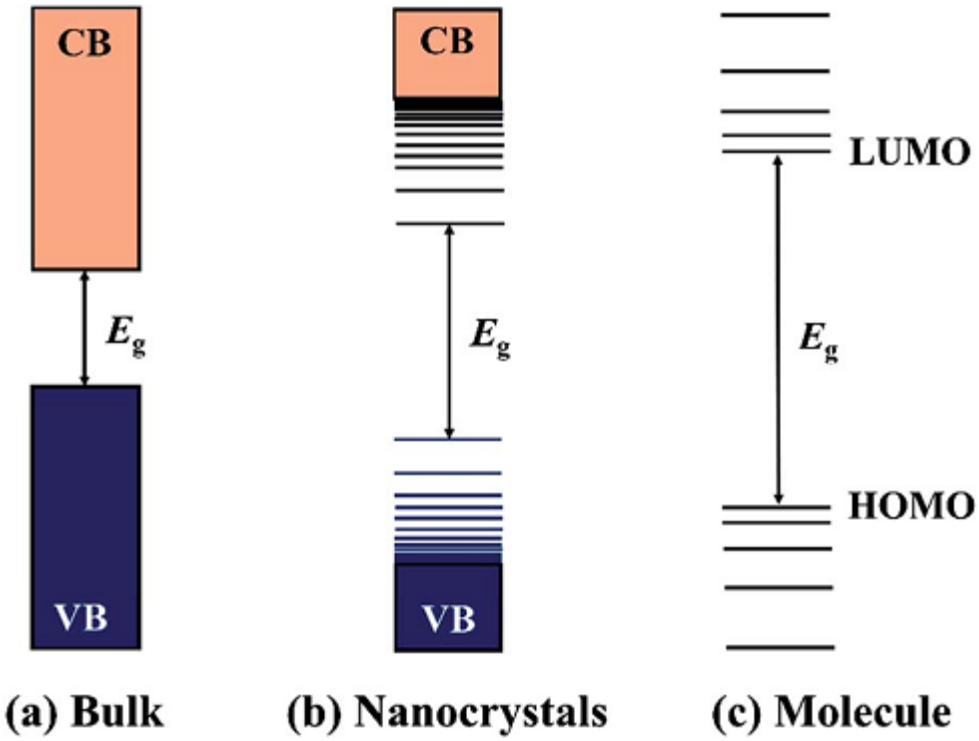


Figure 2.6: A comparison of the electronic energy states of different types of semiconductor materials: (a) bulk semiconductors, (b) semiconductor nanocrystals, and (c) molecular semiconductors [17].

As a result, this allows photon absorption of a particular wavelength with energy greater than band gap E_g [68]. The absorption of photon energy will excite the electron leaving behind an orbital hole in the valence band (VB). Thereafter, the electron will undergo a radiative recombination thus emitting a photon [68]. It must be noted that there is the difference between the nature of the valence and conduction bands (CB) in binary and ternary copper chalcogenides systems [6]. For binary nanocrystals, they are composed of p and s orbitals from anion-like group VI element and cation-like of the group II element respectively [69]. In ternary systems, the upper VB in ternary copper chalcogenides is comprised of Cu 3d orbitals hybridized with the p orbitals of the group VI element, whereas the CB is made of Cu 4s orbitals with some mixing of p character from the chalcogen atoms [69]. Similarly, this

applies to quaternary systems as well. The difference is attributed to ternary systems being more defect tolerant than in binary systems [6]. Therefore, making their optical band gap properties composition-dependent with high copper content resulting in a decrease in band gap [6]. Furthermore, there is a difference observed in the absorption spectra of binary and ternary copper chalcogenides. There is a sharp absorption transition observed in binary nanocrystals and low energy tail seen for ternary [8a]. The observed low energy tail in ternary systems could be attributed to size and shape inhomogeneity [8a]. It was indicated that composition inhomogeneity in these systems can exist even if particles are monodisperse in size and shape [8a].

Moreover, the photoluminescence (PL) of these systems is different from that of the binary systems in that it is characterized by a broad band (full width at half maximum 200–300 meV), a large "global" Stokes Shift (300 meV), and multi-exponential PL decays with long decay constants [8a]. However, there are controversies about the origin of these intriguing optical properties. Initially, the donor-acceptor recombination model similar to bulk ternary copper chalcogenides was proposed (Fig. 2.7a) [8a,70]. This model proposes that the donor-acceptor recombination entails native point defects such as Cu_{In}, V_{In}, or V_{Cu} [70]. It also assumes that the defect structure is similar in both bulk and nanoscale level [8a]. However, the model fell short in explaining the absorption transition due to a size decrease [71-72]. Following this, it was proposed that radiative recombination of quantized VB hole states with electrons localized at native point defects occur (Fig. 2.7c) [73-74]. Others suggested that recombination occurs between quantized CB electron states with localized holes (Fig. 2.7b).[72-75]. The difference between these two studies is that Fig. 2.7c suggests that the hole is localized at native core defects [73-74] whereas in Fig. 2.7b it is assumed that hole localization results from a strong hole–phonon coupling and large nuclear reorganization

energies upon localization, which induces hole self-trapping at a regular Cu+ ion [75]. This model further suggests that hole–phonon coupling is stronger in nanoscale than in bulk and there are no point defects at nanoscale level thus no radiation recombination centres [75].

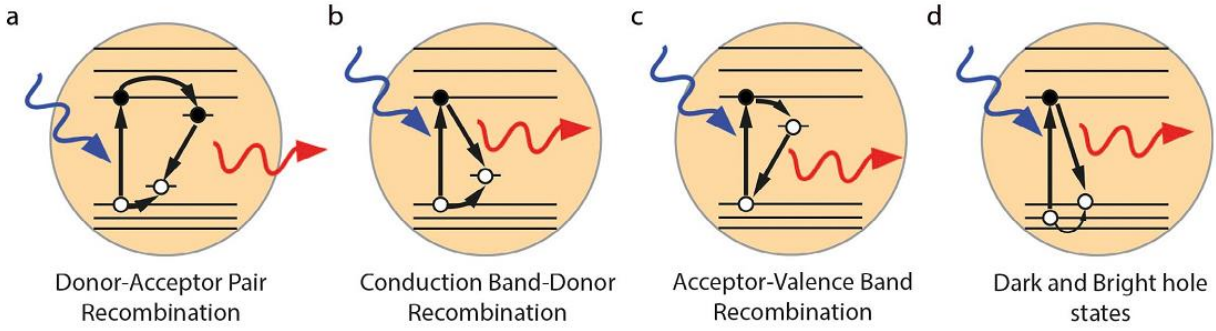


Figure 2.7: Possible recombination pathways in$CuInS_2$ nanocrystals. The origins of the intriguing optical properties of $CuInS_2$ NCs are not yet understood and are still under debate. a) PL of CIS NCs is due to a donor–acceptor pair recombination due to point defects such as Cu_{In} ,V_{in} ,or V_{Cu} .b) PL due to recombination of quantized CB electron states with localized holes. c) PL of CIS NCs is due to radiative recombination of quantized VB hole states with electrons localized at native point defects. d) PL of CIS NCs is intrinsic and originates from the 1S(e)-1S(h) exciton transition [8a].

Recently Efros and co-workers proposed another model shown in Fig. 6d [76]. Herein, they propose that PL of $CuInS_2$ (CIS) NCs is intrinsic and originates from the 1S(e)-S(h) exciton transition [76]. In this case, the recombination involves the recombination of quantized CB electron states with quantized VB hole states, which thus precludes the involvement of localized carriers [76]. It further explained that the observed Stokes shift and long lifetimes in PL result from the nature of the 1S(h) fine-structure states [76]. The fine structure states described as high emitting separated by size-dependent energy gap from the low emitting state [76]. The low-energy tail in the absorption spectra was said to originate from the emitting

state itself [76]. Understanding the size-dependent optical properties of colloidal nanocrystals is crucial for their deployment in applications [8a].

2.5. Photovoltaic applications

Energy conversion in photovoltaics occurs when an incident photon imparts energy to an electron in an absorbing layer thus promoting an electron to an excited state [77]. The excited electron from the valence band to the conduction band will leave behind a positively-charged vacant state (hole) [77]. There is an interface between the electron-conducting (n-type) and hole-conducting (p-type) materials which prevents recombination of electrons and holes inhibiting loss of energy [77]. These barriers can be p-n homojunction, p-n heterojunction, and p-i-n depending on the desired device functions [77]. Direct band gap thin film photovoltaic materials typically form p-n heterojunction configuration shown in Fig. 2.8 [77]. This is due to the carrier collection supported in this configuration, where electron mobility is generally higher than the hole mobility [77]. Moreover, highly conductive wide-gap p-type window materials are very difficult to fabricate [77].

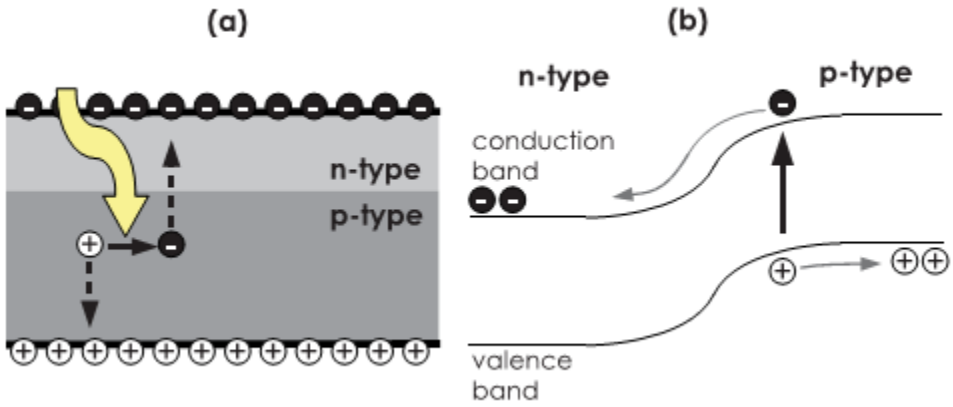


Figure 2.8: (a) Schematic cross-section of a traditional inorganic solar cell. A light-absorbing p-n junction is located between charge-collecting electrodes. (b) Band diagram of the solar cell. An electron is excited from the valence band to the conduction band by incident light, then electrons and holes are separated by the p-n junction. Charges are transported to collection electrodes as majority holes and minority electrons in the p-type layer and majority electrons and minority holes in the n-type layer [[77]].

Large absorption coefficients and high stability of copper chalcogenides system have made them desirable for applications in thin film solar cells as photo-absorbers [[78-79]]. This has mainly been because of the ability of fine tuning of the band gap through colloidal synthesis. The reported bulk band gaps are 1.55 eV, 1.01 eV and 0.97 eV for $CuInS_2$, $CuInSe_2$ and $CuInTe_2$ respectively [[80]]. Alloying these ternary systems with gallium (Ga) saw an increase in band gaps depending on the Ga content [[81]]. The highest efficiency of 20% has been reported for CIGS thin film solar cells [[6]]. Other studies reported 12.6% efficiency for CZT(S, Se) which is lower than CdTe with 16.7% but higher than amorphous silicon with 10% efficiency [[82-83]]. Though copper chalcogenides based semiconducting materials could

potentially help in attaining high efficiencies in photovoltaic devices, the stumbling block has been the fabrication techniques used for manufacturing these devices [6]. The expensive fabrication techniques currently employed hinders the widespread deployment [6]. Therefore low costs fabrication methods are required. The deposition of an absorber layer using nanocrystals ink and high throughput methods such as solution coating or printing has been reported [83]. Unfortunately, ink printed devices showed less efficiency than that of conventional techniques [83]. The limited performance in CI(S, Se) and CIGS devices was attributed to poor charge transport [84]. Recently it was shown that ligand exchange and composition tailoring through cation exchange can enhance carrier mobility and polarity charge in these devices [84]. For example substituting DDT ligand with a short ligand such as 1,2-ethanedithiol and cation exchange between ambipolar Cd^{2+} and n-type mobility In^{3+} [84].

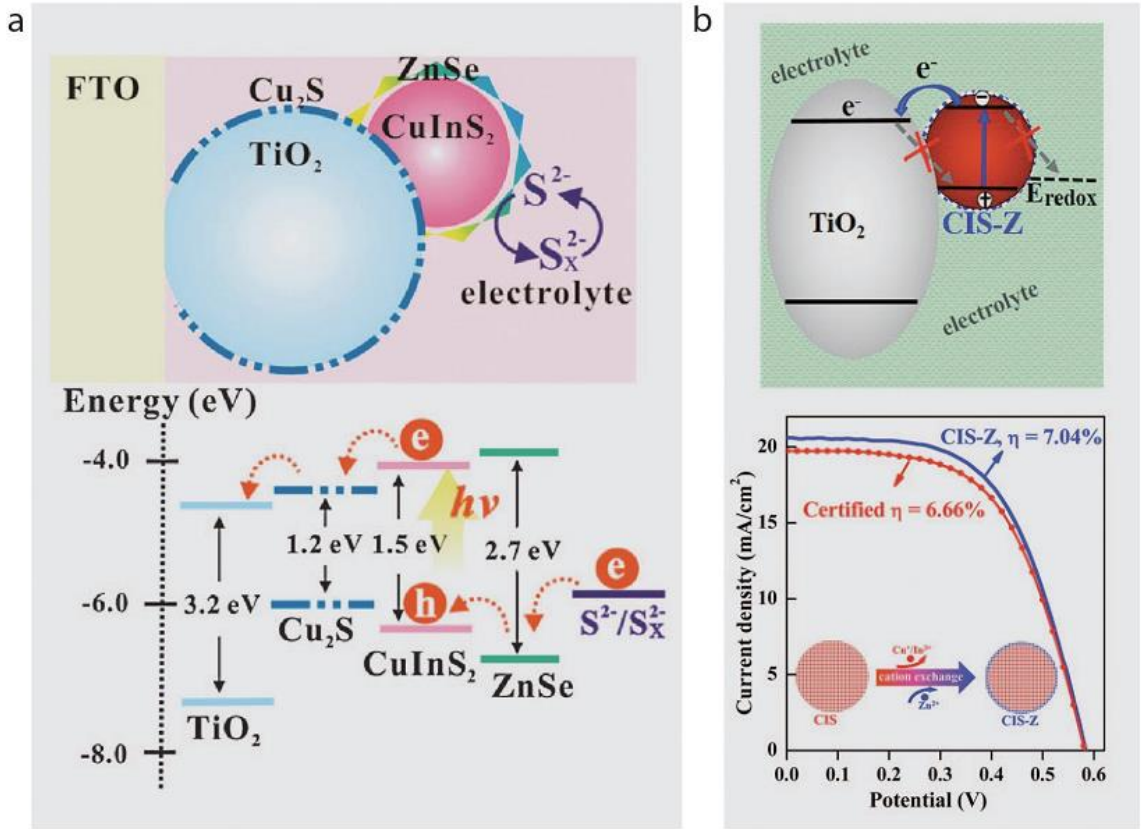


Figure 2.9: Quantum-dot-sensitized solar cells with CIS NCs as sensitizers. (a) The electrons are effectively injected into the TiO_2 particles, whereas the hole is captured by

the electrolyte. In this way, a photocurrent is generated. FTO = fluorine-doped tin oxide [86]. (b) CIS NCs have been shown to be efficient sensitizers in QDSSCs, with a record efficiency of 7.04 % [87].

Other studies showed that use larger crystallite domain sizes improved the performance thus suggesting that longer synthesis period of the nanocrystal is crucial [85]. The use of dye-sensitized solar cell was another way of cutting costs [86 -87]. Previously studies reported the use of Cd and Pd chalcogenides in quantum-dot-sensitized solar cells (QDSSCs) [6]. Recent studies show that the combination of CIS/ZnSe alloyed core–shell NCs with TiO_2 nanoparticles coated with Cu_2S as a buffer layer have shown promising characteristics (Fig. 8a) [86]. Power conversion efficiencies of 7% were obtained by using CIS/ZnS alloyed core–shell NCs as sensitizers on TiO_2 mesoporous films (Fig. 2.9b) [87]. Moreover, using quantum dots (QDs) as a sensitizer can bring distinct advantages for DSSCs, including a tunable absorption spectrum, rapid charge separation, and a low Shockley-Queisser limit [88]. It was also reported that they can be beneficial in large-scale deployment of these PV devices [6].

2.6 References

1. Sagadevan, S., *Rev. Adv. Mater. Sci* **2013,** *34*, 44-61.

2. Arico, A. S.; Bruce, P.; Scrosati, B.; Tarascon, J.-M.; Van Schalkwijk, W., *Nature materials* **2005,** *4* (5), 366-377.

3. Wang, Y.-J.; Wilkinson, D. P.; Zhang, J., *Chemical reviews* **2011,** *111* (12), 7625-7651.

4. Graham-Rowe, D., *Nature Photonics* **2007,** *1* (8), 433-435.

5. Jin, Y.; An, C.; Tang, K.; Huang, L.; Shen, G., *Materials Letters* **2003,** *57* (26), 4267-4270.

6. Van Der Stam, W.; Berends, A. C.; de Mello Donega, C., *ChemPhysChem* **2016**.

7. Birkmire, R. W.; Eser, E., *Annual Review of Materials Science* **1997,** *27* (1), 625-653.

8. (a) Kolny-Olesiak, J.; Weller, H., *ACS applied materials & interfaces* **2013,** *5* (23), 12221-12237; (b) Aldakov, D.; Lefrançois, A.; Reiss, P., *Journal of Materials Chemistry C* **2013,** *1* (24), 3756-3776.

9. Shavel, A.; Cadavid, D.; Ibanez, M.; Carrete, A.; Cabot, A., *Journal of the American Chemical Society* **2012,** *134* (3), 1438-1441.

10. Rath, T.; Haas, W.; Pein, A.; Saf, R.; Maier, E.; Kunert, B.; Hofer, F.; Resel, R.; Trimmel, G., *Solar Energy Materials and Solar Cells* **2012,** *101*, 87-94.

11. Chang, J.; Waclawik, E. R., *CrystEngComm* **2013,** *15* (28), 5612-5619.

12. Zhang, G.; Finefrock, S.; Liang, D.; Yadav, G. G.; Yang, H.; Fang, H.; Wu, Y., *Nanoscale* **2011,** *3* (6), 2430-2443.

13. Urbieta, A.; Fernández Sánchez, P.; Piqueras de Noriega, J., *Journal of applied physics* **2004,** *96* (4), 2210-2213.

14. Ozin, G. A.; Steele, M. R.; Holmes, A. J., *Chemistry of materials* **1994,** *6* (7), 999-1010.

15. Wu, J.-J.; Liu, S.-C., *Advanced Materials* **2002,** *14* (3), 215.

16. Usui, H.; Shimizu, Y.; Sasaki, T.; Koshizaki, N., *The Journal of Physical Chemistry B* **2005,** *109* (1), 120-124.

17. Chang, J.; Waclawik, E. R., *RSC Advances* **2014,** *4* (45), 23505-23527.

18. Faraday, M., *Philosophical Transactions of the Royal Society of London* **1857,** *147*, 145-181.

19. Henglein, A., *The Journal of Physical Chemistry* **1982,** *86* (13), 2291-2293.

20. Rossetti, R.; Brus, L., *The Journal of Physical Chemistry* **1982,** *86* (23), 4470-4472.

21. Murray, C.; Norris, D. J.; Bawendi, M. G., *Journal of the American Chemical Society* **1993,** *115* (19), 8706-8715.

22. van Embden, J.; Chesman, A. S.; Jasieniak, J. J., *Chemistry of Materials* **2015,** *27* (7), 2246-2285.

23. Tao, A. R.; Habas, S.; Yang, P., *small* **2008,** *4* (3), 310-325.

24. Li W.,*Shape Control and Functional Properties of Copper Chalcogenide Colloidal Nanocrystals*, PhD dissertation, Universitat de Barcelona. **2013**.

25. Tao, A.; Sinsermsuksakul, P.; Yang, P., *Angewandte Chemie International Edition* **2006,** *45* (28), 4597-4601.

26. Murphy, C. J.; Jana, N. R., *Advanced Materials* **2002,** *14* (1), 80.

27. Yin, Y.; Alivisatos, A. P., *Nature* **2005,** *437* (7059), 664-670.

28. Vossmeyer, T.; Katsikas, L.; Giersig, M.; Popovic, I.; Diesner, K.; Chemseddine, A.; Eychmüller, A.; Weller, H., *The Journal of Physical Chemistry* **1994,** *98* (31), 7665-7673.

29. Murray, C.; Sun, S.; Doyle, H.; Betley, T., *Mrs Bulletin* **2001,** *26* (12), 985-991.

30. Reiss, H., *The Journal of Chemical Physics* **1951,** *19* (4), 482-487.

31. Peng, X.; Manna, L.; Yang, W.; Wickham, J.; Scher, E.; Kadavanich, A.; Alivisatos, A. P., *Nature* **2000,** *404* (6773), 59-61.

32. Mullin, J. W., *Crystallization*. Butterworth-Heinemann: 2001.

33. Kumar, S.; Nann, T., *Small* **2006,** *2* (3), 316-329.

34. Manna, L.; Scher, E. C.; Alivisatos, A. P., *Journal of the American Chemical Society* **2000,** *122* (51), 12700-12706.

35. Xia, Y.; Xia, X.; Peng, H.-C., *Journal of the American Chemical Society* **2015,** *137* (25), 7947-7966.

36. Peng, Z. A.; Peng, X., *Journal of the American Chemical Society* **2001,** *123* (7), 1389-1395.

37. Peng, Z. A.; Peng, X., *Journal of the American Chemical Society* **2001,** *123* (1), 183-184.

38. Sau, T. K.; Rogach, A. L., *Advanced Materials* **2010,** *22* (16), 1781-1804.

39. Sau, T. K.; Murphy, C. J., *Langmuir* **2004,** *20* (15), 6414-6420.

40. Li, M.; Zhang, Z.; Zhang, X.; Li, K.; Yu, X., *Optics express* **2008,** *16* (18), 14288-14293.

41. Sau, T.; Murphy, C., *Philosophical Magazine* **2007,** *87* (14-15), 2143-2158.

42. Caswell, K.; Bender, C. M.; Murphy, C. J., *Nano Letters* **2003,** *3* (5), 667-669.

43. Matsui, H.; Pan, S.; Douberly, G. E., *The Journal of Physical Chemistry B* **2001,** *105* (9), 1683-1686.

44. Xue, C.; Mirkin, C. A., *Angewandte Chemie* **2007,** *119* (12), 2082-2084.

45. Chen, S.; Fan, Z.; Carroll, D. L., *The Journal of Physical Chemistry B* **2002,** *106* (42), 10777-10781.

46. Zhao, N.; Wei, Y.; Sun, N.; Chen, Q.; Bai, J.; Zhou, L.; Qin, Y.; Li, M.; Qi, L., *Langmuir* **2008,** *24* (3), 991-998.

47. Sau, T. K.; Murphy, C. J., *Journal of the American Chemical Society* **2004,** *126* (28), 8648-8649.

48. Liu, X.; Huang, R.; Zhu, J., *Chemistry of Materials* **2007,** *20* (1), 192-197.

49. Petrova, H.; Lin, C.-H.; Hu, M.; Chen, J.; Siekkinen, A. R.; Xia, Y.; Sader, J. E.; Hartland, G. V., *Nano letters* **2007,** *7* (4), 1059-1063.

50. Scholes, G. D., *Advanced Functional Materials* **2008,** *18* (8), 1145-1145.

51. Lofton, C.; Sigmund, W., *Advanced Functional Materials* **2005,** *15* (7), 1197-1208.

52. Sun, Y.; Mayers, B.; Herricks, T.; Xia, Y., *Nano letters* **2003,** *3* (7), 955-960.

53. Johnson, C. J.; Dujardin, E.; Davis, S. A.; Murphy, C. J.; Mann, S., *Journal of Materials Chemistry* **2002,** *12* (6), 1765-1770.

54. Gai, P. L.; Harmer, M. A., *Nano Letters* **2002,** *2* (7), 771-774.

55. Jiang, X.; Zeng, Q.; Yu, A., *Langmuir* **2007,** *23* (4), 2218-2223.

56. Zeng, Q.; Jiang, X.; Yu, A.; Lu, G. M., *Nanotechnology* **2007,** *18* (3), 035708.

57. Seidensticker, R.; Hamilton, D., *Journal of Applied Physics* **1963,** *34* (10), 3113-3119.

58. Goessens, C.; Schryvers, D.; Landuyt, J. V., *Microscopy research and technique* **1998,** *42* (2), 85-99.

59. Chang, J.; Ahmed, R.; Wang, H.; Liu, H.; Li, R.; Wang, P.; Waclawik, E. R., *The Journal of Physical Chemistry C* **2013,** *117* (27), 13836-13844.

60. Chang, J.; Waclawik, E. R., *CrystEngComm* **2012,** *14* (11), 4041-4048.

61. Bai, J.; Qin, Y.; Jiang, C.; Qi, L., *Chemistry of materials* **2007,** *19* (14), 3367-3369.

62. Sun, Y.; Mayers, B.; Xia, Y., *Nano Letters* **2003,** *3* (5), 675-679.

63. Zhang, J.; Liu, H.; Wang, Z.; Ming, N., *Applied Physics Letters* **2007,** *91* (13), 133112.

64. Germain, V.; Li, J.; Ingert, D.; Wang, Z.; Pileni, M., *The Journal of Physical Chemistry B* **2003,** *107* (34), 8717-8720.

65. Choi, K.-S., *Dalton Transactions* **2008,** (40), 5432-5438.

66. Brus, L., *The Journal of chemical physics* **1983,** *79* (11), 5566-5571.

67. Brus, L., *The Journal of Physical Chemistry* **1986,** *90* (12), 2555-2560.

68. Burda, C.; Chen, X.; Narayanan, R.; El-Sayed, M. A., *Chemical reviews* **2005,** *105* (4), 1025-1102.

69. Jaffe, J.; Zunger, A., *Physical Review B* **1983,** *28* (10), 5822.

70. Debnath, T.; Maiti, S.; Maity, P.; Ghosh, H. N., *The journal of physical chemistry letters* **2015,** *6* (17), 3458-3465.

71. Yarema, O.; Bozyigit, D.; Rousseau, I.; Nowack, L.; Yarema, M.; Heiss, W.; Wood, V., *Chemistry of Materials* **2013,** *25* (18), 3753-3757.

72. Li, L.; Pandey, A.; Werder, D. J.; Khanal, B. P.; Pietryga, J. M.; Klimov, V. I., *Journal of the American Chemical Society* **2011,** *133* (5), 1176-1179.

73. Omata, T.; Nose, K.; Kurimoto, K.; Kita, M., *Journal of Materials Chemistry C* **2014,** *2* (33), 6867-6872.

74. Kraatz, I. T.; Booth, M.; Whitaker, B. J.; Nix, M. G.; Critchley, K., *The Journal of Physical Chemistry C* **2014,** *118* (41), 24102-24109.

75. Knowles, K. E.; Nelson, H. D.; Kilburn, T. B.; Gamelin, D. R., *Journal of the American Chemical Society* **2015,** *137* (40), 13138-13147.

76. Shabaev, A.; Mehl, M.; Efros, A. L., *Physical Review B* **2015,** *92* (3), 035431.

77. Musselman, K. P.; Schmidt-Mende, L., *Green* **2011,** *1* (1), 7-27.

78. Mitzi, D. B.; Gunawan, O.; Todorov, T. K.; Wang, K.; Guha, S., *Solar Energy Materials and Solar Cells* **2011,** *95* (6), 1421-1436.

79. Niezgoda, J. S.; Harrison, M. A.; McBride, J. R.; Rosenthal, S. J., *Chemistry of Materials* **2012,** *24* (16), 3294-3298.

80. Witt, E.; Kolny-Olesiak, J., *Chemistry – A European Journal* **2013,** *19* (30), 9746-9753.

81. Dilena, E.; Xie, Y.; Brescia, R.; Prato, M.; Maserati, L.; Krahne, R.; Paolella, A.; Bertoni, G.; Povia, M.; Moreels, I., *Chemistry of Materials* **2013,** *25* (15), 3180-3187.

82. Wang, W.; Winkler, M. T.; Gunawan, O.; Gokmen, T.; Todorov, T. K.; Zhu, Y.; Mitzi, D. B., *Advanced Energy Materials* **2014,** *4* (7).

83. Stolle, C. J.; Harvey, T. B.; Korgel, B. A., *Current Opinion in Chemical Engineering* **2013,** *2* (2), 160-167.

84. Draguta, S.; McDaniel, H.; Klimov, V. I., *Advanced Materials* **2015,** *27* (10), 1701-1705.

85. Collord, A. D.; Hillhouse, H. W., *Solar Energy Materials and Solar Cells* **2015,** *141*, 383-390.

86. Chang, J.-Y.; Su, L.-F.; Li, C.-H.; Chang, C.-C.; Lin, J.-M., *Chemical Communications* **2012,** *48* (40), 4848-4850.

87. Pan, Z.; Mora-Seró, I. n.; Shen, Q.; Zhang, H.; Li, Y.; Zhao, K.; Wang, J.; Zhong, X.; Bisquert, J., *Journal of the American Chemical Society* **2014,** *136* (25), 9203-9210.

88. Gao, M.-R.; Xu, Y.-F.; Jiang, J.; Yu, S.-H., *Chemical Society Reviews* **2013,** *42* (7), 2986-3017.

Chapter 3: Colloidal synthesis of pure $CuInTe_2$ crystallites based on the HSAB theory

3.1 Introduction

With increasing interest in fabricating low cost photovoltaic devices, much attention has been focused on exploiting the use of Cu-III-IV_2 chalcopyrite based semiconductor materials as effective light absorber layers in thin-film solar cells [1]. This is due to their unique energy band gap and other advantages such as high absorption coefficient, high radiation stability, exceptional radiation hardness and defect tolerance [2]. Among the various Cu-based ternaries, selenides and sulfides have been well explored [2]. Solar-energy conversion efficiencies of about 20% and 12% have already been reported for $CuInSe_2$ and $CuInS_2$ respectively [3]. Although $CuInSe_2$ and $CuInS_2$ have been extensively studied not much attention has been paid to studies on tellurides in general and particularly $CuInTe_2$ [2].

$CuInTe_2$ has a direct band gap in the range of 0.92 and 1.06 eV and an absorption coefficient of more than 10^5 cm^{-1} near the band edge [4]. It exhibits a stronger quantum confinement effect and a larger Bohr radius than $CuInS_2$ and $CuInSe_2$, owing to the covalent property of tellurium[5]. Though $CuInTe_2$ has distinct combination of pertinent characteristics making them suitable for use in solar cells as absorbers, synthesis of these materials involves complex and expensive processes [4]. Boustani et al. prepared $CuInTe_2$ films by thermal evaporation from a single source [6]. Roy et al. also prepared $CuInTe_2$ films by a three source co-evaporation technique[7]. In an attempt to cut costs posed by vacuum based processes, various methods such as solvothermal synthesis, microwave irradiation, polyol synthesis, silicate matrix method and the conventional colloidal method have been adopted [8-9]. Recently, Kim et al. synthesized $CuInTe_2$ particles using the solvothermal method [10].

During the synthesis, prolonged reaction times and various temperatures were explored to obtain the materials [10]. Contrary to prolonged reaction times, Malik and co-workers reported significantly shorter reaction times for $CuInSe_2$ via the colloidal synthesis [11] .

Crystallization is one of few most interesting yet mysterious processes; however it is an important process to understand and influences the ease with which a product is obtained. The first and probably the most critical step of crystallization is nucleation. Nucleation refers to the initial formation process of a crystal phase from another phase, usually a liquid, a solution, or a gas phase. Nucleation defines the boundary conditions for a given crystallization system and most likely dictates the following growth process under given temperature and pressure [12]. Unfortunately, understanding the nucleation process is a big challenge mostly because of the difficulty to quantitatively determine the size and concentration of the newly formed tiny clusters. Substantial progress made in colloidal synthesis has shown that key controllable parameters such as temperature, reaction time and the use of coordinating or non-coordinating solvents are essential for controlling the nucleation process and will result in size-tunable properties, morphology, structure and stoichiometry properties which can be used to shift absorption [13]. Although colloidal syntheses has been proven to be cheap and efficient for synthesizing Cu-III-IV_2 semiconductors, very little work has been reported on the colloidal synthesis of $CuInTe_2$. Herein, a conventional colloidal method was conducted to synthesize $CuInTe_2$ crystallites. Temperature as a factor that has big influence on crystallization was studied. In addition, the effect of varying the sequence of adding the precursors to the reaction mixture was also studied. The optical properties of the crystallites were determined to estimate the use of the material in photovoltaics applications as absorber layer.

3.2 Experimental

3.2.1 Materials and reagents

Copper (I) chloride (CuCl), Indium (III) chloride ($InCl_3$), and elemental tellurium (Te) were all purchased from Sigma Aldrich. Trioctylphosphine (TOP), oleylamine (OLA), dichloromethane (CH_2Cl_2), chloroform ($CHCl_3$), methanol (CH_3OH) and ethanol (C_2H_6O) were all purchased from Sigma Aldrich and used without further purification.

3.2.2 Synthesis of $CuInTe_2$

Two methods were employed for the synthesis of $CuInTe_2$. In method 1, 2.5 mmol of copper chloride and 2.5 mmol of indium chloride were added to 7 mL of OLA and heated to 120 °C under nitrogen. The mixture was then left under vacuum for 20 min before 2 mL of TOPTe (1 M) was injected. The solution was then further heated to 190 °C for 30 min. The temperature was then decreased to 60 °C. Methanol was added to the solution to flocculate the particles. The particles were then collected through centrifugation at 3000 rpm and washed with dichloromethane, ethanol, and methanol to remove the impurities. The temperature was varied from 190 °C – 250 °C. In method 2, the sequence of addition of precursors was changed. Typically, 2.5 mmol of indium chloride was first added to 7 mL of OLA and heated to 120 °C under nitrogen. The mixture was then left under vacuum for 20 min. Thereafter, 2 mL of 1 M TOPTe was added. The solution was then further heated to 250 °C at which point 2.5 mmol of copper chloride dissolved in 2 mL of OLA was quickly injected. The temperature was maintained at 250 °C for 30 min. The particles were then collected and washed following the previous procedure.

3.2.3 Characterization

XRD patterns on powdered samples were measured on a Bruker MeasSrv D2-205530 diffractometer using secondary graphite monochromated CoKα radiation (λ 1.78897 Å) at 30 kV/30 mA. Measurements were taken using a glancing angle of incidence detector at an angle of 2°, for 2θ values over 20 - 90° in steps of 0.026° with a step time of 37 s and at a temperature of 25 °C. Raman spectroscopy in which the 514 nm emission line from an argon laser done in conjunction with a Horiba Jobin-Yvon LabRAM HR Raman spectrometer was used. The transmission electron microscopy (TEM) was carried out on a FEI Technai T12 TEM microscope with an EDS detector operated at an acceleration voltage of 200 kV with a beam spot size of 20 - 100 nm in TEM mode. UV-vis to near-Infra Red spectra of the powered samples was acquired by Praying Mantis DRS Cary 500.

3.3 Results and discussion

3.1 Effect of temperature on the formation of $CuInTe_2$

3.1.1 XRD studies

In order to study the formation process of $CuInTe_2$, temperature studies were done on particles synthesized using method 1. Fig. 1 shows the XRD patterns of the synthesized materials at different temperatures. At 190 °C a pronounced (111) peak at 32° 2θ of the tellurium hexagonal phase (PDF #:00-036-1452) was seen indicating a preferred orientation along this plane. At this temperature only a tellurium phase was detected, indicating no formation of binary or ternary phases. This suggested that the reaction temperature was fairly low to facilitate the reaction with the metal salts [10]. Similarly Kim et al. also observed a tellurium hexagonal phase at 200 °C which was attributed to a low reaction temperature and the same phase was detected when the reaction was conducted over a prolonged period [10].

Formation of tellurium crystallites therefore was indicative of unformed copper and indium ion monomers during the reaction due to unreacted precursors.

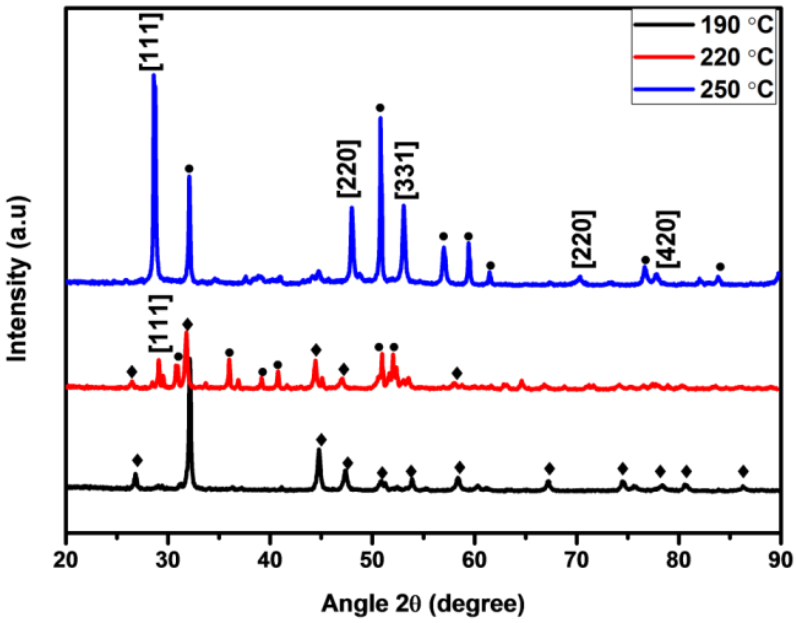


Figure 3.1: XRD patterns of crystallites synthesized using method 1 at various temperatures where ♦ = Te phase and ● = Cu_5Te_3.

As the temperature was further increased to 220 °C, the (111) peak at 32° 2θ became less intense indicating that the formation of a tellurium phase was gradually disappearing. The less intense peak at 29.2° 2θ (PDF#: 00-026-1117) corresponding to the $CuInTe_2$ phase was observed. Tellurium and binary Cu_5Te_3 phases were predominant. These findings were in agreement with those of Kim et al. who obtained a mixture of $CuInTe_2$ and Te phases after carrying a solvothermal reaction for 6 hrs [10].

At 250 °C, the $CuInTe_2$ chalcopyrite phase was the major phase corresponding to the (111) at 28.5° 2θ, (220) at 48° 2θ, (311) 57° 2θ, (222) at 70.3° 2θ and (420) at 78.1° 2θ planes. However, the formation of a secondary phase of Cu_5Te_3 was also observed. Similar results have been reported in literature at temperatures of 260 °C and extended reaction times [10, 14].

Formation of secondary phases can be attributed to the difference in stability or reactivity of Cu^{+1} and In^{+3} ions. Based on the Hard and Soft Acid Base (HSAB) theory, Cu^{+1} is a soft acid while S^{-2}, Se^{-2} and Te^{-2} are known to be soft bases. According to the theory, soft acids will tend to react more readily with soft bases [14-15]. In the present study formation of binary tellurium compounds can be attributed to the strong affinity of Cu^{+1} ions as soft acids to Te^{-2} ions as soft bases. They react fast and form stronger bonds thus hindering bond formation between indium and tellurium.

3.1.2 Raman studies

Raman spectroscopy involves the inelastic scattering of monochromatic laser light by molecules. Energy from the laser interacts with the molecules in such a way that the scattered light photons have a higher or lower energy than the incident photons. The difference in energy is due to a change in the rotational and vibrational energy of the molecule and gives valuable molecular information. Since different molecules show different energy changes, the Raman technique can be used as a fingerprinting technique for the determination of molecular structure, for locating various chemical bonds or functional groups in molecules and for the quantitative analysis of complex mixtures. A feature of Raman scattering is that each line has a characteristic polarization, and polarization data can provide additional information about molecular structure [16].

The Raman spectra of particles synthesized at different temperatures using method 1 are shown in Fig. 3.2. The acquired spectra of materials synthesized at 190 °C and 220 °C showed two similar peaks at 117 cm^{-1} and 140 cm^{-1}. The observed peaks were attributed to the A_1 and E vibrational modes of tellurium. A slight shift was observed from the reported

values of 120 cm^{-1} and 139 cm^{-1} [16]. This slight frequency shift may be due to bond-stretching forces between the nearest-neighbor atoms [17].

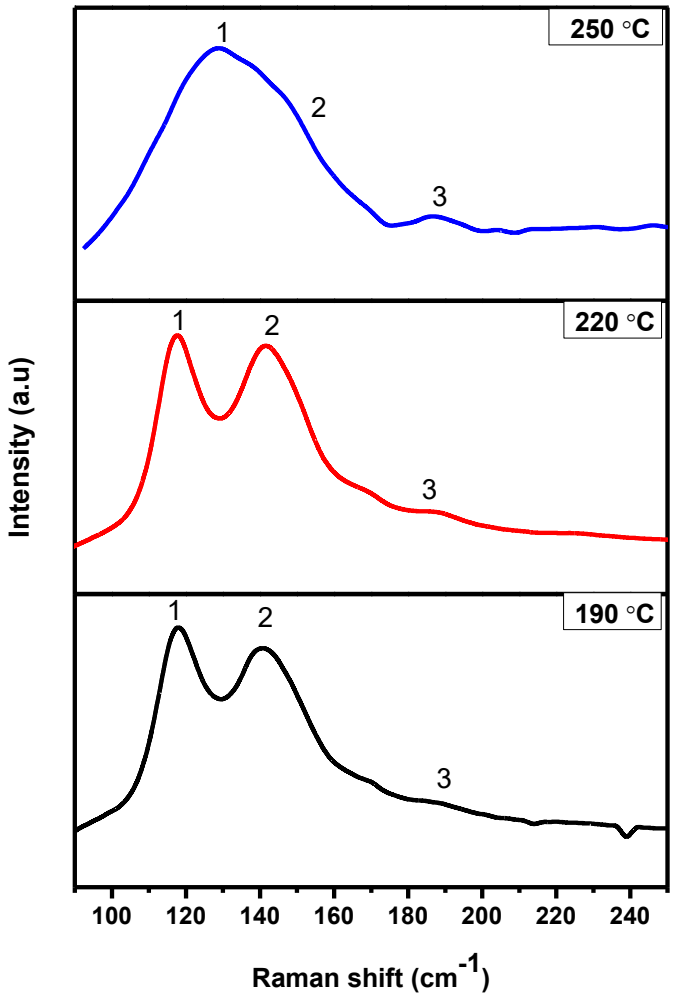


Figure 3.2: Raman spectra of crystallites synthesized using method 1 at various temperatures.

Furthermore there was a shoulder peak observed at 188 cm^{-1} assigned to the E mode [16]. The Raman spectrum of particles synthesized at 220 °C was similar to those synthesized at 190 °C. The A_1 vibrational mode of copper telluride usually observed at 259 cm^{-1} originating from the motion of the Te atom with the Cu atom was not seen [18]. This suggested that there was relatively a small amount of copper telluride particles as compared to tellurium particles.

A similar observation was seen in the X-ray diffraction pattern in Fig. 1 where the major peaks were associated with tellurium. The characteristic A_1 mode of chalcopyrite at 127 cm^{-1} due to the in-plane motion of Te atoms with cations at rest was not observed for both materials at 190 °C and 220 °C [19]. For particles synthesized at 250 °C, only two peaks were observed. The broad peak was deconvulated to two peaks located at 129 cm^{-1} and 149 cm^{-1}. These peaks were attributed to the A_1 and B_1 vibrational modes of chalcopyrite $CuInTe_2$ respectively [20]. The small peak marked as at 188 cm^{-1} was associated with the E vibrational mode of Te.

3.1.3 Microscopy analysis at various reaction temperatures

The morphology of the materials synthesized at different temperatures was evaluated with TEM. TEM micrographs of the materials are shown in Fig. 3. A mixture of cylindrical and spherical shaped particles was observed at 190 °C with spheres being dominant. The particles were polydispersed, with sizes well over a 100 nm. As the temperature was increased to 220 °C a mixture of rods and spheres was seen with rods being dominant. Based on the XRD results in Fig. 1 and the abundance of the rods, it may be deduced that the rod particles are Cu_5Te_3, as this was the most dominant phase. A further increase in temperature to 250 °C resulted in cubic structures. The crystallites were polydispersed. A few rod shape particles were detected with the majority of the sample made up cubic particles. This was again consistent with the XRD data where a mixture of $CuInTe_2$ together with Cu_5Te_3 was observed. It therefore became evident that $CuInTe_2$ gave rise to cube-like morphology.

190 °C

220 °C

250 °C

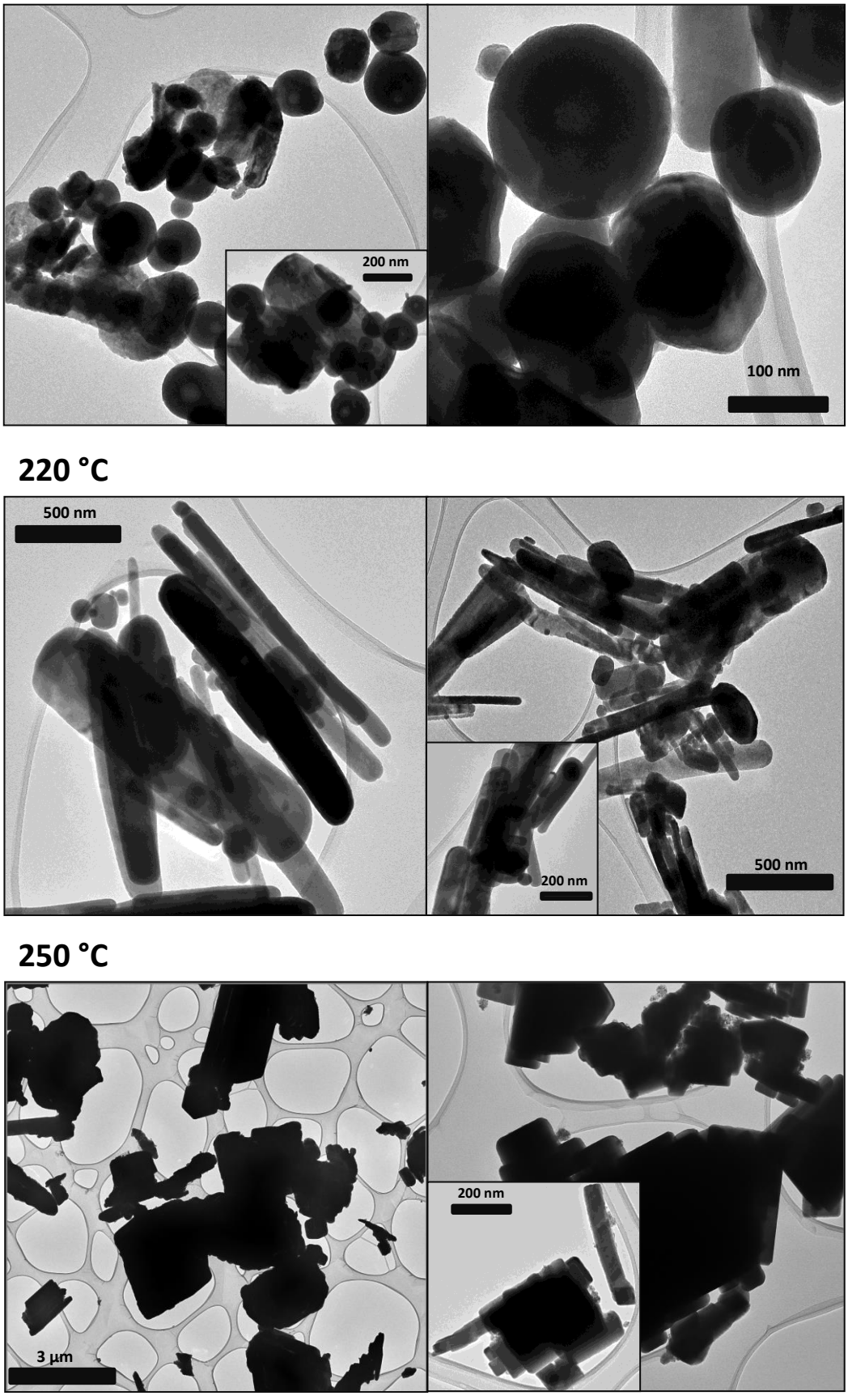


Figure 3.3: TEM micrographs of crystallites synthesized using method 1 at 250 °C.

3.2 Effect of order of precursor addition

Previously it has been reported that synthesis of ternary compounds usually yield either binary products or additional phases as impurities and these impurities hinder the use of these materials in any application more so in devices. Recently, Guo et al. demonstrated that the order of precursor addition in $CuInSe_2$ synthesis via colloidal method is of great importance as it determines the formation pathway of the nanocrystals and allows control over the crystal structure of the particles [21]. For instance, chalcopyrite $CuInSe_2$ was formed when all the precursors were added simultaneously whilst the less stable phase of sphalerite was formed when the selenium precursor was injected later at a higher temperature. The consequence of the order/time of precursor addition resulted in particles with different morphologies and properties [21]. Herein, it was clear that the ideal temperature was 250 °C as attempted reactions at higher temperatures yielded a cocktail of different compounds. Furthermore, at temperatures higher than 250 °C, OLA began to thermally decomposing. Since Cu_5Te_3 was still detected at 250 °C, the effect of the order of precursor addition was investigated. The rationale behind this was that based on the HSAB theory, tellurium will always have a higher affinity for copper, hence by tempering with this, it may be possible to eliminate the formation of Cu_5Te_3. Consequently the indium precursor and the tellurium precursor were first added to allow for them to react. Then the copper precursor was injected at 250 °C and the particles were allowed to grow. This “hot injection” of CuCl induces abrupt supersaturation of the reaction mixture. The supersaturation results in rapid nucleation and growth of the particles which result in the formation of the ternary phase.

3.2.1 XRD studies

A powder X-ray diffraction pattern of the resultant particles is shown in Fig. 3.4. This is compared to the particles synthesized by method 1. The XRD pattern showed no evidence of

binary phases and this can be clearly seen when compared to the particles prepared by method 1. Thus only pure $CuInTe_2$ was detected when using method 2. The sample was indexed as a tetragonal crystal phase with the diffraction characteristic peaks of (111), (220), (311), (222) and (420) planes at 2θ values of 29,2°, 48,6°,57,6°,71,0° and 78,8° respectively and this was in good agreement with the reference data for $CuInTe_2$ (PDF#:01-0703086).

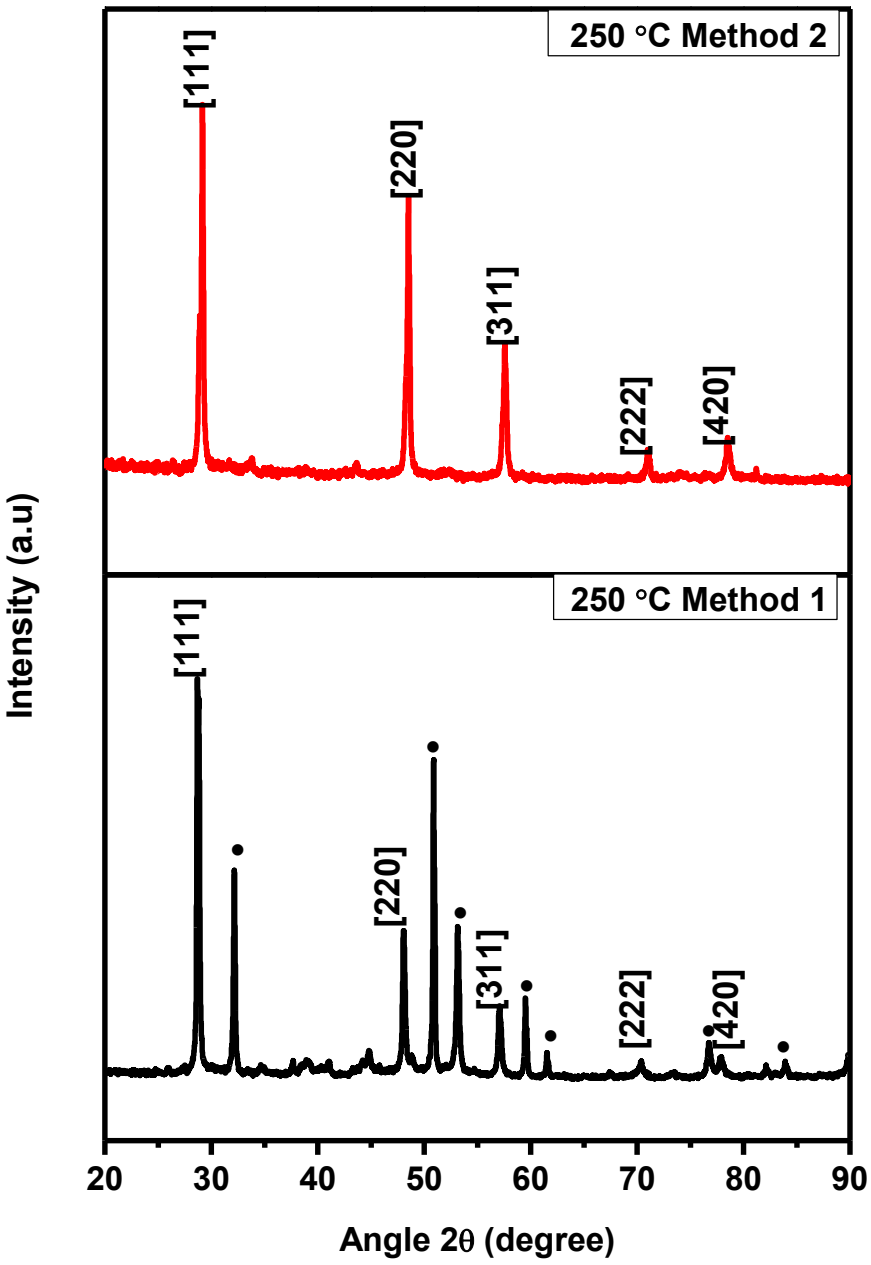


Figure 3.4: XRD patterns of $CuInTe_2$ crystallites synthesized at 250 °C using method 1 and 2, where ● = Cu_5Te_3.

3.2.2 Raman studies

Tetragonal chalcopyrite structure of $CuInTe_2$ has a primitive cell that contains eight atoms. This gives rise to 24 vibrational modes where 3 are acoustic and 21 are optical [17]. These optical modes transform as $1A_1 + 2A_2 + 3B_1 + 3B_2 + 6E$ where all the modes are Raman-active except the A_2 mode which is optically inactive [10, 22, 23,19, 23]. The Raman spectra of the $CuInTe_2$ crystals synthesized by the two methods are shown in Fig. 3.5. The spectra show distinct difference with the one obtained using method 1 showing only two vibrational peaks associated with $CuInTe_2$ and one associated with an impurity. It is therefore evident that the particles synthesized via method 2 are purer and contain only $CuInTe_2$ particles as more vibrations can be perturbed. The lines observed in the spectrum of particles synthesized by method 2 and their symmetry assignments are given in Table 3.1. Five vibrational modes were observed due to the wavelength range. All lines recorded appeared at slightly higher frequencies as compared to ref [19], except for E^6 mode which appeared at a lower frequency.

Table 3.1: Frequency of the phonon modes in the Cu–In–Te system observed in the present work and Ref [19] and their possible symmetry assignment

Line number	[a]$CuInTe_2$ (cm^{-1})	[b]$CuInTe_2$ (cm^{-1})	Symmetry Assignment
1	131	127	A_1
2	149	147	B_1
3	175	170	E^5 and or $B_2{}^3$
4	216	220	E^6 or $[B_2 + E^4]$
5	244	237	$B_2 + E^3$

a = present study, b = ref [19]

Miller et al. also reported shifts to higher frequencies for $HgIn_2Te_4$ chalcopyrite particles [24]. The shifts were attributed to the assumption made during calculations that the vacancy–anion force constant was zero however this was later proven to be non-negligible [24]. Therefore the shifts to higher frequencies suggested that cation vacancy was not an empty site in the lattice but rather a localized region with a positive potential thereby attracting the valence electrons of the surrounding anions. It was also indicative of the difference in magnitude of vacancy-Te and Cu-Te stretching force constant [20].

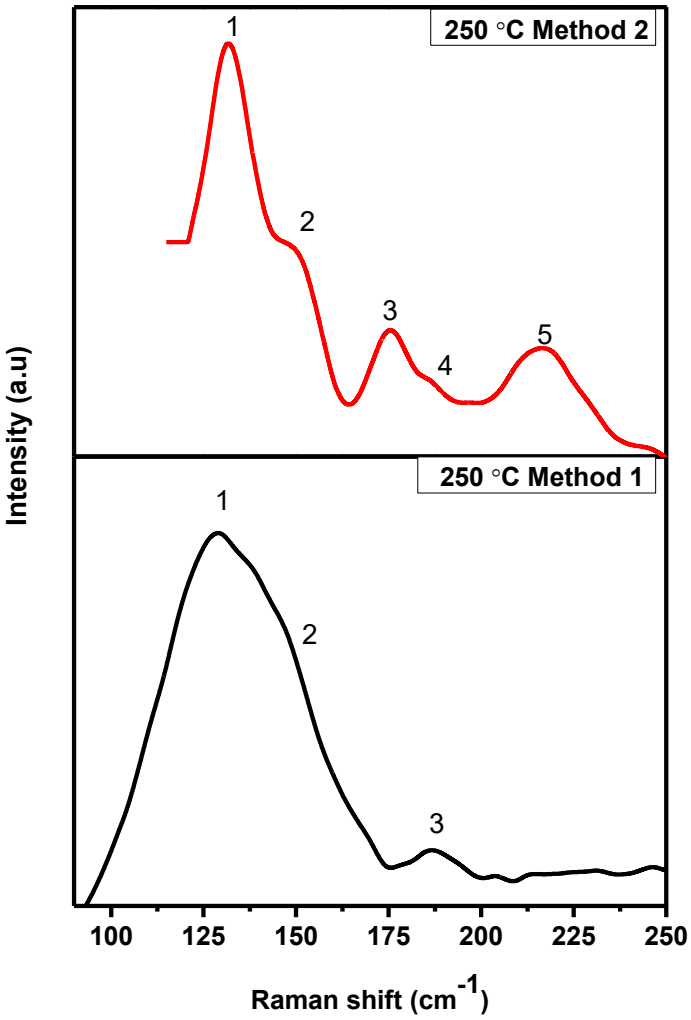


Figure 3.5: Raman spectra of $CuInTe_2$ crystallites synthesized at 250 °C using method 1 and 2.

At 131 cm^{-1} the most intense line was observed corresponding to the A_1 mode that is due to the motion of Te with Cu and In at rest [25]. A weak B_1 mode was observed at 149 cm^{-1} arising from the motion of Cu and In moving in antiphase [26]. This mode was weak due to the change in polarizability resulting from the stretching of the Cu-Te bond compensated by the compression of the In-Te bond [26]. The line observed at 149 cm^{-1} has been previously observed at 148 cm^{-1} for $CuInTe_2$ [20]. The highest phonon modes at 216 and 244 cm^{-1} are attributed to the combination of B_2 and E mode.

2.2.3 Optical analysis

As previously suggested that $CuInTe_2$ could also be promising as absorber layer in photovoltaic applications, the optical measurements of the crystallites were conducted. The optical properties of the material synthesized at 250 °C via method 1 and 2 were examined. The absorption spectra of the material are shown in Fig. 6. From the absorbance measurements the optical band gap of the material was obtained by Kubelka-Munk which allows to extract Eg of the powered semiconductor material unambigiouslly. By converting absorbance to reflectance using equation:

$$A = Log\ \frac{1}{R} \qquad (3.1)$$

Where A is absorbance and R is reflectance. Hence R becomes:

$$R = \frac{1}{10^A} \qquad (3.2)$$

Thereafter Kubelka-Munk function, *F(R)*, which allows the optical absorbance of a sample to be approximated from its reflectance was applied [27].

$$F(R) = \frac{(1-R)^2}{2R} \qquad (3.3)$$

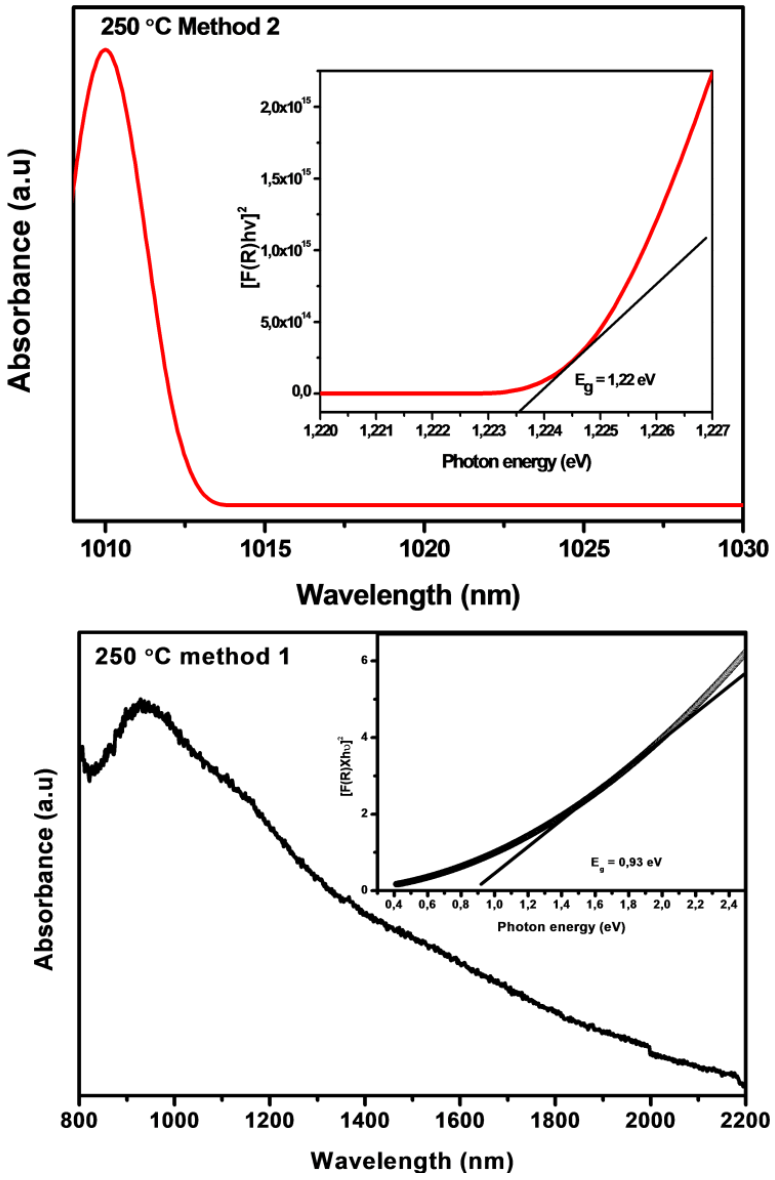


Figure 3.6: UV–Vis–NIR absorbance spectra and optical bands (insets) gaps of $CuInTe_2$ crystallites synthesized at 250 °C using method 1 and 2.

The above equation 3 allows a plot of $[F(R)X\ hv]^{1/n}$ versus photon energy hv where n is a constant determined by the nature of the transition that the sample undergoes. The values of n are 1/2, 3/2, and 2 for allowed direct transitions, forbidden direct transitions, and allowed indirect transitions respectively. Because $CuInTe_2$ is known to be a material with a direct band gap [26], n should be ½. By extrapolating a straight line portion of the graph to hv x-

axis optical band gap of the material was determined. The deduced optical band gap of the crystallites synthesized by method 1 is 0.93 eV corresponding to the band edge of 1322 nm. This agrees with gap energy determinations from optical absorption measurements and photoconductivity spectra [28]. The band gap energy observed is due to the transition of electrons from the shallow acceptor level to the conduction band [29]. Shallow acceptor levels have been observed in several Cu-III-VI_2 compounds [29]. Sridevi et.al reported band gap of 0.94 eV resulting from the shallow acceptor transitions for $CuInTe_2$ thin films [29]. The transitions were attributed to the presence of copper vacancies (V_{cu}) and antisite defects of indium on copper sites (ln_{cu}) [29]. Contrary to this Wasim et.al and colleagues argued that shallow acceptor levels were not due to the Cu vacancy rather Te vacancies [30]. They argued that if shallow acceptor levels were due to Cu vacancy, the absorption energy of the material with Cu excess and Cu deficient in its stoichiometric would differ which was not the case [30]. They attributed the transitions to high hole concentration which has Te vacancy in the material [30]. Furthermore, a decrease in the acceptor ionization energy due to screening effect evidently showed that the shallow acceptor level observed in $CulnTe_2$ is due to Te vacancies [30]. This is in agreement with covalent bonding model under which both the anion interstials and vacancies should act as acceptors [30]. However, in the present case more studies are required to confirm the defect present in the crystallites. Employing method 2 resulted in increased band gap of 1.22 eV and band egde decreased to 1016 nm. This is similar to the reported band gap of 1.26 eV for polycrystalline thin films of $CuInTe_2$ [29]. The transition is due to spin-orbit interactions in the d level [29].

3.2.4 Morphological analysis

The TEM images of particles synthesized via method 2 are shown in Fig. 3.7. Cubic particles were observed however, a high degree of agglomeration was also observed. Nevertheless, the particles seemed to be more homogeneous than those synthesized by method 1 (Fig 3.8). There was also no evidence of rod shaped particles further suggesting that method 2 resulted in the formation of only $CuInTe_2$. This was consistent with the XRD and Raman data. The particles were however still large. The size of the seen cubic particles varies from small to large. The insets in Fig 3.7 d) and Fig 3.8 d) reveal the lattice fringes of the cubed particles with interatomic distance of 3.58 Å and 3.57 Å for particles synthesized via method 2 and 1 respectively. The insignificant change in the interatomic distance is indicative of the similar phases. The calculated d-spacing correspond to the (111) peak at 29.2° 2θ. Therefore confirming that the cubed particles formed in both methods 1 and 2 is $CuInTe_2$ phase. Elemental analysis (Fig 3.9) also confirmed formation $CuInTe_2$ phase in both method 1 and 2. There was also no evidence of rod shaped particles further suggesting that method 2 resulted in the formation of only $CuInTe_2$. This was consistent with the XRD and Raman data. However, C and Be peaks are also detected which could be from the detector of the instrument. Further investigations are therefore being undertaken where parameters such as concentration, time and type of capping agent are being investigated

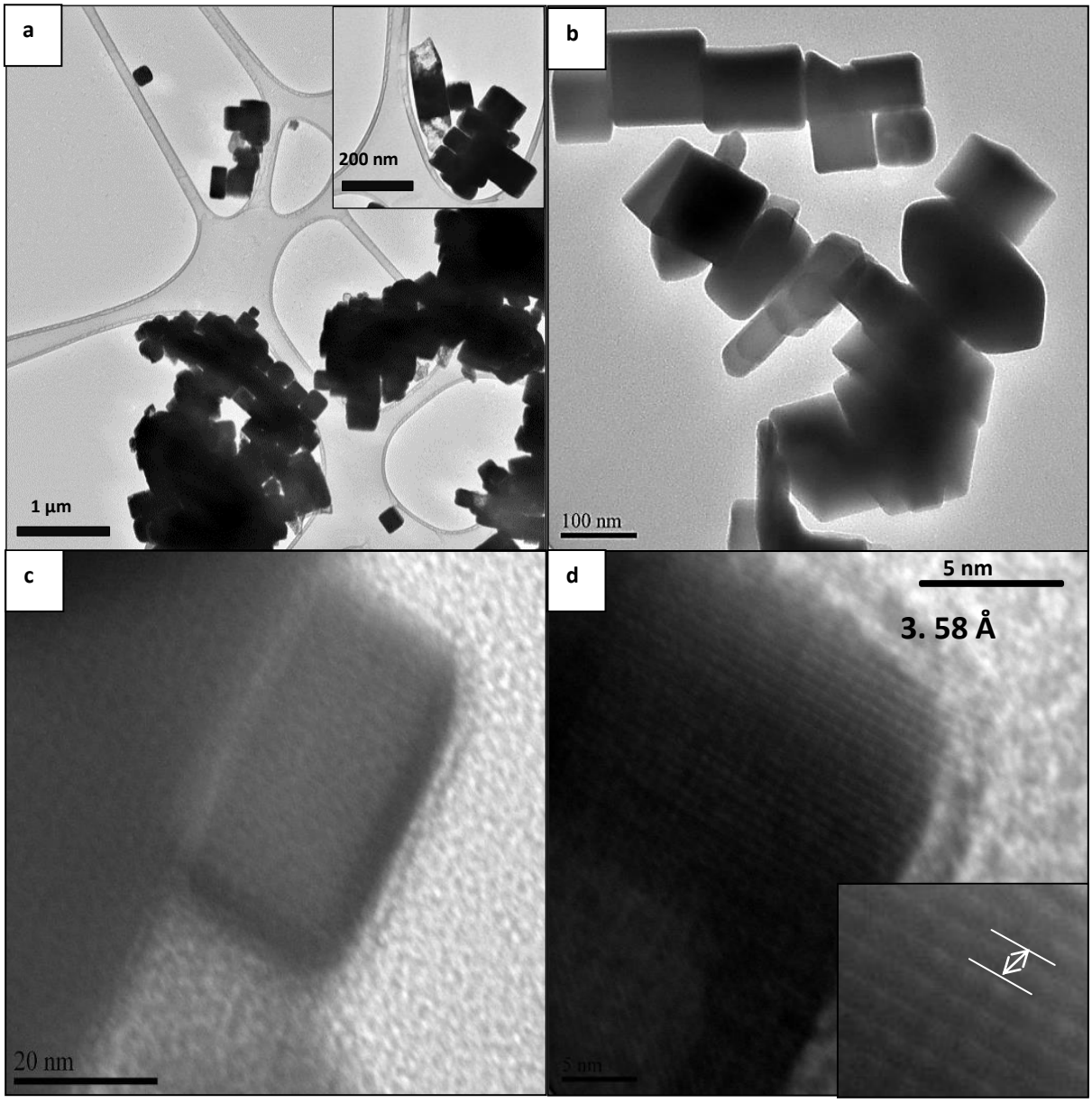


Figure 3.7: TEM and HRTEM micrographs of $CuInTe_2$ crystallites synthesized at 250 °C using method 2.

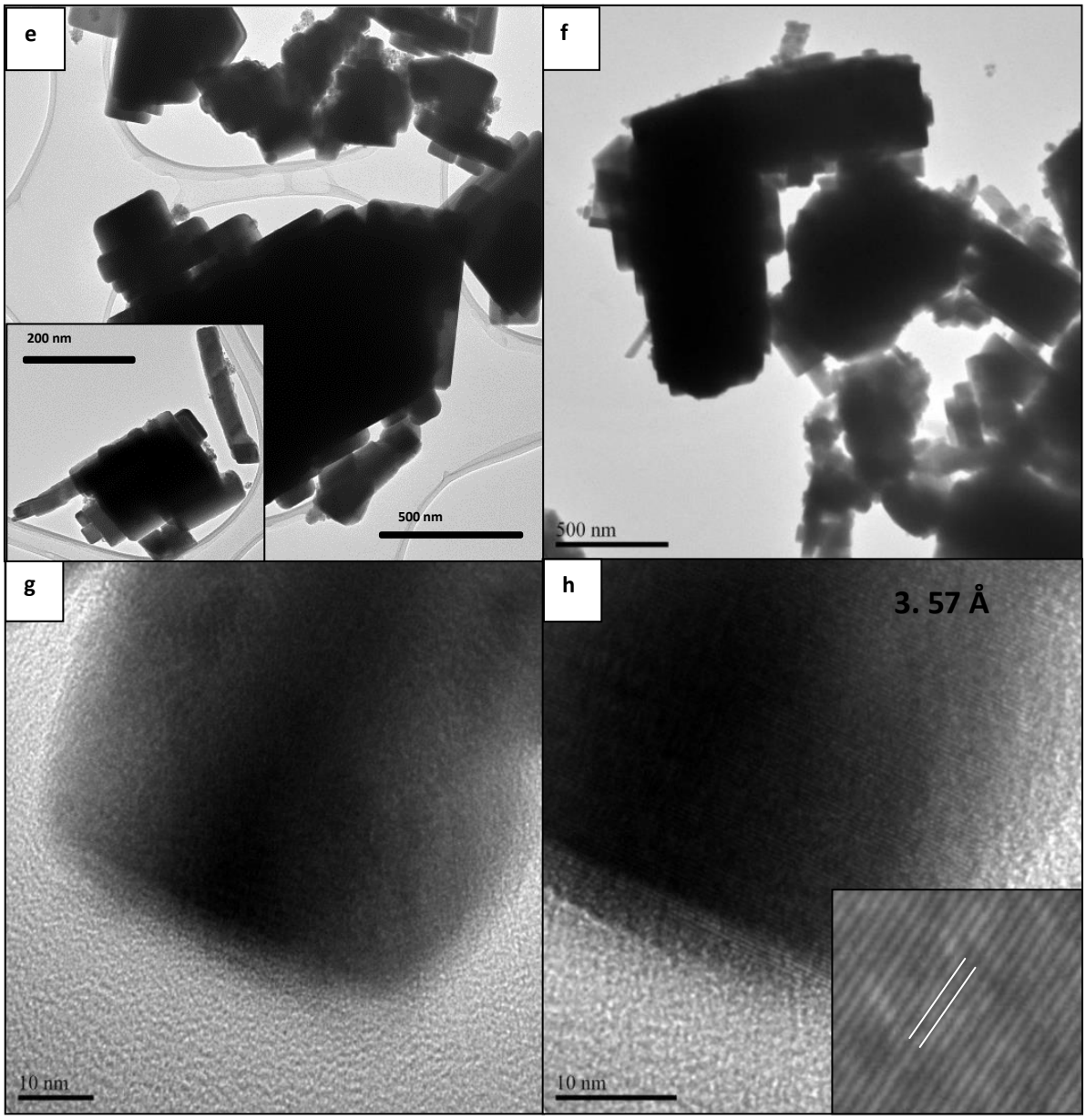


Figure 3.8: TEM and HRTEM micrographs of $CuInTe_2$ crystallites synthesized at 250 °C using method 1.

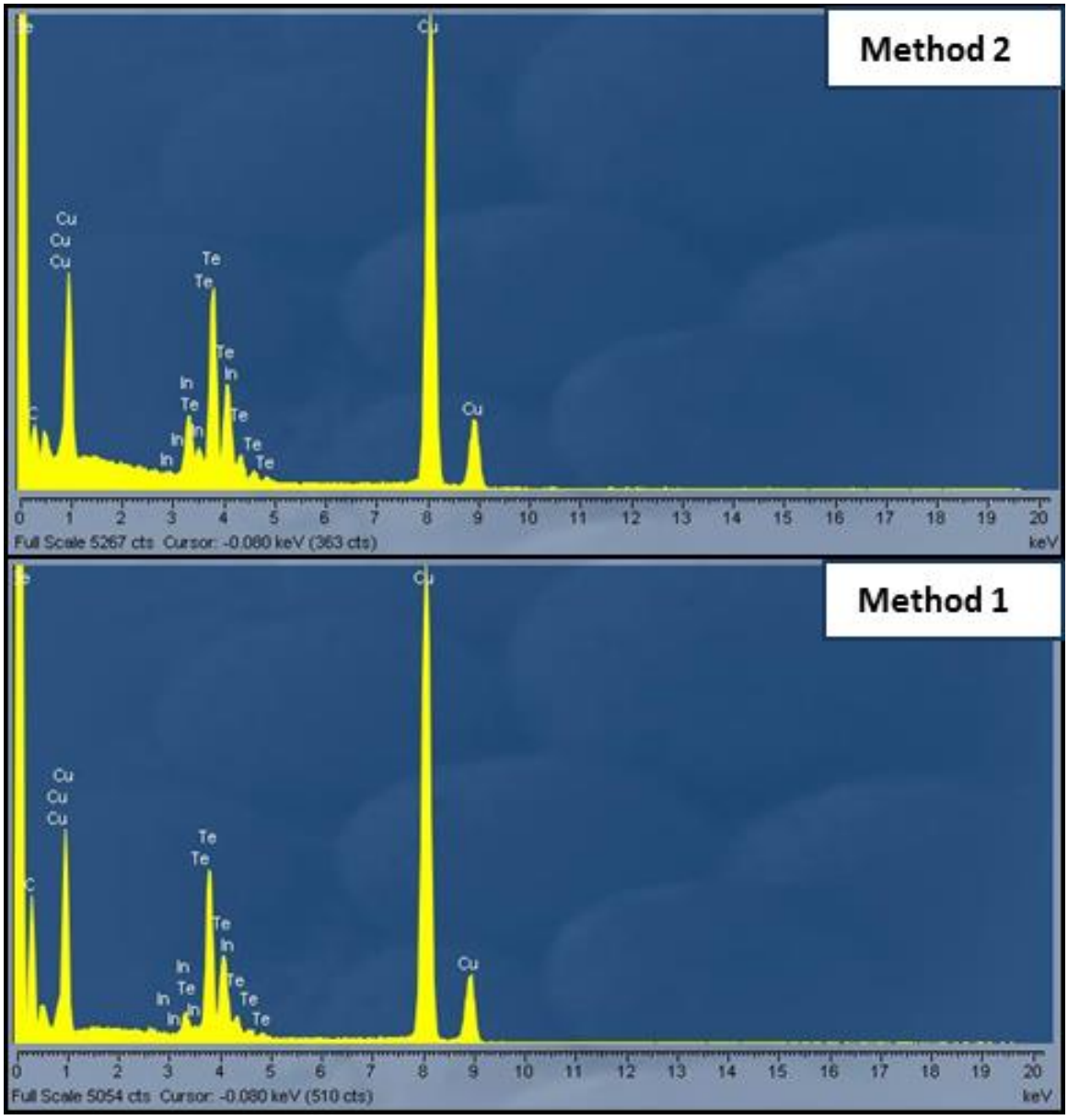


Figure 3.9: EDS spectra of TEM and HRTEM micrographs of $CuInTe_2$ crystallites synthesized at 250 °C using method 2 and method 1.

3.3 The proposed reaction path for the formation of phase pure $CuInTe_2$

In recent years it has been shown that successful synthesis of colloidal nanostructures is ligand based. [31]. The appropriate ligand environment determines the overall thermodynamic and kinetics of the reaction via coordination to metal centers [31]. Furthermore, it provides colloidal stability and structure direction by coordination to the surfaces of nanoparticles [31].

These properties have helped postulate the crystallization mechanism of ternary and quaternary selenides and sulphides in the ligand system. Kar et.al investigated formation pathway of $CuInSe_2$ nanocrystals dissolved in oleylamine [32]. Formation of the nanocrystals proceeded by initially forming binary CuSe and InSe which ultimately reacted forming $CuInSe_2$ [32]. Carenco et al. investigated the role of the binary ligand system consisting of OLA and TOP for the synthesis of Ni nanoparticles [9]. They delineated the roles of both OLA and TOP in the nucleation and growth of the nanoparticles. OLA was thought to be the reductant controlling the nucleation rate, while TOP provided a surface stabilization through coordination on the Ni(0) surface [9]. In this work, we have a binary ligand system comprised of OLA and TOP. OLA was selected as a solvent due to its strong and basic capacity and strong chelating effect [33]. The metal halides ($InCl_3$ and CuCl) were dissolved in OLA thus activating Cl^{1-}, In^{3+} and Cu^{1+} resulting from nucleophilic attack by OLA. Due to lower reduction potential of Te compared to S and Se, dissolution of Te in aliphatic solvents with considerable concentrations has not been reported [12]. Specifically, E^0 (V) of $X^0+2e^- \leftrightarrow X^{2-}$ for X = S, Se, and Te are −0.48 V,−0.92 V, and−1.14 V, respectively [12]. However, dissolution of the tellurium in phosphines could be achieved at high temperatures (~350°C) at relatively low concentrations [12]. The reaction preceded by redox transfer thus oxidizing Te to Te^{2-}. Based on the HSAB theory (Fig 3.10), we hypothesized that due to weakly polarized In^{3+} ions deemed hard acid, it will easily interact with Te^{2-} ions as a soft base. The reaction will initially proceed by converting precursor to monomers. In which the In^{3+} and Te^{2-} ions will be activated. As temperature increases, the monomer availability increases which facilitates the nucleation processes. This will permit growth of In_2Te_3 nanocrystals which has a layered structure. During this time nucleation process will be .controlled by OLA while the particle stabilization is provided by TOP. As temperature reaches 250 °C, we introduce CuCl-OLA precursor into the reaction system. Through nucleophilic attack reaction

Cu^{1+} ions will be activated. The Cu^{1+} ions will instantly react with In_2Te_3 thus forming pure chalcopyrite $CuInTe_2$ crystallites. Therefore, it is clear from the presented data the sequence in which the precursors are added is important as determined the reaction kinetics of formation of pure $CuInTe_2$ crystallites.

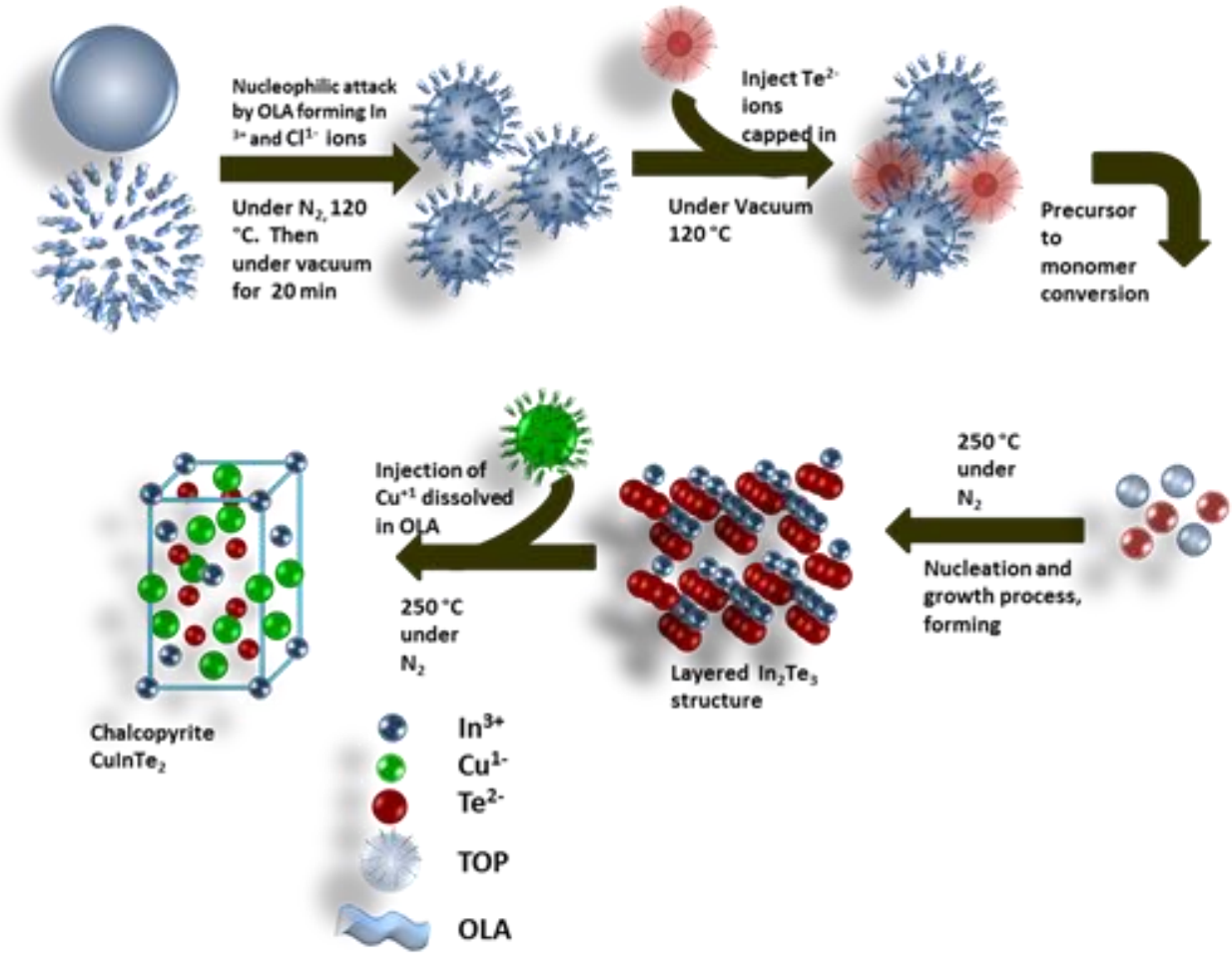


Figure 3.10: Proposed reaction path for the formation of phase pure $CuInTe_2$.

3.4 Conclusions

In this study, we have indicated that formation of ternary $CuInTe_2$ was attainable through colloidal synthesis. The high synthesis temperature of 250 °C was required for formation of $CuInTe_2$. At low temperatures 190 and 220 °C no formation of $CuInTe_2$

was observed, only Te and CuTe phases were seen. The ideal synthesis temperature for $CuInTe_2$ is 250 °C. At 250 °C, the sequence in which precursor were added was not only important for pure phase formation it also aided in postulating crystallization formation mechanism of $CuInTe_2$. Highly agglomerated cubic structures were observed for pure $CuInTe_2$, while mixed morphologies were obtained for impure crystallites. High optical band gap of 1.22 eV was obtained for pure $CuInTe_2$ crystallite which is close to that of polycrystalline thin films. Therefore, it can be said that colloidal method is an effective way of producing high quality nanocrystals applicable in photovoltaics. However, further investigations on parameters such as concentration, time and type of capping agent still need further experimentation for enhancing optical and morphological properties of this material.

3.5 References

1. E. Witt and J. Kolny-Olesiak, *Chemistry – A European Journal*, 2013, **19**, 9746-9753.

2. S. Siebentritt and U. Rau, *Wide-gap chalcopyrites*, Springer, 2006.

3. M. Green, *Solar cell efficiency tables (Version 41) Progress in Photovoltaics: Research and Applications*, 2013, **21**, 1-11.

4. L. L. Kazmerski, *Renewable and sustainable energy reviews*, 1997, **1**, 71-170.

5. I. V. Bodnar, V. S. Gurin, N. P. Soloveĭ and A. P. Molochko, *Semiconductors*, 2007, **41**, 939-945.

6. M. Boustani, K. El Assali, T. Bekkay and A. Khiara, *Solar Energy Materials and Solar Cells*, 1997, **45**, 369-376.

7. S. Roy, B. Bhattacharjee, S. N. Kundu, S. Chaudhuri and A. K. Pal, *Materials Chemistry and Physics*, 2003, **77**, 365-376.

8. M. P. Kalenga, S. Govindraju, M. Airo, M. J. Moloto, L. M. Sikhwivhilu and N. Moloto, *Journal of nanoscience and nanotechnology*, 2015, **15**, 4480-4486.

9. S. Carenco, C. Boissiere, L. Nicole, C. Sanchez, P. Le Floch and N. Mézailles, *Chemistry of Materials*, 2010, **22**, 1340-1349.

10. C. Kim, D. H. Kim, Y. S. Son, H. Kim, J. Y. Bae and Y. S. Han, *Materials Research Bulletin*, 2012, **47**, 4054-4058.

11. M. A. Malik, P. O'Brien and N. Revaprasadu, *Advanced Materials*, 1999, **11**, 1441-1444.

12. J. van Embden, A. S. Chesman and J. J. Jasieniak, *Chemistry of Materials*, 2015, **27**, 2246-2285.

13. T. Omata, K. Nose and S. Otsuka-Yao-Matsuo, *Journal of Applied Physics*, 2009, **105**, 073106.

14. R. G. Parr and R. G. Pearson, *Journal of the American Chemical Society*, 1983, **105**, 7512-7516.

15. R. G. Pearson, *Journal of the American Chemical Society*, 1963, **85**, 3533-3539.

16. M. Ananthan, B. C. Mohanty and S. Kasiviswanathan, *Semiconductor Science and Technology*, 2009, **24**, 075019.

17. F. Li and G. Yong-Quan, *Chinese Physics B*, 2014, **23**, 127801.

18. K. Neyvasagam, V. Ramakrishnan, C. Sanjeevaraja and N. Soundararajan, *Optoelectronics and Advanced MaterialsS-Rapid CommunicationsS*, 2007, **1**, 319-321.

19. H. Tanino, H. Fujikake and H. Nakanishi, *Journal of Applied Physics*, 1993, **74**, 3821-3823.

20. C. Rincón, S. M. Wasim, G. Marín, E. Hernández, J. M. Delgado and J. Galibert, *Journal of Applied Physics*, 2000, **88**, 3439-3444.

21. Q. Guo, S. J. Kim, M. Kar, W. N. Shafarman, R. W. Birkmire, E. A. Stach, R. Agrawal and H. W. Hillhouse, *Nano letters*, 2008, **8**, 2982-2987.

22. M. R. Ananthan and S. Kasiviswanathan, *Solar Energy Materials and Solar Cells*, 2009, **93**, 188-192.

23. T. Mise and T. Nakada, *Thin Solid Films*, 2010, **518**, 5604-5609.

24. A. Miller, A. MacKinnon and D. Weaire, in *Solid State Physics*, eds. F. S. Henry Ehrenreich and T. David, Academic Press, 1982, vol. Volume 36, pp. 119-175.

25. H. Neumann, *Helv. Phys. Acta*, 1985, **58**, 337-346.

26. P. Prabukanthan and R. Dhanasekaran, *Materials Research Bulletin*, **43**, 1996-2004.

27. C. Kim, D. H. Kim, Y. S. Son, H. Kim, J. Y. Bae and Y. S. Han, *Materials Research Bulletin*, 2012, **47**, 4054-4058.

28. W. Hörig, H. Neumann, V. Savelev, J. Lagzdonis, B. Schumann and G. Kühn, *Crystal Research and Technology*, 1989, **24**, 823-827.

29. D. Sridevi and K. V. Reddy, *Thin Solid Films*, 1986, **141**, 157-164.

30. S. M. Wasim, A. LaCruz Vielma and C. Rincón, *Solid State Communications*, 1984, **51**, 935-937.

31. N. Ortiz and S. E. Skrabalak, *Langmuir*, 2014, **30**, 6649-6659.

32. M. Kar, R. Agrawal and H. W. Hillhouse, *Journal of the American Chemical Society*, 2011, **133**, 17239-17247.

33. J. Zhou, G.-Q. Bian, Y. Zhang, Q.-Y. Zhu, C.-Y. Li and J. Dai, *Inorganic chemistry*, 2007, **46**, 6347-6352.

Chapter 4: Morphology and shape engineering of $CuInTe_2$ nanostructured semiconductor material

4.1 Introduction

Colloidal processing of semiconductor nanocrystals has enabled fabrication of various particles with novel physical and chemical properties [1]. The new emerging physical and chemical properties are not only related to crystal sizes and surface chemistry, but also associated with the shapes of particles [2]. The size and shape dependent properties exhibit the quantum confinement effect which allows for band gap engineering and fine-tuning of the optical and electrical properties of the nanocrystals [3]. Based on these properties, colloidal semiconductor nanocrystals are beneficial to solar cells [4]. Their unique energy band gap and other advantages such as high absorption coefficient, high radiation stability, or exceptional radiation hardness and defect tolerance are pertinent characteristics that make them potential candidates for absorber-based solar cells [4]. Among the various colloidal semiconductor nanocrystals, Cu-based ternaries of the selenides and sulphides are well studied [5]. Solar-energy conversion efficiencies of about 20% and 12% have already been reported for $CuInSe_2$ and $CuInS_2$ respectively [6].

The engineering of properties afforded by the colloidal method has made it possible to obtain high quality semiconductor nanocrystal of various shapes and sizes [2]. Although it is an excellent attribute of this method, it is challenging to achieve highly monodispersed semiconductor nanocrystals [2]. In the colloidal method, the growth process of the particles is based on the Lamer model as shown in Fig. 4.1 [7]. The formation of nanocrystals is governed by rapid and homogeneous mixing of reagents at high temperatures where they turn

into monomers [8]. As the concentration of the monomers reaches super saturated level, nuclei are formed. This allows for controlled nucleation of the nanocrystals [8]. When the injection volume increases, the process becomes slower and less predictable and the intrinsic of mixing time is reached [8].

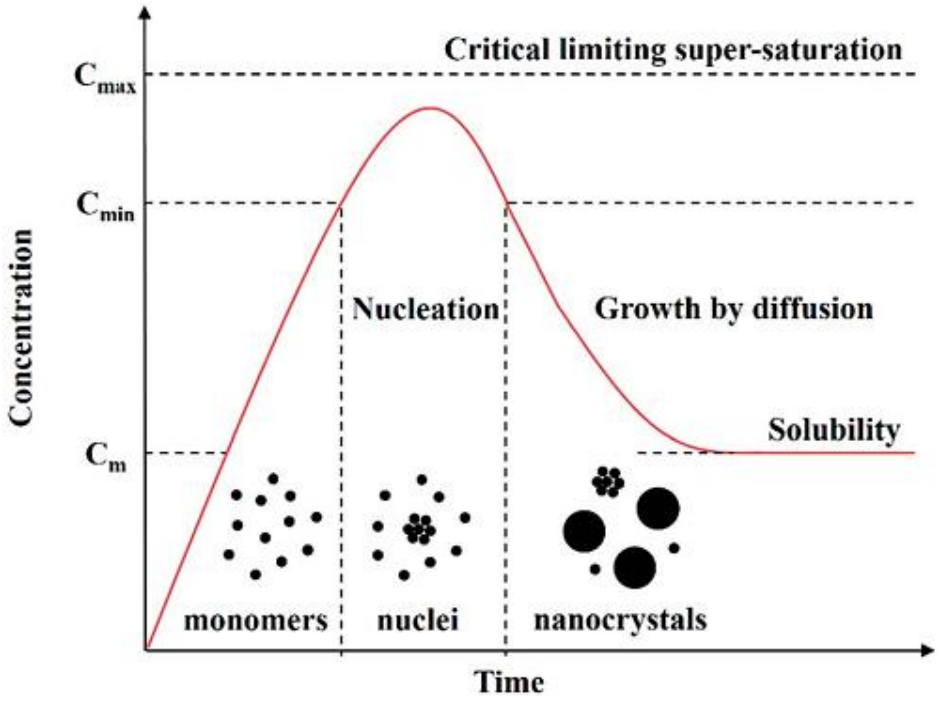


Figure 4.1: Schematic illustration of the nucleation and growth process of nanocrystals in solution: precursors are initially dissolved in solvents to form monomers, followed by the generation of nuclei and the growth of nanocrystals via the aggregation of nuclei [2].

In most cases, the temperature drop following the injection is essential as it limits nucleation to a short burst-like event and subsequently slows down the growth of the nanocrystal [8]. Prior to the crystal growth stage, the nucleation process proceeds until the temperature and monomer concentration has dropped below the critical threshold then growth begins at low temperatures [8]. It should be noted that the nucleation and growth steps are vital for the formation of monodispersed metal chalcogenides nanocrystals [9]. As crystal growth continues, occasionally there are nuclei formed which often result into wide size distribution

of the nanocrystals [10]. This is due to a poor nucleation rate, triggered by poor temperature control [10]. The nucleation rate is mostly sensitive to changes in temperature compared to the growth rate due to the high activation energy required [11]. Therefore to balance the nucleation and growth rate the reaction temperatures should be varied. [11].

Previously, the nucleation and growth of nanoparticles over extended reaction times have been investigated. It was found that when the temperature was kept moderate, particles with a wide range of sizes were obtained [12]. Peng and colleagues studied the growth process of CdSe and InAs nanocrystals [12]. They established that there was temporal size evolution as the reaction time increased [12]. The size evolution was distinguished by two distinct kinetic regimes in which particle size rapidly increased followed by a focused size distribution [12]. The wide size distribution was due to the high monomer concentration which resulted in size focusing of particles. As monomer concentration decreases particles grow slowly resulting in the shrinking of smaller particles with size distribution being broaden. This is known as defocusing of the particle size [2]. The focusing and defocusing process of size distribution are illustrated in Fig. 4.2b.

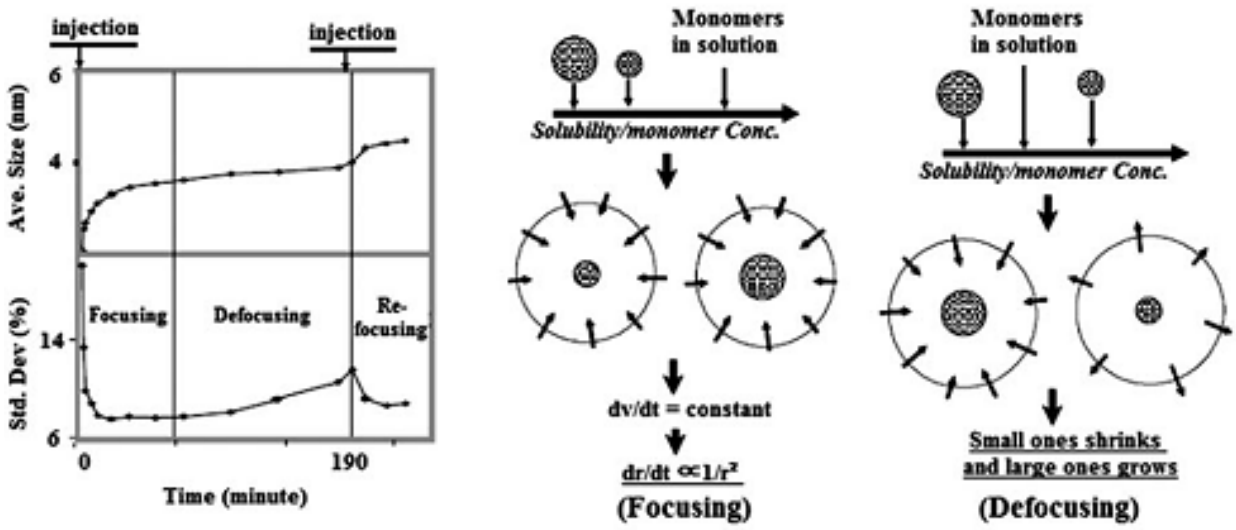


Figure 4.2: (a) Temporal evolution of the size distribution of CdSe NCs prepared by a hot injection method, including a secondary injection during the reaction. (b) Illustration of the focusing and defocusing of size distribution observed in (a) (reproduced with permission from ref. 52, copyright 1998, American Chemical Society, and ref. 53, copyright 2005, Springer) [2].

According to the study on size distribution control of colloidal nanocrystals, the growth stage may occur in two possible ways [2]. It may occur either by diffusion controlled growth or reaction controlled growth. In the diffusion controlled growth the reaction takes place rapidly in that the crystal growth rate is controlled by monomer diffusion through the reaction medium [13]. In the reaction controlled growth, the particle growth rate is governed by the surface reaction of monomers [2]. The growth rate of nanocrystals is determined by the relative rate of nucleation and the growth rate of monomers on particle surfaces [2]. Therefore, particle growth rate is directly proportional to the surface area of the individual particle, and the size distribution will widen as particles continues to grow [2]. Although the emphasis on particle size evolution is due to the change in reaction times, temperature can still affect the particle size of the nanocrystal as it plays a paramount role in determining the

nucleation rate. It has also been reported that particle sizes of the nanocrystals will increase with an increase in temperature due to Ostwald ripening [8].

While size evolution of the nanocrystals is dependent on the reaction time, morphology and shape control is governed by growth regime of the reaction [14]. The reaction can either progress in a kinetic or thermodynamic growth regime [15]. The growth regime is influenced by factors such as monomer concentration, reaction temperature, functional group of the capping agent [15]. The thermodynamic growth regime is facilitated by thermal energy (high reaction temperature) and low monomer concentration, while kinetic regime is achievable at low reaction temperatures with high monomer concentration [15]. The thermodynamic growth regime result in formation of isotropic-shaped nanocrystals (e.g. dots and cubes) and the selective anisotropic structures (e.g. rods and tetrapods) are obtained by the kinetic growth regime [15-16].

The formation of shape is determined by the capping agent chemisorbed on the surface [17]. That is the direction of growth will be hindered in a chemisorbed face [17]. For example in a kinetic growth regime, shape control can be achieved by increasing the growth rate which in turn can make high energy facets grow faster than low energy facets (Fig. 3a). Kinetic shape control can also be obtained by introducing molecules with preferred adhesion therefore resulting in formation of rod or disk-shaped nanocrystals (Fig. 4.3b) [1].

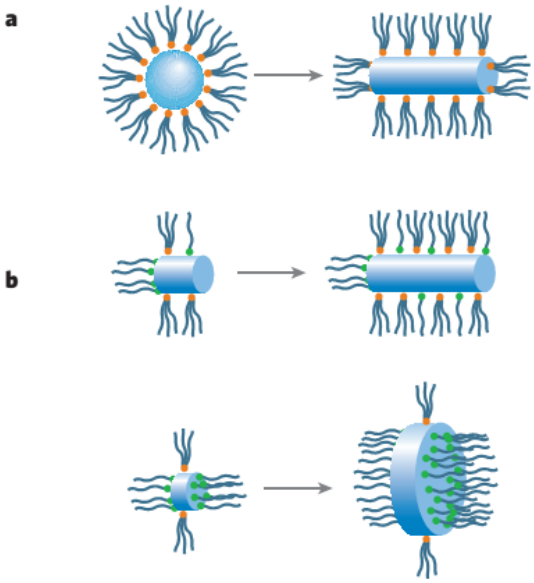


Figure 4.3: shape control of colloidal nanocrystals a) Kinetic shape control at high growth rate. The high-energy facets grow more quickly than low energy facets in a kinetic regime. b) Kinetic shape control through selective adhesion [1].

As seen in the previous chapter there was a lack of morphology control on $CuInTe_2$ particles, as the particles obtained were either agglomerated or heterogeneous. In this chapter we investigate the influence of capping agent on morphology and optical properties of the $CuInTe_2$. We will further investigate the effect of reaction time on the morphology and optical properties of particles capped with various capping agents.

4.2 Experimental section

4.2.1 Materials and reagents

Copper (I) chloride (CuCl), indium (III) chloride ($InCl_3$) and elemental tellurium (Te) were all purchased from Sigma Aldrich. Tricoctylphosphine (TOP), oleylamine (OLA), hexadecylamine (HDA), ethanedithiol (EDT), dichloromethane (CH_2Cl_2), chloroform

($CHCl_3$), methanol (CH_3OH) and ethanol (C_2H_6O) were all purchased from Sigma Aldrich and used without further purification.

4.2.2 Synthesis of $CuInTe_2$

Two methods were employed for the synthesis of $CuInTe_2$. In method 1, 2.5 mmol of copper chloride and 2.5 mmol of indium chloride were added to 7 mL of OLA and heated to 120 °C under nitrogen. The mixture was then left under vacuum for 20 min before 2 mL of TOPTe (1 M) was injected. The solution was then further heated to 190 °C for 30 min. The temperature was then decreased to 60 °C. Methanol was added to the solution to flocculate the particles. The particles were then collected through centrifugation at 3000 rpm and washed with dichloromethane, ethanol, and methanol to remove the impurities. The temperature was varied from 190 °C – 250 °C. Thereafter, reaction time studies were conducted under temperatures 190 °C – 250 °C. The use of various capping agents was also explored at temperature 250 °C. Method 2 described in chapter 3 was adopted to synthesize particles capped with OLA.

4.2.3 Characterization

XRD patterns on powdered samples were measured on a Bruker MeasSrv D2-205530 diffractometer using secondary graphite monochromated CoKα radiation (λ 1.78897 Å) at 30 kV/30 mA. Measurements were taken using a glancing angle of incidence detector at an angle of 2°, for 2θ values over 20 - 90° in steps of 0.026° with a step time of 37 s and at a temperature of 25 °C. Raman spectroscopy in which the 514 nm emission line from an argon laser done in conjunction with a Horiba Jobin-Yvon LabRAM HR Raman spectrometer was used. The transmission electron microscopy (TEM) was carried out on a FEI Technai T12 TEM microscope with an EDS detector operated at an acceleration voltage of 200 kV with a

beam spot size of 20 - 100 nm in TEM mode. UV-vis to near-Infra Red spectral frequencies were acquired using a 40X UVB microscope objective lens from Thor Labs following electromagnetic excitation using a 244 nm UV probe.

4.3 Results and discussions

4 3.1 Effect of coordinating ligands on morphology

Although shape controlled nanocrystals can be obtained, it is however desirable to develop synthetic strategies that allow manipulation of various shaped particles. The intrinsic geometry of colloidal nanocrystals has significant effect on their electric, magnetic, catalytic and electrical properties which are especially important for their stimulating applications. In colloidal method, shape control is governed by the use of coordinating ligands which adsorbs on the surface of the molecules during the reaction. The dynamic behaviour of these surfactants greatly influences the growing crystal faces. This is due to the ability of the capping agents of preferentially binding to different types of facets on a nanocrystal, which changes the specific free energy and thus their proportions in terms of area [18]. In other words the facet in which the capping agent is chemisorbed will prevent atom deposition on that facet thus nanocrystals with a distinct shape will eventually grow [18]. However, preferential binding is dependent on factors such as crystal structure and the functional group(s) of a capping agent as well as the electronic and surface structure of the metal [18]. Moreover, the intrinsic anisotropic property in atomic arrangement of different crystallographic planes also plays a key role in determining the morphology of the nanocrystals [18]. The surface energy is indirectly controlled by adjusting the types and ratios of the organic molecules. The different binding crystallographic faces introduced by a mixture of surfactants allow control over shape of the nanocrystals. Furthermore, the coordinating ligands allow control over morphology tailoring, facilitates assembly into

artificial molecules or patterns, and induces interactions such as exciton coupling, energy or electron transfer between the core and the surface ligands of a nanocrystal [19].

The effect of coordinating ligands on particle morphology was employed by carrying a synthesis at 250 °C using various capping agents namely: oleylamine (OLA), hexadecylamine (HDA), trioctylphosphine (TOP) and ethanedithiol (EDT). The capping agents are shown in scheme 1. The synthesis duration of the nanoparticles was kept at 60 min.

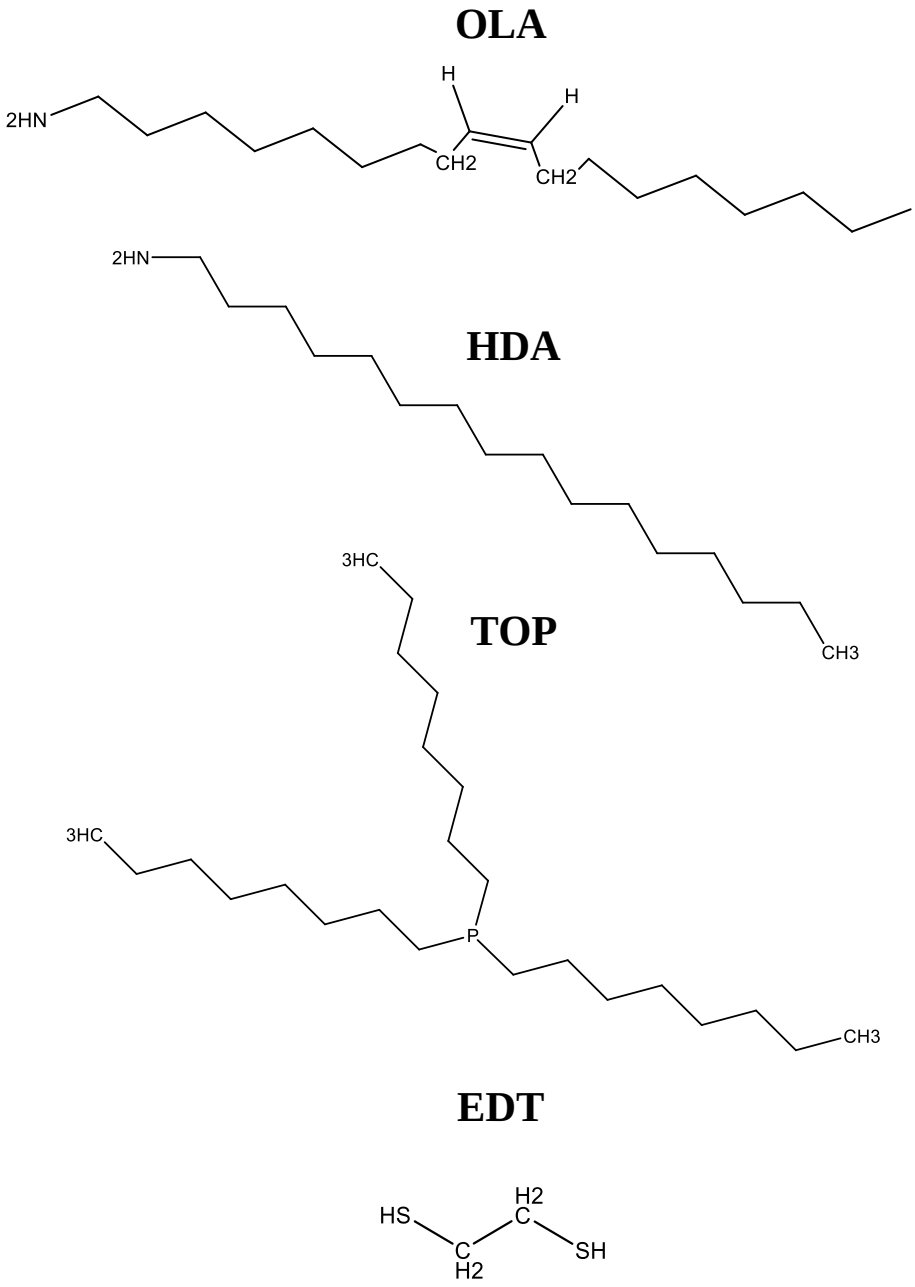


Figure 4.4 Scheme of the different capping agent molecules and their functionalities.

The morphology of the particles was further investigated by TEM. The TEM micrographs are shown in Fig. 4.5 below. The use of various capping agents gave rise to particles with different morphologies. The long chain alkyl amines gave rise to 1D hollow rod for HDA and 3D cubed shaped particles for OLA. The formation of anisotropic rods is consistent with other reports in the literature [[20]]. The formation of rods is said to be encouraged by the high-

energy twin plane surfaces exposed at the end vertices of the decahedron, facilitating fast metal reduction with a preferential growth direction [21]. This mechanism has been observed for different colloidal systems and capping agents [20]. The irregular and hollow shaped particles formed, could be indicative of rod shaped particles formed from spherical nucleating centres, which eventually fused to form a long rod shape. This is contrary to formation of CdSe quantum rods which were synthesized from the seeded growth approach [22]. The hollow rods seem to be inconsistent in length with both long and short rods observed which could be attributed to the fusion rate or growth rate. Previously, it has been reported that it is challenging to achieve control over rod length particularly for long rods [23]. It is believed that there are factors such as pH, nature of seed, heat treatment etc. which need to be taken into account in order to understand the formation mechanism of nanorods [23]. However, in both cases the particles were not homogeneously dispersed.

There are round shaped particles observed alongside the different sized cubes for OLA capped particles while irregular shaped particles close to the stacked hollow rods are seen for HDA capped particles. The formation of aggregates in both cases can be attributed to the dynamic binding and unbinding process between the particles surface and the electron donating group which is amine in this case. This is most likely brought about by either the excessive washing of the particles or by another incoming ligand [24- 25]. The conical shaped particles were seen for TOP capped particles. The conical particles are said to evolve from penta-twinned decahedral particles [26]. Their growth direction is along the (110) which lead to formation of branches [26]. Due to the unequal corners of the penta-twinned decahedral particles, each corner will experience a different growth rate [26]. This will lead to the formation of different branch lengths as seen in the present case.

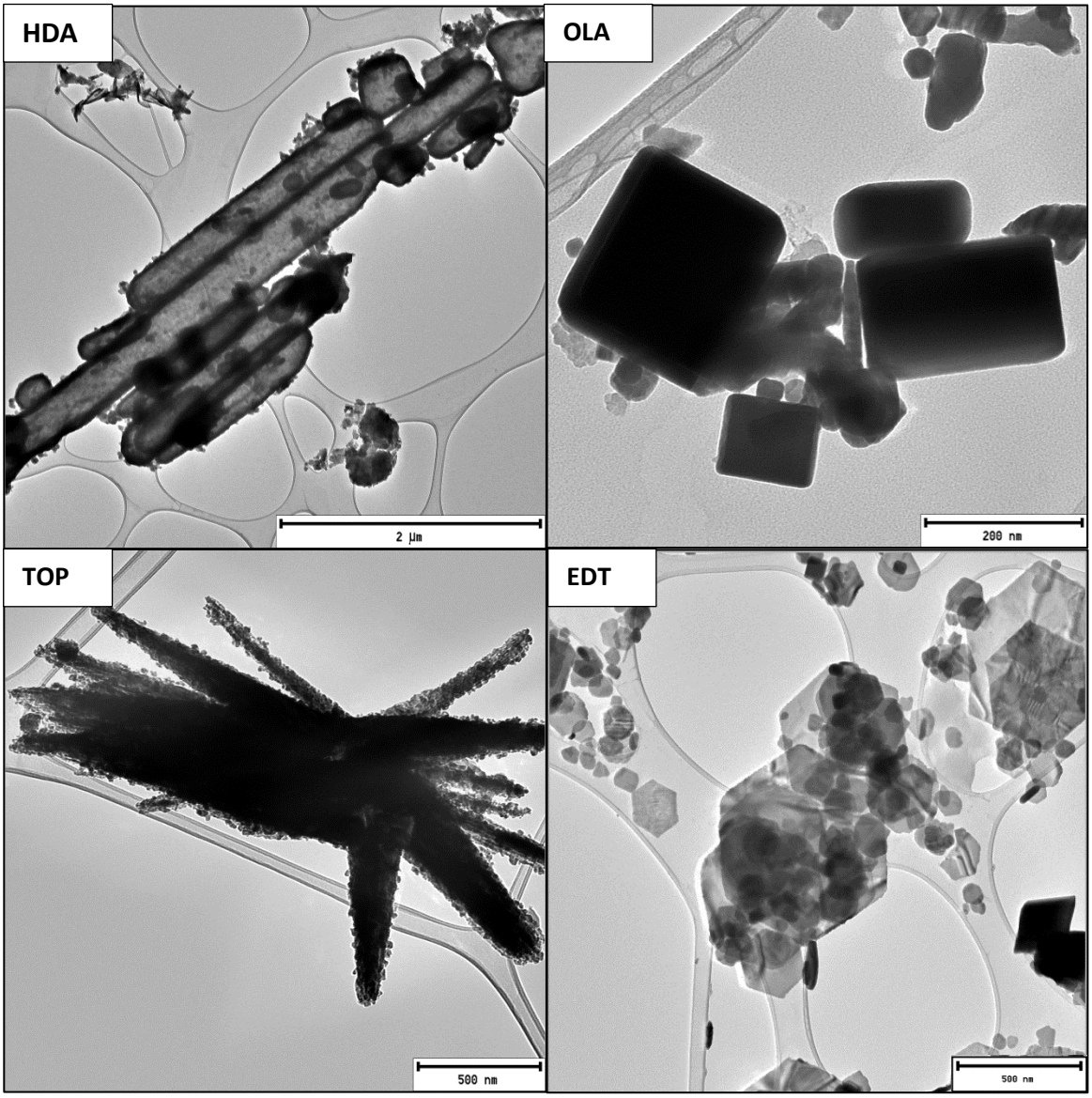


Figure 4.5: TEM micrographs of $CuInTe_2$ synthesized at 250 °C using various capping agents.

The nanosheets are observed for EDT capped particles. Three types of nanosheets morphologies are noticeable, that is, triangular, hexagonal, and quasi-equilateral hexagonal. The observed triangular morphologies follow that of Djurleite $Cu_{31}S_{16}$ [27]. It was deduced that triangular nanosheets grow along lateral direction and are formed first [27]. Due to the high energy of the three sharp angles, they continue to grow into more stable shapes [27].

They further demonstrate that both the triangular and hexagonal particles are symmetrical with the [100] facets being perpendicular to the normal direction [27].

The crystal structure of the nanocrystals was analysed by XRD. The diffraction patterns are illustrated in Fig. 4.6. From the diffraction pattern major peaks indexed as (111), (220), (331), (222) and (420) according to PDF#:01-0703086 were detected. There is a decrease in peak intensity across all the capping agents except for OLA capped particles which have highest peak intensities. Furthermore, there is a peak shift to low and high 2θ angles for HDA and EDT capped particles respectively. The formation of binary impurities was detected in all capping agents except for OLA which showed pure $CuInTe_2$ phase. The change in peak intensity and peak position can be attributed to an increase in vacancy concentration defects. Previously, it was reported that the presence of stacking faults defects in nanocrystals resulted in peak position shift [28]. Moreover, the change in stoichiometric composition in CuIn, results in a change in lattice parameters which can cause peaks to shift [28]. Furthermore, peak shifting can be attributed to the coordination provided by the capping agent. For example, OLA and HDA are both long chain alkyl amines, and they can act as electron donors at elevated temperatures [18]. They exhibit similar basicity and affinity to the metals through their NH_2 functional groups [18]. Though they seem to have similar properties, we observed shifting of the peaks to low 2θ angles and formation of binary impurities for HDA capped particles. This can be due to the lack of C=C bond in HDA, thus resulting in limited coordination. The binary impurities formed in HDA capped particles could be attributed to the difference in reactivity and stability of the coordinating ligand at 250 °C.

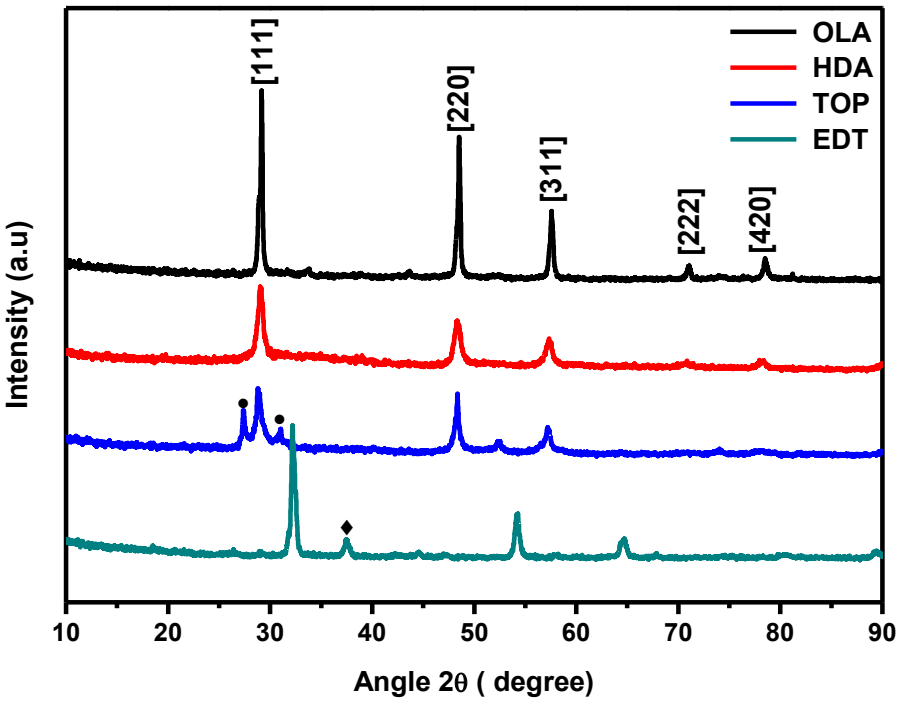


Figure 4.6: XRD patterns of $CuInTe_2$ synthesized at 250 °C using various capping agents♦ = Te phase and ● = Cu_5Te_3.

Thereby suggesting that both coordinating alkyl amine solvents form intermediate complexes with different reactivity which tends to decompose and form different phases. In other words, those intermediate complexes possess different reactivity to form $CuInTe_2$ nanoparticles. Similarly, the formation of CdS nanocrystals at elevated temperatures in ethylenediamine (EDA) and diethylamine (DEA) was reported to form through different intermediate complexes [18]. This was attributed to stability constant of the complex formed in EDA which was higher than the one formed in DEA [18]. Therefore suggesting that the complex with high reactivity is EDA and is likely to decompose into the thermodynamically favoured phase compared to the DEA complex [18].

As seen from the TEM images anisotropic colloidal nanocrystals were obtained with different coordinating agents. Anisometry in morphology is based on the growth confinement of

nanocrystals in a particular direction. Depending on the dimension of the nanocrystals for example OD, 1D, 2D or 3D, electron confinement will differ thus making the optical properties of the nanocrystal shape-dependent. In an instance where the synthesized nanocrystal diameter approaches exciton Bohr diameter the optical properties becomes both size and shape dependent. Furthermore formation of geometric shapes affects the arrangement of the atoms in a crystal structure resulting in compression or expansion.

Typically, the $CuInTe_2$ ternary semiconductor has a chalcopyrite structure. The energy band structure of the chalcopyrite is derived from their binary analogues. The ordering of the valence band has been established by using selection rules governing the transition from five Cu d-band in the $CuInSe_2$ [29]. It has been suggested that the lower valence structure for $CuInTe_2$ is based upon ordering of five transitions [29], in which the chalcopyrite tetragonal field splits the free atom d level into Γ_3 and Γ_5. The Γ_3 level further splits into Γ_3 and Γ_1, while Γ_5 splits into Γ_5 and Γ_4 [29]. The spin-orbit interaction further produces the last five levels seen in Fig. 4.7. This energy is due to the transition from Γ_6 or Γ_7 in the valence band to the Γ_6 level in the conduction band as shown in Fig. 4.7 [30].

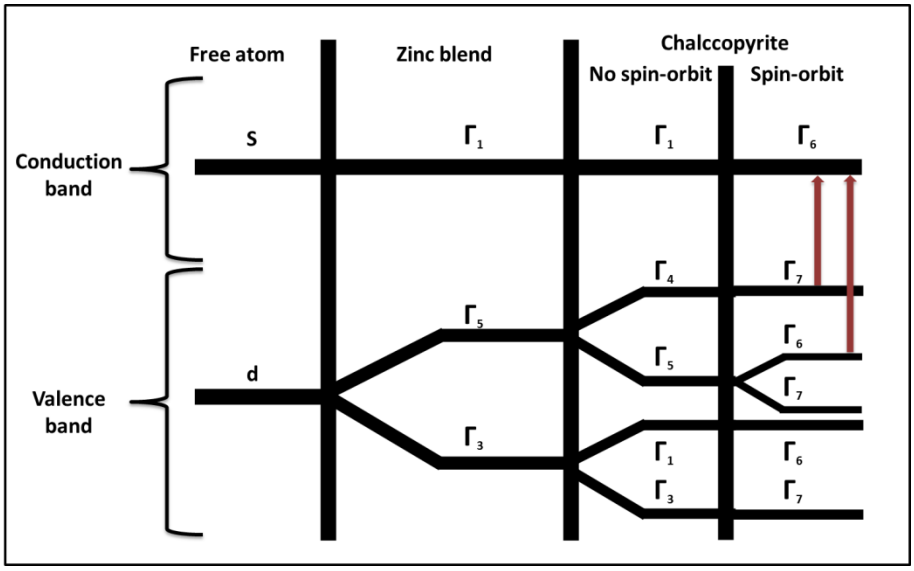


Figure 4.7: Schematic diagram of the band structure of chalcopyrite with modified d-levels to fit the ordering levels in $CuInTe_2$ [29].

Due to the fundamental importance of shape-dependent optical properties of colloidal nanocrystals, optical measurements were conducted. The absorption measurements of powdered nanocrystals are illustrated in Fig. 4.8 below. The optical band gap of the nanocrystals was obtained by Kubelka-Munk function [31]. In which absorption was converted to reflectance using equation:

$$\boldsymbol{A = Log\ \frac{1}{R}} \qquad (4.1)$$

Where A is absorbance and R is reflectance. Hence R becomes:

$$\boldsymbol{R = \frac{1}{10^{A}}} \qquad (4.2)$$

Thereafter Kubelka-Munk function, *F(R)*, which allows the optical absorbance of a sample to be approximated from its reflectance was applied [32].

$$\boldsymbol{F(R) = \frac{(1-R)^2}{2R}} \qquad (4.3)$$

The absorption spectra of the particles capped with various capping agents exhibit band edges in the near infrared region. The band edges are similar with a slight shift observed between

the capping agents. The shift in band edges can be attributed to formation of different geometric shapes of the nanocrystals [33]. The band gap of elongated particles is dependent on both their width and length although it is more sensitive to the width [34]. The measured band edges of the amine ligands are 1013 nm and 1017 nm for OLA and HDA respectively. The corresponding optical band gaps are 1.22 eV and 1.21 eV for OLA and HDA respectively.

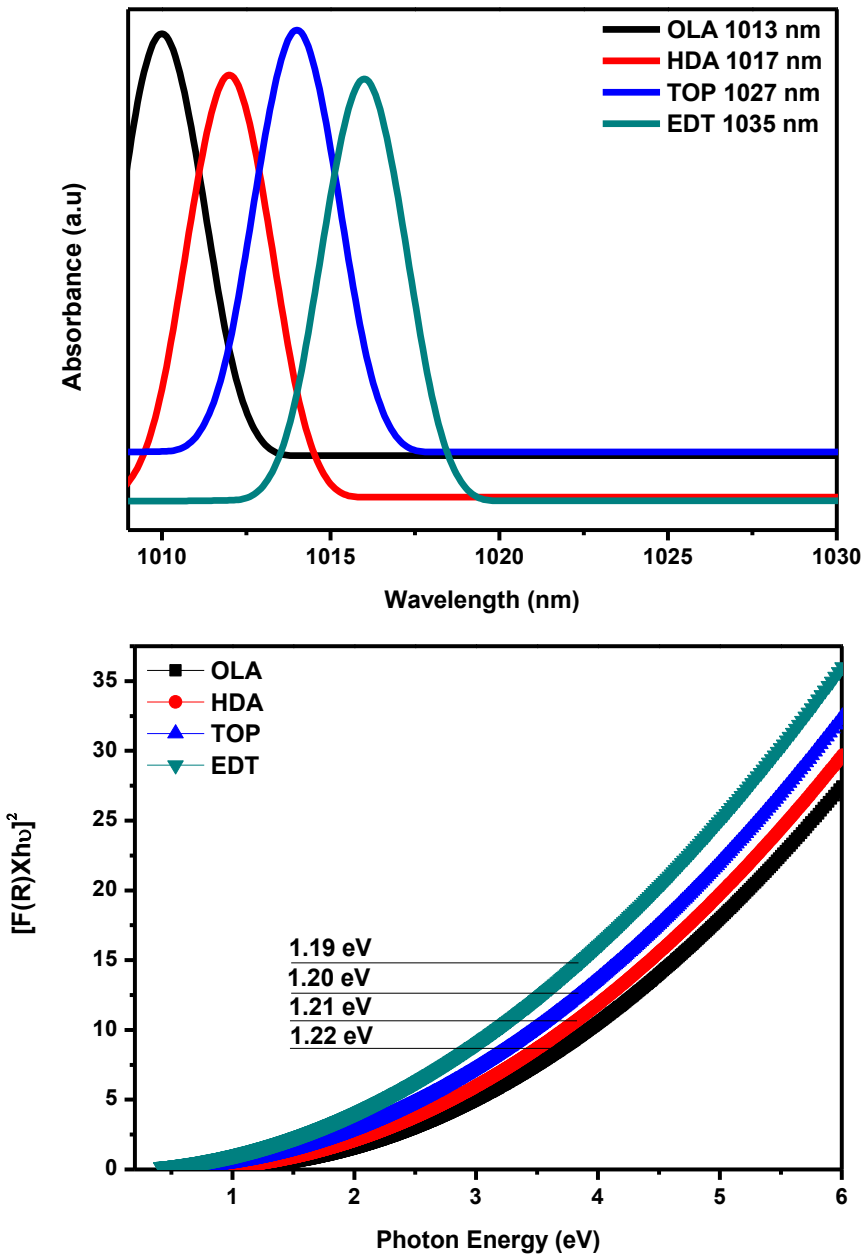


Figure 4.8: UV–Vis–NIR absorbance spectrum (top) and optical band gap (bottom) of $CuInTe_2$ crystallites synthesized at 250 °C using various capping agents.

The observed optical band gaps are due to the direct allowed transitions. The observed transitions can be due to the shallow level acceptors. Although the shallow level acceptors have been identified before, there is still controversy around the origin of these defects [35]. In some reports it is stated that they originate from the Cu vacancy while others claim that they

in fact originate from the Te vacancy [35]. It is therefore highly recommended that defect studies on these materials are undertaken in future.

Upon changing from the amine ligands, the absorption band edges changed to 1027 nm and 1035 nm for TOP and EDT respectively. This resulted in a slight decrease in the optical band gaps to 1.20 eV and 1.19 eV for TOP and EDT respectively. Band gap narrowing in $CuInSe_2$ has been attributed to ionization impurity induced screening [36], resulting from the quantum mechanical penetration of the band state in the band gap [37]. The quantum mechanical penetration is said to originate from potential gradient of the charged defects [38]. It has also been reported that the band gap of p-type $CuInTe_2$ is usually low compared to the n-type due to the existence defect levels in different charge [39]. The optical results are summarized in Table 4.1.

Table 4.1: Optical properties of $CuInTe_2$ capped with different surfactants

Ligand	**Morphology**	**Absorption Band edge (nm)**	**Optical band gap (eV)**
HDA	Hollow rods	1017	1.21
OLA	Cubes	1013	1.22
TOP	Tree-branched	1035	1.20
EDT	Hexagonal ultrathin sheets	1027	1.19

4 3.2 Effect of reaction time on morphology

It is understood that coordinating ligands govern shape control of colloidal nanocrystals. The shape evolution mechanism can be established through coordinating ligand chemistry and it determines how monomers and growth of particles evolve over time [19]. It therefore controls the thermodynamic and kinetic stability of the metal complexes [19]. The thermodynamic stability is controlled via chelate or macrocyclic effect [19]. The kinetics of the reaction are modified by displacing the native ligands of the metal complex by either the precursor reduction or decomposition [19]. By understanding all of these key factors, one can be able to establish what facilitates certain growth and shapes. Moreover, one can determine what facilitates assembly into artificial molecules or patterns, and induces interactions such as exciton coupling, energy or electron transfer between the core and the surface ligands of a nanocrystals [19].

Understanding morphology evolution will help understand the novel electronic, magnetic, catalytic and optical properties of the colloidal nanocrystals that also evolve over time [14]. This will further aid in design and development of energy devices where these materials are applicable. For example the two-dimensional (2D) nanomaterials such as nanosheets and nanoplates have been reported to be superior over spherical nanocrystals for constructing nanodevices owing to their anisotropic structures [40]. Additionally, it also helps to develop enhanced colloidal reaction systems and effectively engineer properties as reproducibility of colloidal systems is challenging. In the present case morphology evolution of $CuInTe_2$ nanocrystals, was studied by extracting aliquots at various reaction times when particles were grown at 250 °C. Herein, we specifically study the evolution of ultra-thin sheets which form when the particles are capped with EDT.

It is known that the high-energy facet grows much faster than the low-energy facet and the fast growing facets eventually disappears, leading to the development of a crystal terminated with low-energy facets. The mixture of rods, cubes and amorphous particles seating on irregular shaped plates were observed under TEM for an aliquot of the reaction taken at 5 min as shown in Fig. 4.9. The Formation of the undefined particles is indicative of the lack of temperature control leading to rapid particle growth. Temperature drop is usually evident upon injection, and this may affect homogeneous nucleation and growth of the particles.

As the reaction time is further increased to 15 min, the irregular shaped plates begin to self-assemble into anisotropic elongated rod-like shaped structures. The 1D nanorods are comprised of the irregular shaped plates. In other studies it has been reported that the formation of cylindrical wurtzite CdSe nanocrystals was due to the difference in surface energies connecting facets which are related to their intrinsic properties [15]. They indicated that the side facets of the cylindrical structures where passivated by surfactant and their surface energy was low compared to the side facets [15]. Therefore, growth was favored on the side facets, resulting in formation of elongated rods. Formation of self-assembled nanorods can be attributed to lack of passivation on the end facets resulting into high surface energy, thereby favoring growth in that direction.

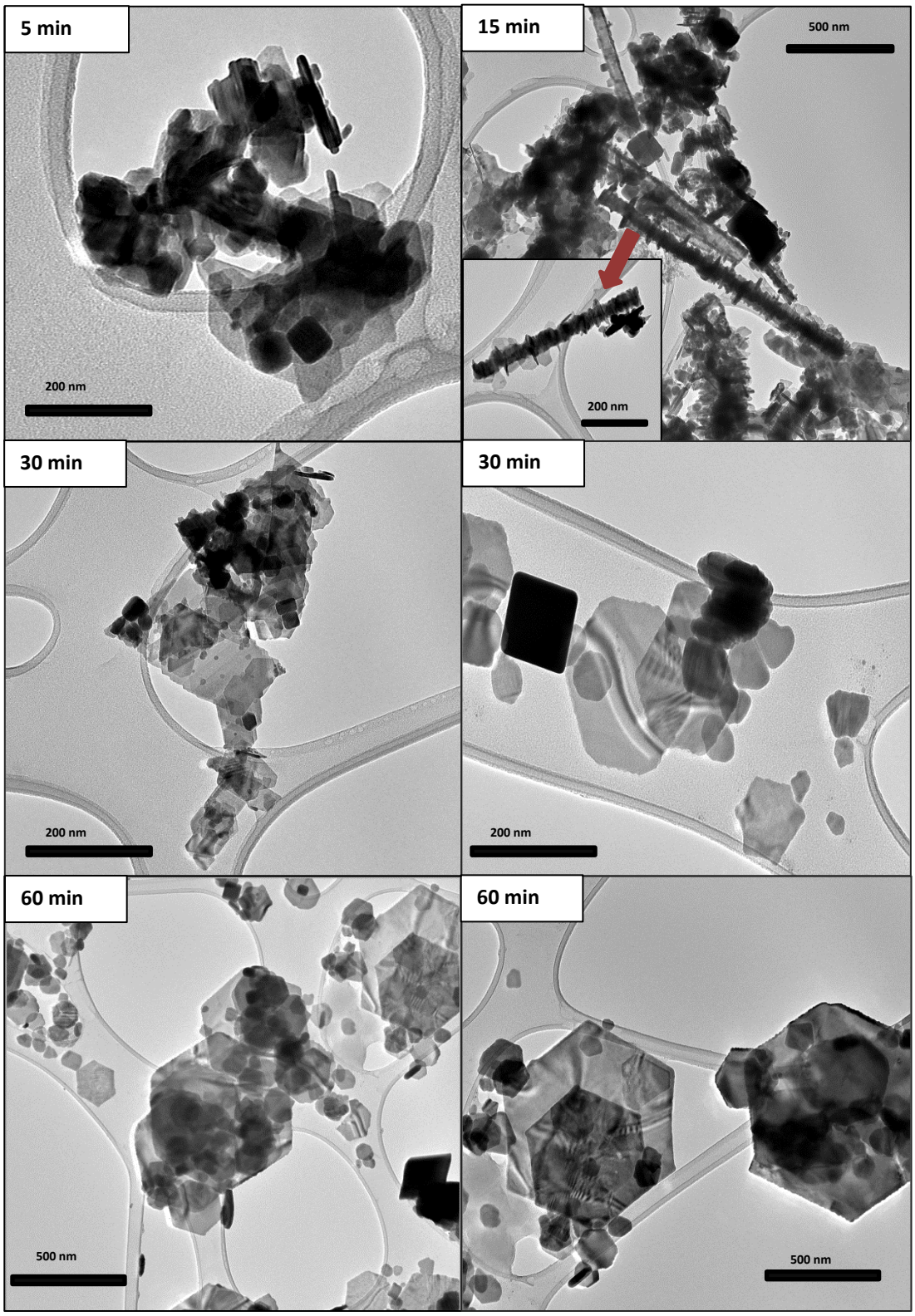


Figure 4.9: Morphology transition from 1D to 2D Shape of $CuInTe_2$ with increasing reaction time.

At 30 min, cylindrical structures collapsed into different shaped sheets and traces of cubed and irregular shaped particles are evident. The formation of nanosheets from nanorods is contrary to the observations of Yi and colleagues who reported transformation of the $Cu_{13}S_{16}$ 2D nanosheets to 1D nanorods [27]. However, in their case, the formation of 1D nanorods was induced by face-to-face stacking, which resulted into self-assembled nanorods [27]. It was further indicated that dipole-dipole interaction along the [100] direction and the hydrophobic interaction between the nanoplates were the main driving force for the formation of 1D superstructures of the nanoplates [27]. Nevertheless, based on the obtained results herein, it is evident that nanosheets are more dominant. However, it is not clear between the triangular and hexagonal sheets which shape is formed first.

Upon increasing reaction time to 60 min, large hexagonal and quasi-triangular nanosheets are observed with hexagonal nanosheets being more dominant. With hexagonal nanosheets being more dominant it is not clear whether they are formed through direct transformation of triangular nanosheets or through transition of triangular to quasi-triangular eventually forming hexagonal nanosheets. Therefore in this case it is difficult to establish the growth direction. Yi and co-workers observed a mixture of regular defined shaped nanosheets [27]. They first attributed formation of regular shapes to controlled thermodynamic conditions [27]. Similarly, they also detected triangular, quasi-triangular and hexagonal nanosheets. They deduced that the morphology evolution of the nanosheets was through the initial growth of the triangular nanosheets [27]. This is followed by transformation to quasi-triangular shapes, as result of high energy, three sharp angle tips gradually growing into bigger particles, which eventually form stable hexagons [27]. Herein, the evolution of nanosheets is similar to that of Yi and co-workers. From the TEM micrographs, the formed nanosheets appear to be crystalline with lattice fringes being observed (Fig. 4.10). The measured lattice spacing for

the triangular, quasi-triangular and hexagonal sheets were all 0.315 nm corresponding to [111] peak. This confirms that as morphology evolved from triangular to the hexagonal sheets, no phase evolution took place.

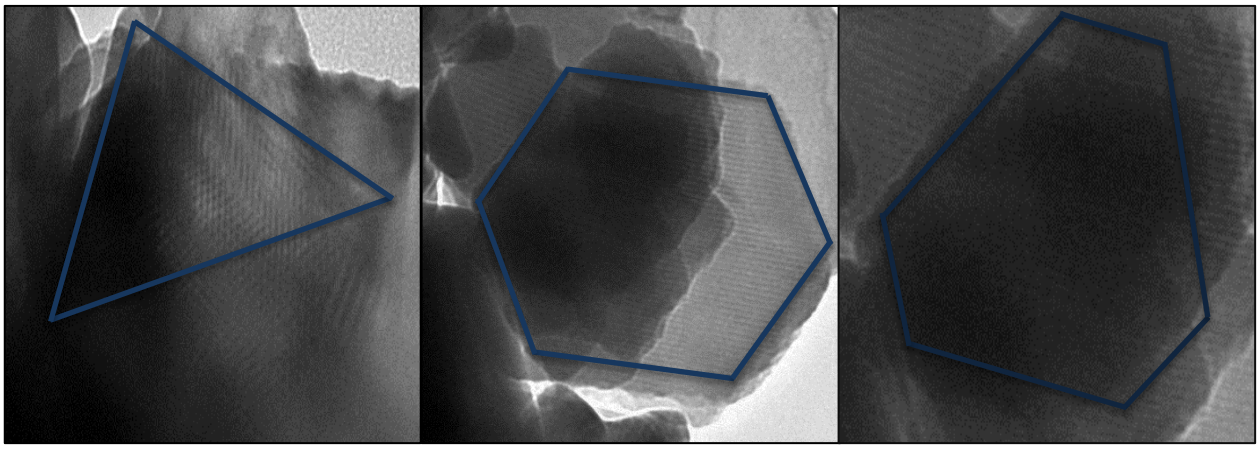


Figure 4.10: Morphology transition from 1D to 2D Shape of $CuInTe_2$ with increasing reaction time.

The crystal structure and phase composition evolution with reaction time was determined by XRD and the results are shown in Fig. 4.11. The diffraction patterns of the aliquots extracted at different reaction times are presented below. The observed reflection peaks can be indexed to tetragonal chalcopyrite $CuInTe_2$ phase, which is consistent with the standard PDF#:01-0703086. At low reaction times there is evidence of binary CuTe impurities which vanishes when the reaction time is prolonged to 60 min. Formation of pure $CuInTe_2$ with no impurities, suggest that $CuTe_2$ are monomers during the reaction which gets consumed over prolonged reaction time. The preferred growth in the [111] direction is seen across all the reaction times, although at 15 min the relative intensity of the [111] and [220] peak are almost equal. This is can be attributed to the transition in morphology.

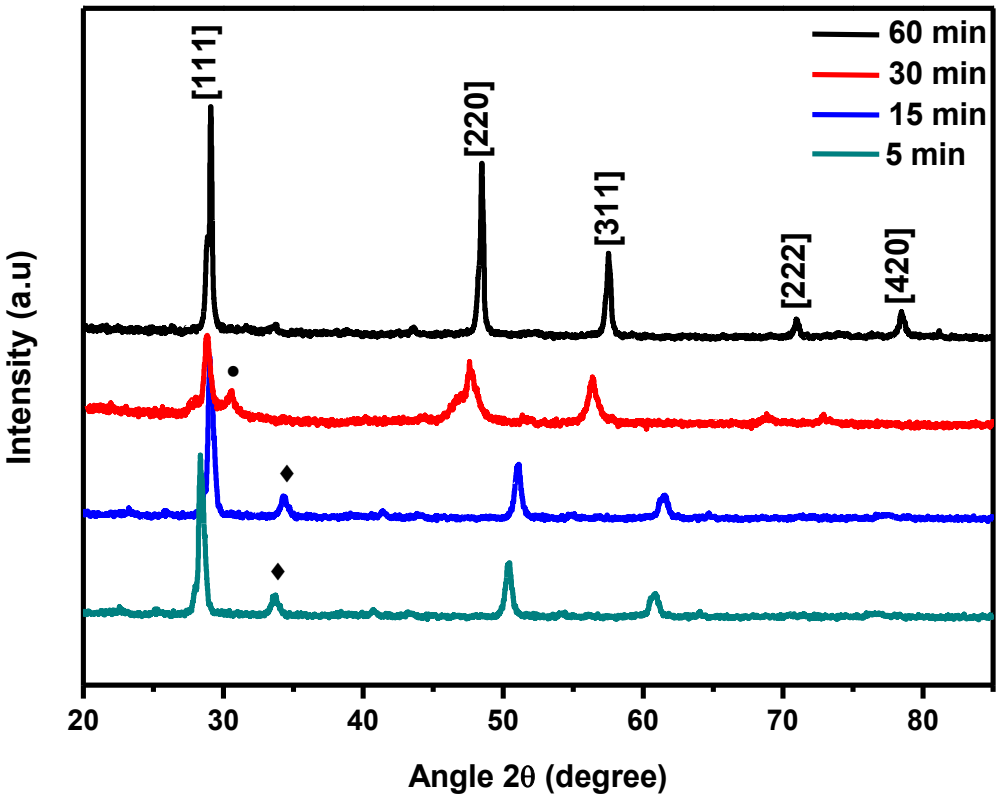


Figure 4.11: XRD patterns of $CuInTe_2$ synthesized at temperature 250 °C and various reaction time where ♦ = Te phase and ● = Cu_5Te_3.

The optical properties of the 2D structures were probed. The obtained spectra are shown in Fig. 4.12. It has been reported that 2D morphology is appealing due to its geometry which allows for a large interface area, hence promoting fast charge transfer between the layers [41-41]. Also reported is that the optical absorption of the 2D nanostructures is thickness dependent [41-41].

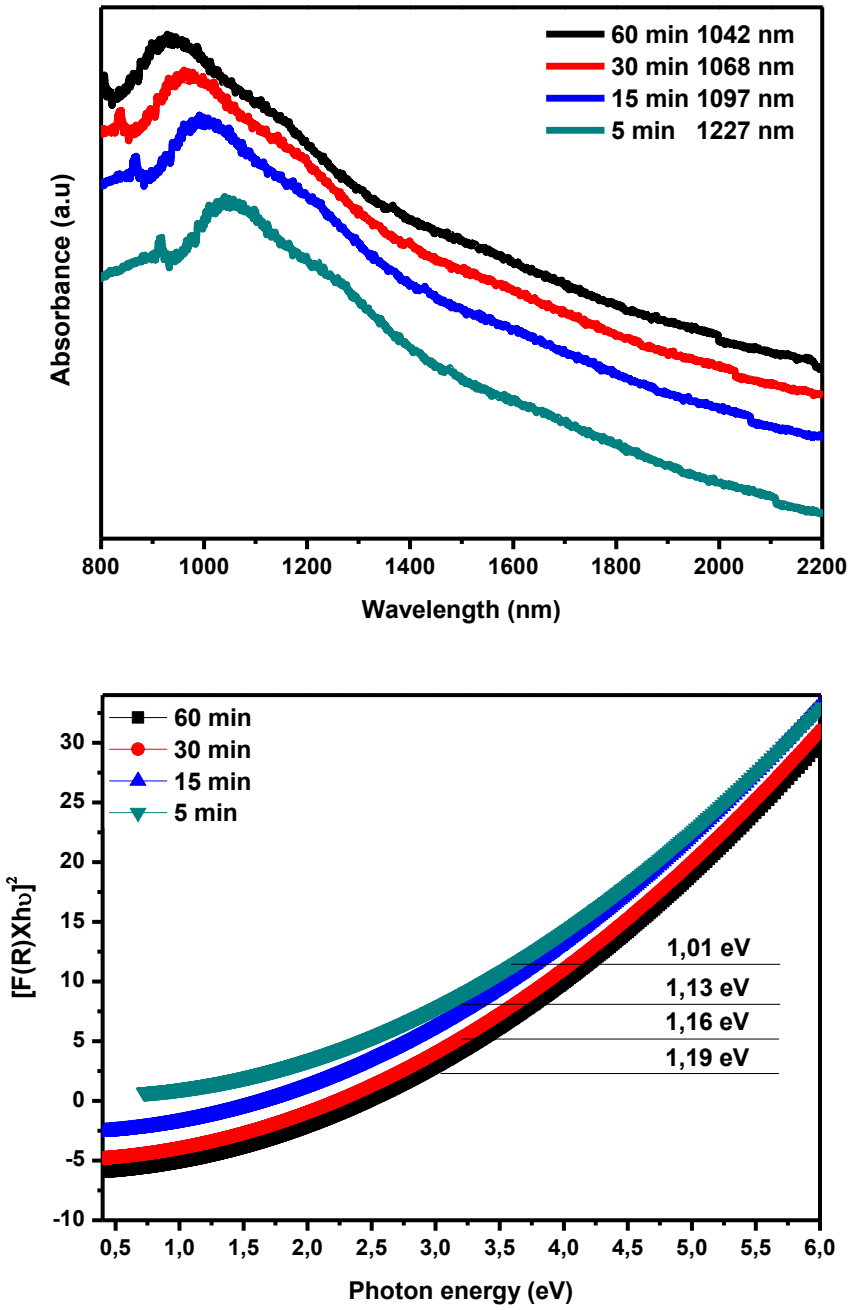


Figure 4.12: UV–Vis–NIR absorption spectra (top) and optical band gap (bottom) of $CuInTe_2$ crystallites synthesized at temperature 250 °C at various reaction times.

In the present study, the materials' absorption band edges are in the near infrared region despite the transition from 1D to 2D shaped particles. As the reaction time is increased, the band edges are blue shifted. At low reaction times, 5 and 15 min, the measured absorption band edges are 1227 nm and 1097 nm respectively. Therefore, indicating that the optical band

gap increased from 1.01 eV to 1.13 eV. This could be due to almost aggregated undefined particles observed at low reaction time (5 min) resulting in bigger particles hence narrower band gap. Upon transition from 1D to 2D at 15 min, there is an increase in the optical band gap. The optical band gap of 1.16 eV corresponding to 1068 nm band edge was obtained for the 30 min sample. The increase in band gap can be attributed to surface defects in 3D geometry. As time increased to 60 min, the optical band gap also increased to 1.19 eV. The increase in the band gap could be due to the formation of hexagonal sheets which have high surface area compared to the triangular or quasi-triangular sheets. In addition, the increase in band gap from 30 min to 60 min was not as pronounced like in the low reaction times. This is attributed to thickness of nanosheets where the shape is quite different however the thickness is quite similar hence similar optical properties.

4.3.3 1D to 2D shape evolution mechanism

Although morphology evolution is governed by the involvement of parameters that are intimately and intricately entangled to each other, an attempt to understand the role played by thermodynamic or kinetic parameter can still be pursued. It is through the understanding of the thermodynamic or kinetic parameter that one can be able to explain morphology evolution for example 1D to 3D evolution [22]. Amongst key parameters, the concentration of the available monomers plays an essential role towards shape evolution of nanocrystals. Previously, evolution of CdS spheres to rods has been reported [42]. The shape evolution was attributed to the availability of the monomer concentration. It was further indicated that the small amount of nuclei and the use of stable precursors was crucial for obtaining monodispersed shape and size [22].

Morphology evolution mechanism of CdSe nanocrystals via self-ripening of individual nanoparticles was first proposed by Peng [42]. The mechanism explains the evolution of elongated CdSe nanocrystals at different growth stages [42-43]. The mechanism states that the transition of morphology of an individual particle at a particular growth stage is significantly dependent on the availability of the monomer concentration [22]. The formation of one dimensional structure was favored by extremely high monomer concentration. As the reaction continues monomers are consumed resulting in a decreased concentration of reacting monomer. If the remaining concentration of reacting monomers drops below a level that is required for the elongated shape, transition from 1D to 2D growth will occur.

We also propose that evolution mechanism from 1D to 2D occurs via self-ripening. At low reaction time (5 min), there is extremely high monomer concentration available, promoting the formation of short rods and other irregular shaped-particles. At 15 min, the formation of flakey rods emerges due to the decrease in monomer concentration. As a result of the dipole-dipole interaction along [100] plane and the hydrophobic surface offered by the surface coordinating agent EDT, nanorods are formed through a self-assembly mechanism. Self-assembled nanorods from ultrathin triangular nanoplates were also observed by Yi and colleagues [27]. They attributed the formation of the nanorods to a decreased size of 2D nanosheets resulting in high degree of overlapping thus forming rod-like structures [27]. Contrary to their findings, 1D to 2D morphology transition was observed rather than 2D to 1D transition in this study. The further the reaction time was prolonged, the self-assembled structures collapsed into different shaped sheets. It is at this stage where the morphology transition from 1D to 2D is initiated. This is an indication that at the concentration of the reacting monomers is below that of elongated structures [22]. At this stage the net monomer exchange between nanocrystals and solution is constant [22]. Therefore, resulting in, a

difference in potential energy between different facets of nanocrystals [22]. The difference in potential energy will initiate the move of the monomer on the nanocrystal in an intra particle manner to convert the 1D rod into the 2D sheet [43]. The collapsing of cylindrical structures can also be attributed to weak Van der Waal interactions [22].

However, there are multiple regular shaped sheets, suggesting that there is a lack of morphology control in a reaction system. Upon increasing reaction time to 60 min, the most stable sheets which are hexagons are seen. Form HRTEM the measured d spacing of all three types of sheets were equal indicating that they are similar in crystal structure. The XRD measurements indicated that the preferred growth direction of the nanocrystals were in both [111] and [220] planes. We therefore propose that the triangular ultra-thin sheets were initially formed. As the reaction continues the high energy facets at the sharp tips continues to grow forming quasi-triangular nanosheets, which eventually grow in to more stable hexagons. The route of formation is illustrated in Fig. 4.13.

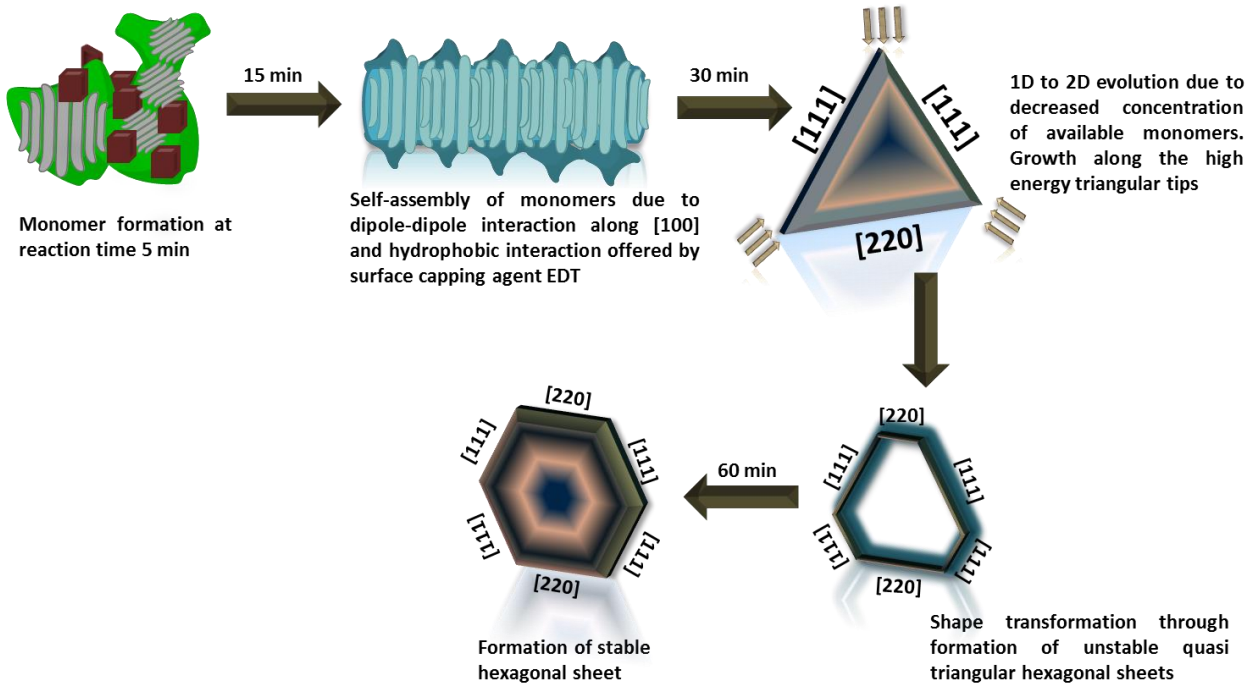


Figure 4.13: The proposed self-ripening mechanism of 1D to 2D morphology transformation.

The lack of homogeneity in the shapes and sizes of the particles can be attributed to the nature of the capping agent as well. While EDT is a desired ligand compared to the long chained alkyl amines such as OLA and HDA due to a number of reasons such as its ability to form sheets which are of course more desirable for devices as charge transfer will be easier. Secondly, the thiol group has higher affinity for the positively charge nanocrystal surface hence ensuring good passivation of the surface which will tend to produce better optical properties. Thirdly, the shortness and the bidentate nature of the ligand ensure a compact network of nanocrystals which is excellent for solar cells hence its use in solar cells as a ligand that exchanges the long alkyl chain. However, it is clear from the obtained results that direct capping is perhaps not a good idea as inhomogeneity and agglomeration results. Nevertheless, the production of nanosheets is highly desirable hence a system containing both a long-chain amine and EDT may be the answer.

4.4 Conclusions

The use of various capping agents gave structures with different geometry thus enabling morphology engineering of the $CuInTe_2$ nanocrystals. The different alkyl amines OLA and HDA produced different shaped particles 1D rods and 3D cubes for HDA and OLA respectively. Binary impurities were detected for both EDT and TOP capping agents, while alkyl amines showed pure $CuInTe_2$ phase. The optical properties of different structures varied with OLA capped particles with the highest optical band gap of 1.22 eV. Morphology evolution of the 2D hexagonal sheets was studied through variation of reaction time. The evolution of hexagonal sheets was through the formation of the self-assembled 1D rods at low reaction time (15 min). As the reaction time increased, there was more monomer consumption which led to formation of triangular structures, further transformed into quasi triangular hexagons finally forming stable hexagonal sheets. XRD was confirmed that the preferred crystal growth were in [111] and [220] planes. There was no phase evolution detected with evolution of triangular and hexagonal structures. However, impurities at low reaction time were detected. It was postulated that 1D to 2D morphology transformation occurred through self-ripening mechanism. The optical band gap increased with increasing reaction time.

4.5 References

1. Y. Yin and A. P. Alivisatos, *Nature*, 2005, **437**, 664-670.
2. J. Chang and E. R. Waclawik, *RSC Advances*, 2014, **4**, 23505-23527.
3. C. de Mello Donegá, *Chemical Society Reviews*, 2011, **40**, 1512-1546.
4. R. Xie, M. Rutherford and X. Peng, *Journal of the American Chemical Society*, 2009, **131**, 5691-5697.
5. S. Siebentritt and U. Rau, *Wide-gap chalcopyrites*, Springer, 2006.

6. M. Green, *Solar cell efficiency tables (Version 41) Progress in Photovoltaics: Research and Applications*, 2013, **21**, 1-11.

7. V. K. LaMer and R. H. Dinegar, *Journal of the American Chemical Society*, 1950, **72**, 4847-4854.

8. J. van Embden, A. S. Chesman and J. J. Jasieniak, *Chemistry of Materials*, 2015, **27**, 2246-2285.

9. J. Park, J. Joo, S. G. Kwon, Y. Jang and T. Hyeon, *Angewandte Chemie International Edition*, 2007, **46**, 4630-4660.

10. W. Van Der Stam, A. C. Berends and C. de Mello Donega, *ChemPhysChem*, 2016.

11. T. Sugimoto, *Monodispersed particles*, Elsevier, 2001.

12. X. Peng, J. Wickham and A. P. Alivisatos, *Journal of the American Chemical Society*, 1998, **120**, 5343-5344.

13. T. Sugimoto, *Advances in Colloid and Interface Science*, 1987, **28**, 65-108.

14. N. Revaprasadu and S. Mlondo, *Pure and applied chemistry*, 2006, **78**, 1691-1702.

15. X. Peng, L. Manna, W. Yang, J. Wickham, E. Scher, A. Kadavanich and A. P. Alivisatos, *Nature*, 2000, **404**, 59-61.

16. J. Hu, L.-s. Li, W. Yang, L. Manna, L.-w. Wang and A. P. Alivisatos, *Science*, 2001, **292**, 2060-2063.

17. Y. Xia, X. Xia and H.-C. Peng, *Journal of the American Chemical Society*, 2015, **137**, 7947-7966.

18. S. Mourdikoudis and L. M. Liz-Marzán, *Chemistry of Materials*, 2013, **25**, 1465-1476.

19. N. Ortiz and S. E. Skrabalak, *Langmuir*, 2014, **30**, 6649-6659.

20. A. R. Tao, S. Habas and P. Yang, *small*, 2008, **4**, 310-325.

21. Y. Xiong, B. J. Wiley and Y. Xia, *Angewandte Chemie International Edition*, 2007, **46**, 7157-7159.

22. G. Jia, S. Xu and A. Wang, *Journal of Materials Chemistry C*, 2015, **3**, 8284-8293.

23. C. J. Murphy, T. K. Sau, A. Gole and C. J. Orendorff, *Mrs Bulletin*, 2005, **30**, 349-355.

24. C. S. Weisbecker, M. V. Merritt and G. M. Whitesides, *Langmuir*, 1996, **12**, 3763-3772.

25. H. Döllefeld, K. Hoppe, J. Kolny, K. Schilling, H. Weller and A. Eychmüller, *Physical Chemistry Chemical Physics*, 2002, **4**, 4747-4753.

26. T. K. Sau and A. L. Rogach, *Advanced Materials*, 2010, **22**, 1781-1804.

27. L. Yi and M. Gao, *Crystal Growth & Design*, 2011, **11**, 1109-1116.

28. J. Makinson, J. Lee, S. Magner, R. De Angelis, W. Weins and A. Hieronymus, *Advances in X-ray Analysis*, 2000, **42**, 407-411.

29. M. Thwaites, R. Tomlinson and M. Hampshire, *physica status solidi (b)*, 1979, **94**, 211-214.

30. D. Sridevi and K. V. Reddy, *Thin Solid Films*, 1986, **141**, 157-164.

31. P. Kubelka and F. Munk, *Z. Tech. Phys*, 1931, **12**.

32. C. Kim, D. H. Kim, Y. S. Son, H. Kim, J. Y. Bae and Y. S. Han, *Materials Research Bulletin*, 2012, **47**, 4054-4058.

33. D. C. Onwudiwe, M. Hrubaru and E. E. Ebenso, *Journal of Nanomaterials*, 2015, **2015**.

34. Q. Wang, D. Pan, S. Jiang, X. Ji, L. An and B. Jiang, *Journal of crystal growth*, 2006, **286**, 83-90.

35. S. M. Wasim, A. LaCruz Vielma and C. Rincón, *Solid State Communications*, 1984, **51**, 935-937.

36. H. Neumann and R. Tomlinson, *Solid state communications*, 1986, **57**, 591-594.

37. D. Redfield, *Physical Review*, 1963, **130**, 916.

38. C. Rincón, *Solid state communications*, 1987, **64**, 15-17.

39. S. Wasim and J. Albornoz, *physica status solidi (a)*, 1988, **110**, 575-583.

40. N. Moloto, H. Puggens, S. Govindraju, B. Rakgalakane and M. Kalenga, *Thin Solid Films*, 2013, **531**, 446-450.

41. V. L. Bridewell, R. Alam, C. J. Karwacki and P. V. Kamat, *Chemistry of Materials*, 2015, **27**, 5064-5071.

42. Z. A. Peng and X. Peng, *Journal of the American Chemical Society*, 2001, **123**, 1389-1395.

43. X. Peng, *Advanced Materials*, 2003, **15**, 459-463.

Chapter 5: Time, precursor, surfactant and stoichiometry dependency of quaternary $CuIn_{1-x}Ga_xTe_2$ nanostructured semiconductor materials

5.1 Introduction

Band gap tailoring of nanostructured ternary copper chalcogenides has rendered them interesting materials for several applications such as light-emitting diodes, solar cells, bio-imaging and so on [1]. Among these devices, solar cells fabricated based upon $CuInGaSe_2$ (CIGS) photo absorber layers have been reported with 20% efficiency [1]. The extensive use of these materials as photo-absorber in thin-film solar cells is due to their non-toxic nature. They are also p-type semiconductors with a direct band gap with exceedingly high optical absorption coefficients that may exceed 10^5 cm^{-1} [2]. They can also be processed into thin layer thickness associated with an increase in shunt conductance and also provides the advantages of reducing the weight of the devices and providing flexibility [3]. Fine tuning of the band gap of these materials is dependent on size and stoichiometry [1]. Control over the size of these materials achieved by employing a balanced multiple precursor reactivities which enable control over the nucleation and the growth process during the reaction [4-5]. The small sized particles generate a quantum confinement effect `which alters the electronic structure to discrete or quantized electronic levels [6]. Therefore, the resulting continuous optical transitions between the electronic bands become discrete and the properties become size-dependent [7].

The stoichiometry variation arises from the defect tolerance of these materials particularly ternary copper chalcogenides nanostructures [8]. These materials are substitutional alloys formed by either mixed cations or mixed anions [8]. The substitution results in the formation

of disorder in the respective cation or anion sublattice [8-9]. The resulting disorder changes the lattice parameters by either increasing or reducing the interatomic distance or bond lengths (Fig 5.1) [10]. Furthermore, the difference in the cation and anion electronegativity affects the molecular bond strengths [10]. These changes in the crystal structure will result in a shift in valence band maximum (VBM) thus widening the band gap [10]. The change in the band gap is directly linked to the p-d hybridization which refers to the anion p- and cation d-orbitals [10]. All of these above-mentioned factors were accounted for by the Jaffe, Wei, and Zunger (JZW) model.

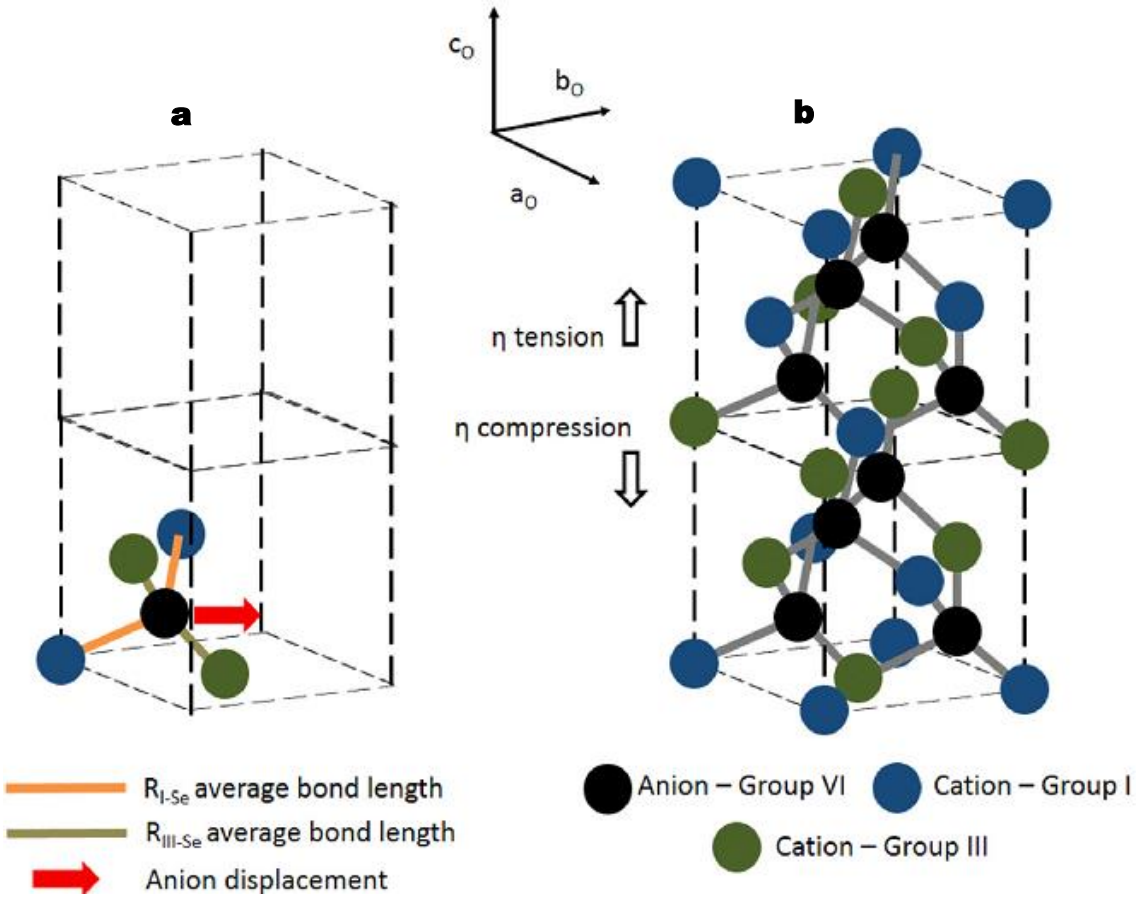


Figure 5.1: Schematic illustration of (a) anion displacement and (b) tetragonal distortion [10].

The proposed JZW theory states that the band gap variation in Cu-based chalcopyrite ternary alloys is due to structural deformation arising from the chemical and structural factors [11-12]. The chemical factors arise from the p-d hybridization and cation electronegativity, while the structural factors are due to tetragonal distortion and anion displacement [11]. Based on this theory, the cation d orbitals and anion p orbitals which make the valence band maximum will shift higher due to the repulsion between the d and p orbitals [11]. The cation electronegativity responsible for charge separation on the cation sublattice will affect the molecular bond strength [11]. Furthermore, the structural contributions due to tetragonal distortion will either result in compression, $c_0/a_0 < 2$, or tension, $c_0/a_0 > 2$ [10]. The resulting internal bond-length or anion displacement will determine the lattice constant a_0 and c_0 [10]. Moreover, a_0 should obey Vegard's rule and c_0 should change at different rates than a_0 [10]. Therefore, suggesting that the change in bond lengths of group I–VI and group III–VI are governed by anion displacement and differences in cation radii [11].

Based on this model studies have been carried out on different pseudobinary or quaternary systems such as $Cu_{1-x}Ag_xGaSe_2$ and $CuIn(S_{1-z}Se_z)_2$ etc. [13]. Wei and co-workers studied the effect of Ga addition on the electronic properties of $CuInSe_2$ [14]. They found that incorporating Ga increases the band gap and that in turn increases the open-circuit voltage [14]. This was attributed to Ga partially replacing In, which was different from $In_{1-x}Ga_xAs$ where cations were fully substituted [14]. They also observed an increase in valence band maximum while conduction band significantly decreased [14]. In other studies, it was reported that 30% critical limit of gallium should not be exceeded as it will result in segregation [15]. Band gap tailoring of $CuInSe_2$ has previously been done by alloying the material with sulphur to form $CuInSSe_2$ [16]. This resulted in increased conversion efficiencies and open-circuit voltage. Varying the relative ratio between S and Se could modify and enhance the optical

and electrical properties [17]. Increased sulphur composition showed high band gap which was attributed to change in lattice constant variation [17]. Moreover, sulphur incorporation resulted in electron distribution deformation due to the alloy atoms' electronegativity differences, and relaxation of anion-cation bond lengths and angles [18].

Though these materials remain the active absorber materials in thin-film solar cells with the highest performance, the reports have only been on the direct deposition of precursors into thin-films, not solution synthesis. Literature shows that processing of thin-film requires expensive vacuum technologies with sophisticated process control [19]. William et al. reported the deposition of $Cu(InGa)Se_2$ by multisource evaporation [20]. It is reported that the incorporation of sulphur and selenium in the absorber thin film is mainly done by high-temperature selenization and/or sulfurization approach [21-22]. This method involves the use of toxic gasses which are harsh to the environment [23]. Other reports showed a lack of stoichiometry control in films which resulted from co-evaporating individual elements [24]. The inability to control stoichiometry degrades the electrical and optical properties thus making the upscaling difficult. Moreover, high temperatures required for processing thin films, escalates the manufacturing costs.

An alternative approach is to develop nanocrystals as the building blocks with desired composition for $CuIn(S_{1-x}Se_x)_2$ absorber thin films [25]. Literature has reported few approaches such as hot-injection [26-27], microwave-assisted synthesis [28], thermal pyrolysis [29-30] and solvothermal reactions [31-32]. Wang et al. conducted a two-step solvothermal process for manufacturing $CuIn(S_xSe_{1-x})_2$ [23]. Initially, $CuInSe_2$ nanocrystals were synthesized by solvothermal method subsequent to that sulphur was incorporated forming $CuIn(S_xSe_{1-x})_2$ [23]. In this study we report on the colloidal synthesis of quaternary $CuIn_{1-}$

$_xGa_xTe_2$ through various metal precursor and capping agents. We also investigate the effect of reaction time on the optical band gap. Band gap engineering of the material is explored via variation in indium (In) and gallium (Ga) concentration.

5.2 Experimental section

5.2.1 Materials

Copper chloride, indium chloride, gallium chloride, tellurium, trioctylphosphine (TOP), hexadecylamine (HDA), 1-dodecanethiol (DDT), gallium(III) acetylacetonate ($Ga(acac)_3$), copper(II) acetylacetonate ($Cu(acac)_2$), indium(III) acetate ($In(acac)_3$),dichloromethane, ethanol, methanol and chloroform

5.2.2 Synthesis procedure

The colloidal synthesis was carried out using a Schlenk line setup as shown in Fig. 5.2. In a $CuInTe_2$ synthesis, HDA (120 mg) was placed in a three-neck bottom then heated to 90 °C under nitrogen thereafter copper chloride (2.5 mmol, 24.74 mg), indium chloride (2.5 mmol, 55.29 mg) were added. The mixture was further heated to 120 °C for 20 min under nitrogen. Then TOPTe was injected and the contents of the flask were further heated to 250 °C. The temperature was maintained at 250 °C for 60 min. The reaction was quenched and the temperature was decreased 60 ^oC. Methanol was added to the solution to flocculate the nanoparticles. The collected particles were centrifuged and dichloromethane, ethanol, methanol and chloroform were used to purify the particles. In the quaternary synthesis of $CuIn_{1-x}Ga_xTe_2$ nanocrystals, $GaCl_3$ was added prior TOPTe injection for metal precursor 1. The synthesis through precursor 2 entailed the use of $Cu(acac)_2$, 0.2 mmol and $In(acac)_3$ and $Ga(acac)_3$. The nanocrystals were either capped in HDA or DDT.

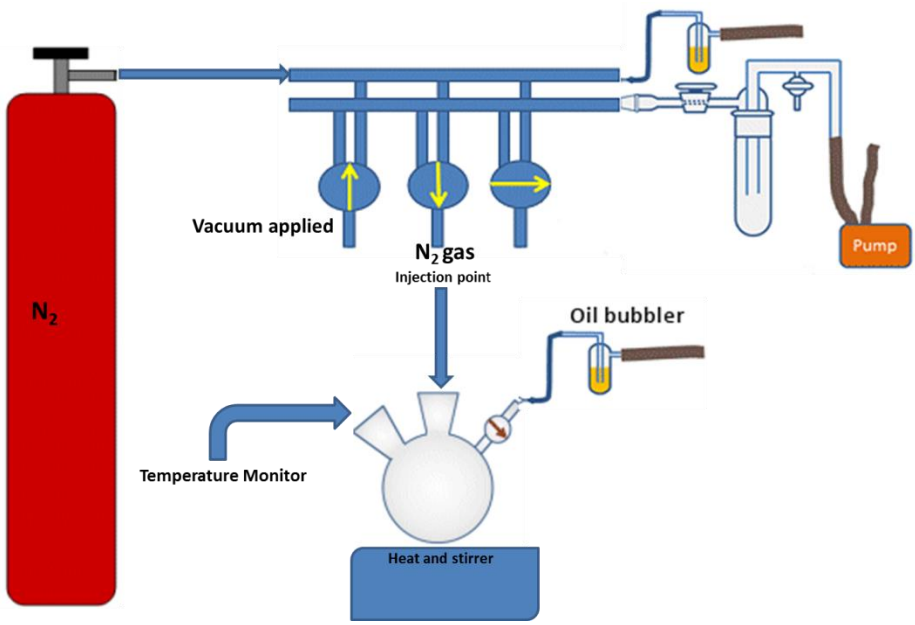


Figure 5.2: Schematic diagram of experimental set-up.

5.2.3 Characterization

XRD patterns of powdered samples were measured on a Bruker MeasSrv D2-205530 diffractometer using secondary graphite monochromated CoKα radiation (λ 1.78897 Å) at 30 kV/30 mA. Measurements were taken using a glancing angle of incidence detector at an angle of 2°, for 2θ values over 20 - 90° in steps of 0.026° with a step time of 37 s and at a temperature of 25 °C. Raman spectroscopy in which the 514 nm emission line from an argon laser done in conjunction with a Horiba Jobin-Yvon LabRAM HR Raman spectrometer was used. The scanning electron microscopy (SEM) results were obtained from FEI Nova Nanolab 600 microscope. The transmission electron microscopy (TEM) was carried out on an FEI Technai T12 TEM microscope with an EDS detector operated at an acceleration voltage of 200 kV with a beam spot size of 20 - 100 nm in TEM mode. UV-Vis to near-Infra Red spectral frequencies were acquired using a 40X UVB microscope objective lens from Thor Labs following electromagnetic excitation using a 244 nm UV probe. The atomic percentages

were determined by inductively coupled argon plasma emission spectroscopy (ICP-OES) on a Genesis ICP-OES Spectro instrument. The solid samples were digested in 5M concentrated HNO_3 solutions.

5.3 Results and discussion

5.3.1 The effect of incorporating gallium

5.3.1.1 Structural properties

In order to effectively study the effect of gallium doping, pure ternary $CuInTe_2$ and quaternary $CuIn_{1-x}Ga_xTe_2$ were initially synthesized. During synthesis, the ratio of Ga to In was 0.5:0.5 (weight percentage). The structural properties of the prepared materials were studied by XRD. The diffraction patterns of the prepared materials are shown in Fig. 5.3. The obtained patterns for pure $CuInTe_2$ (CIT) and $CuIn_{1-x}Ga_xTe_2$ (CIGT) corresponded to PDF#01-0703086 and 01-082-0449 respectively. There are five peaks observed for $CuInTe_2$ indexed as (111), (220), (311), (220) and (420) at 2θ values of 29.2°, 48.6°, 57.6°, 71.0° and 78.8° respectively. The gallium-doped shows characteristic peaks with (111), (220) and (311) planes while the high 2θ peaks have vanished. Formation of impurity has also been detected. This is similar to the findings of Aissaoui et al. who reported the formation of binary alloys in the XRD patterns of $CuInG_{1-x}Te_x$ [24]. Furthermore, the obtained pattern shows that the indium content is higher than the gallium. This is confirmed by a shift in (112) peak (Fig. 5.3 inset). There is a shift in (112) peak from 29.13° to 28.93° 2θ observed for Ga-doped material (Fig. 5.3 inset).

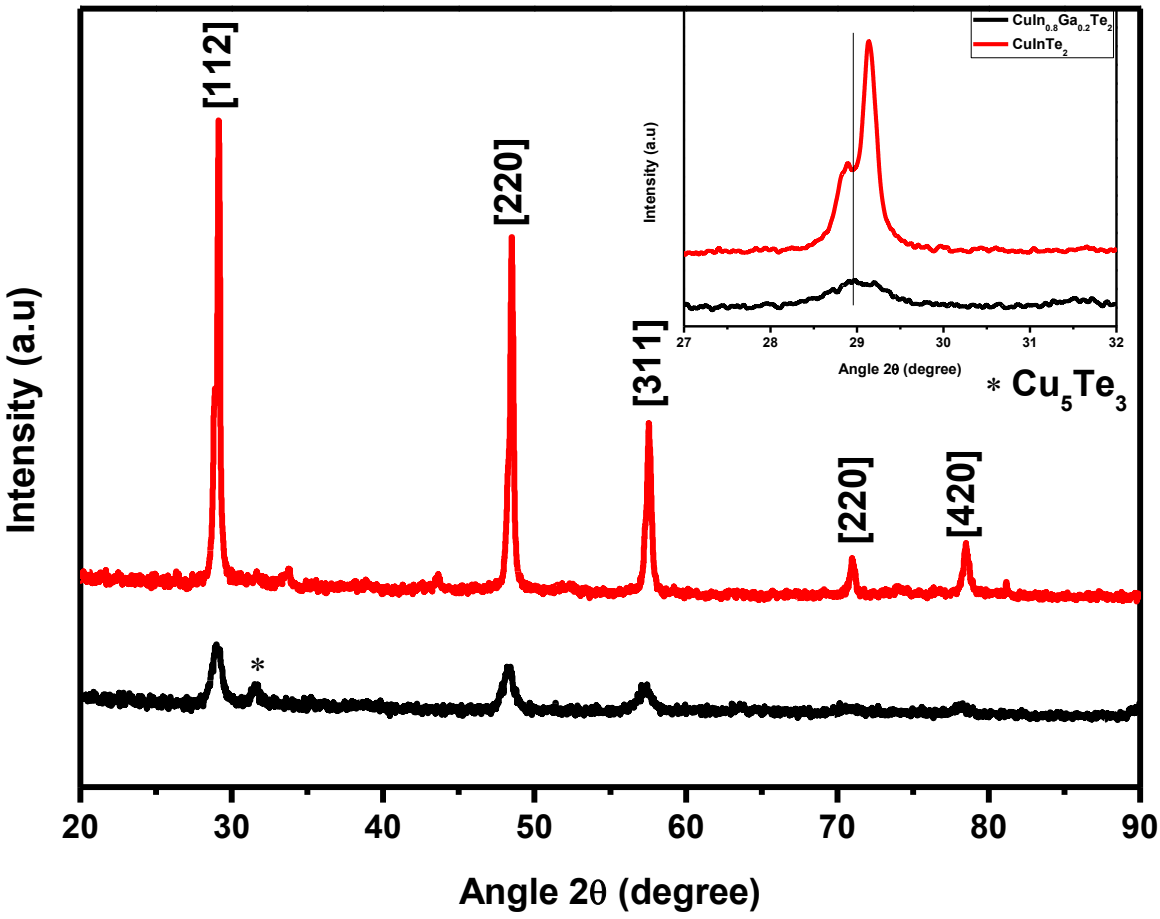


Figure 5.3: (a) XRD patterns of $CuInTe_2$ and $CuIn_{1-x}Ga_xTe_2$ at 250 °C with inset of an expanded view of (111) peak.

This is contrary to the findings of Fiat et al. who saw a shift to higher 2θ values in the (112) peak [2]. It has been reported that the peak position of (112) is dependent on the stoichiometry of In relative to Ga [33]. It has been reported that the peak shift to higher 2θ values is attributed to the increasing content of Ga relative to In [33]. Since we have observed a shift to low 2θ, this confirms that the Ga content is relatively low compared to the In content. The shift in peak position can be quantified by cell parameters *a* and *c*. In Table 5.1 the cell parameters and the grain size of the prepared materials are shown. A decrease in lattice constants *a* and *c* in Ga-doped material is due to the substitution of In atoms with

smaller Ga atoms. This is in good agreement with other chalcopyrite semiconductors such as $CuIn_{1-x}Ga_xSe_2$ crystals [34]. The average crystallite size of the prepared materials was deduced from XRD measurements by applying Debye-Scherrer formula. The grain size tremendously decreased upon incorporating Ga and this is in good agreement with work done by Gabaruci et al. [35].

Table 5.1: Cell parameters and grain size of $CuInTe_2$ and $CuIn_{1-x}Ga_xTe_2$

Material	(112) Peak position (2θ)	*a* (A°)	*c* (A°)	Grain size (nm)	FWHM
$CuInTe_2$	29,13	12.36[a]	6.179[a]	41	0.1998
$CuIn_{0.8}Ga_{0.2}Te_2$	28,93	12.30[b]	6.153[b]	19	0.4344

a = PDF#01-0703086, b = PDF#01-082-0449, FWHM = Full Width at Half Maximum

5.3.1.2 Morphological properties

The morphology of the prepared materials was studied by TEM. TEM micrographs of the synthesized materials are shown in Fig 5.4. From TEM micrographs a stacked cubed like structures are detected for pure $CuInTe_2$. Similarly cubed shaped $CuInTe_2$ structures has previously been attained through hydrothermal synthesis [36]. Upon Ga doping, a change in morphology is observed. A mixture of rods and irregular shaped particles are obtained showing a lack of morphology control. Therefore, suggesting that there was rapid growth of particles during synthesis. The diameter of the CIT cubes is 180 nm while the length and diameter of the rod shape particles is 210 nm and 65 nm respectively. The sizes of both CIT

and CIGT are far bigger than the ones estimated from the XRD. The Scherrer method which uses equation

$$Dp = \frac{K\lambda}{B\cos\theta} \ldots\ldots\ldots\ldots (5.1)$$

were D*p* = average crystallite size, λ= wavelength of the x-ray, K= shape factor equal to 0.9, B= Full Width at Half Maximum (FWHM) of the peak. It was used to estimate grain size from XRD assumes that the shapes of the particles are spherical and is usually an average. This therefore produces significant errors in the calculation however the trend is usually maintained. Hence from Fig. 5.4, it can be seen that the diameter of the rod-shape particles is much smaller than the cube particles.

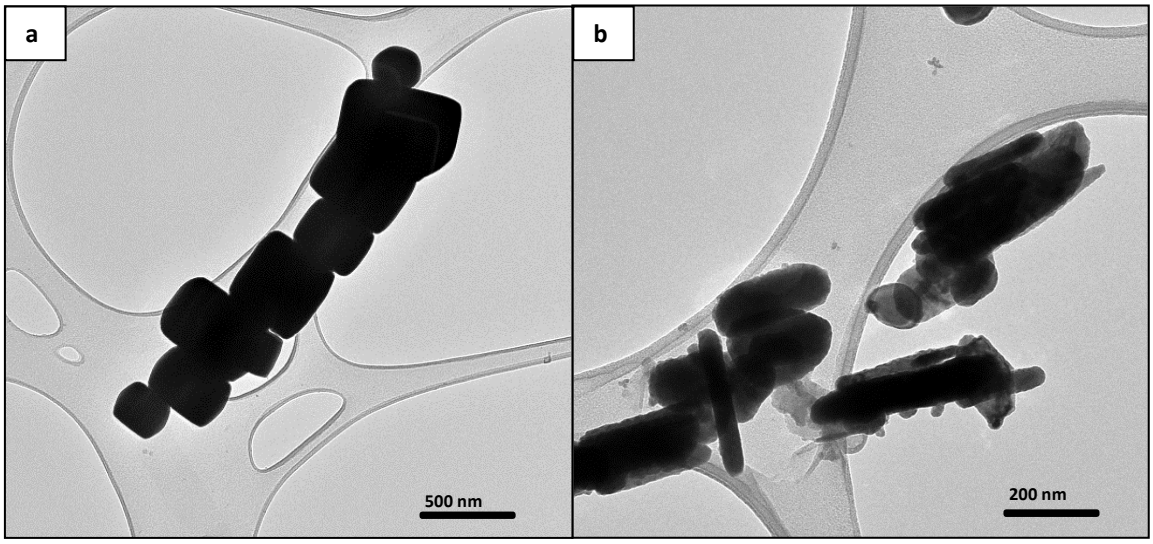


Figure 5.4: TEM micrographs of (a) $CuInTe_2$ and (b) $CuIn_{0.8}Ga_{0.2}Te_2$ semiconductor materials synthesized at 250 °C.

5.3.1.3 Raman analysis

Raman spectroscopy of the synthesized materials was performed and the related spectra are shown in Fig. 5.5. For the CIT material only 5 modes at 131, 149, 175, 216 and 244 cm^{-1} were detected. The observed frequencies corresponded with A_1, B_1, E, E and B_2+E^3 modes respectively. The observed modes coincided with what has been reported in the literature [37]. For the Ga-doped material the most intense line appears at 137 cm^{-1} corresponding to A_1. The

A_1 mode appears at high frequency for CIGT than that of pure CIT, this is due to the presence of Ga. This line originates from the motion of Te atoms with Cu and Ga atoms at rest [37]. This mode is comparable to peak observed at 138 cm^{-1} for $CuGaTe_2$ [37]. The other intense line at 161 cm^{-1} corresponds to B_2/E mode. The weak E modes are observed at high frequency. Their frequencies are 205, 231 and 275 cm^{-1}. The E modes at 205 and 231 cm^{-1}, have also been observed at a lower frequency for $GuGaTe_2$ [37]. The weak B_1 mode at 275 cm^{-1} arises from the motion of the cations in antiphase which is expected to be very weak [38]. The IR studies conducted showed that the B_1 mode at high frequency is inactive [37]. On the other hand lines at 239 and 273 cm^{-1} have been reported for $CuGaSe_2$ which have been attributed to the E symmetry [37]. Therefore, the possibility that the line at 275 cm^{-1} corresponds to E symmetry cannot be ruled out.

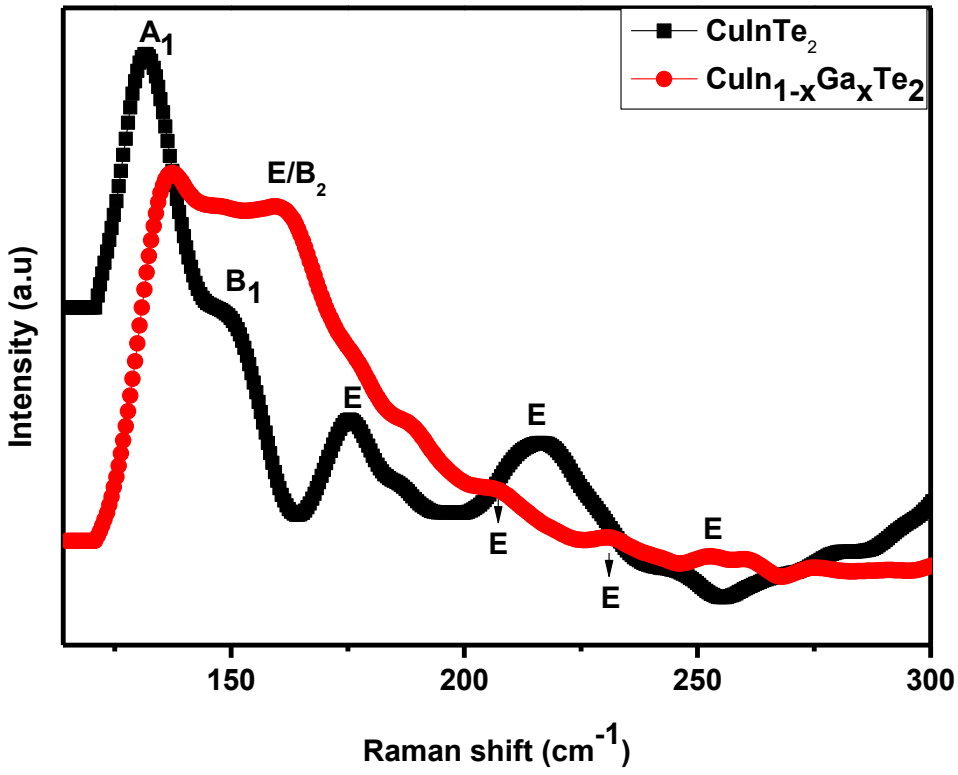


Figure 5.5: Raman spectra of $CuInTe_2$ and $CuIn_{1-x}Ga_xTe_2$ materials synthesized at 250 °C.

5.3.1.4 Optical properties

In order to determine and confirm the band gap of the synthesized semiconductor materials, the absorption measurements were conducted and the optical energy band gaps were deduced by Kubelka-Munk function. The absorption spectrum s is presented below in Fig. 5.6. The spectra confirm that both pure and doped semiconductor materials absorb in the near infrared region. Upon Ga doping, a shift to shorter absorption wavelengths is observed thus an increasing optical band gap. An absorption peak at 1009 nm is observed for $CuInTe_2$ and the extrapolated optical band gap is 1.22 eV. This is similar to the reported band gap of 1.26 eV $CuInTe_2$ polycrystalline thin films [[39]]. The deduced band gap is governed by the allowed electron transitions from the valence band to the conduction band. These transitions are from Γ_6 or Γ_7 in the valence band to Γ_6 level in the conduction band. The Γ_6 and Γ_7 levels result from the spin-orbit interaction.

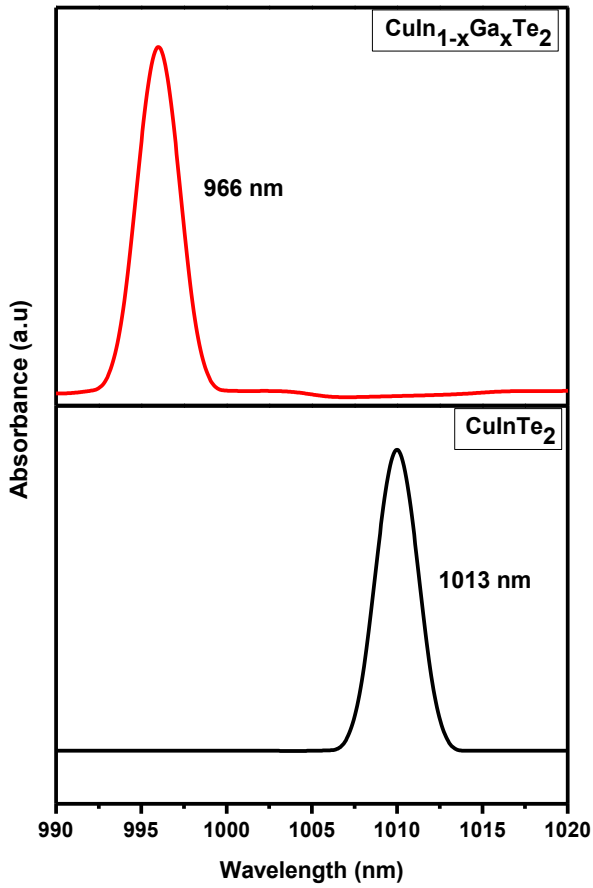


Figure 5.6: Absorbance spectra of $CuInTe_2$ and $CuIn_{0.8}Ga_{0.2}Te_2$ materials synthesized at 250 °C.

The Ga doped semiconductor material was found to absorb at 966 nm. The optical band gap was determined for the absorption band edge and the value is 1.27 eV. The obtained optical band gaps in the present study are comparable to that that reported on $CuGa_{0.25}1n_{0.75}Se_2$ thin films [40]. The studies confirmed three allowed optical band gaps which are Eg_1= 1.16 eV, Eg_2 = 1.22 eV and Eg_3 = 1.38 eV [40]. In the present study, the optical band gap of 1.24 eV corresponds with Eg_2 = 1.22 eV, which is a transition originating from a crystal-field split level to the conduction band minimum [40]. The second band gap agrees with Eg_3, resulting from a spin-orbit split level to the conduction band minimum [40]. There is an increase observed in the optical band gap upon incorporating Ga. A similar effect was reported for $CuIn_{1-x}Ga_xSe_2$ polycrystalline thin films [41]. It was found that when In is replaced by Ga it

affected only half of the cations in the chalcopyrite unit cell [42]. In addition to that, there was a reduced bond length between III-Se which reduced the p-d hybridization [42]. This brought conduction band minimum close to the vacuum level thus band gap widening [42]. The increased s-s orbital repulsion also contributed to an increase in band gap [42]. It has to be considered that in the present case the same effects can be the reason for the observed increase in the optical band gap. However, other studies showed that due to the large Te radius compared to Se, the optical band gap of $CuInGaSe_2$ should be higher than that of $CuInGaTe_2$ films [2]. Therefore, in the present case the high band gap originates from the structural differences. It is known that the structure of the material is different from that of the films. Moreover, the synthetic method followed during preparation greatly influences the structure of the film or material thus changes the lattice parameter. This is consistent with the XRD analysis.

5.3.2 The effect of metal precursors

It has been emphasized that the rational selection of precursors is the key consideration in the synthesis of monodispersed colloidal chalcogenides nanocrystals [43]. This is due to the complexity accompanied by the stability and reactivity of precursor particularly when attempting to yield highly monodispersed pure nanocrystals [43]. This is particularly important since the interaction of metal precursor and coordinating ligands react according to the HSAB principle [44]. It states that the affinity between metal centres (Lewis acids) and coordinating ligands (Lewis bases) will be higher if they share similar “hard” or “soft” properties [45]. Therefore, the hard ligand will associate more strongly to a hard metal than a soft ligand, and vice versa [45]. This is due to the formation of strong ionic bond compared to the covalent bond formation when soft metal interact with soft ligand [44].

According to the HSAB principle hard acid or base is defined by weak polarization which arises from the small atomic radii and a high oxidation state [46]. On the other hand, highly polarizable acids and bases due to their larger atomic radii and low oxidation states are referred to as soft [46]. As a result, it is important to consider the strength interaction of the competing ligands and metal precursors as they control the nucleation and growth of nanocrystals [44]. For example, precursors with weak metal-ligand bond will have increased monomer available which facilitates rapid nucleation [44]. However, strong ligand coordination will be required to stabilize and halt uncontrolled particle growth and aggregation [44]. Failure to achieve this balance will lead to monomers in the solution diffusing in the particle surface [47]. In the absence of dynamic exchange, the nanocrystals will be kinetically inert and will fail to grow [47]. This could potentially be the reason it was difficult to achieve high gallium content doping as seen in the previous section.

Due to the lack of particle growth controlled which led to low gallium content doping and formation of binary impurities; we explore the use of a different metal precursor. In this section synthesis of quaternary $CuInGa_{1-x}Te_2$ was done by using (Precursor 1 and Precursor 2 ($Cu(acac)_2$, 0.2 mmol and $In(acac)_3$ and $Ga(acac)_3$.).

5.3.2.1 Structural properties

During synthesis metal precursor 1 and precursor 2 were employed and the concentration of In and Ga was kept similar. Therefore implying that the value of x is equivalent to 0.5.In order to determine the effect of metal precursor on the crystal structure, XRD studies were conducted. The obtained diffraction patterns of the synthesized material are presented below in Fig. 5.7. Based on the obtained diffraction patterns, precursor 1 and 2 follow the crystal structures $CuIn_{0.8}Ga_{0.2}Te_2$ (PDF#:01-082-0449) and $CuIn_{0.2}Ga_{0.8}Te_2$ (PDF#:01-082-0447)

respectively. Three main peaks were identified with the (112) plane being the most prominent peak for both precursors. Additional peaks with reflection (220) and (312) planes were detected. This is in agreement with Fiat et al. who reported similar reflections corresponding to the chalcopyrite CIGT films [15].

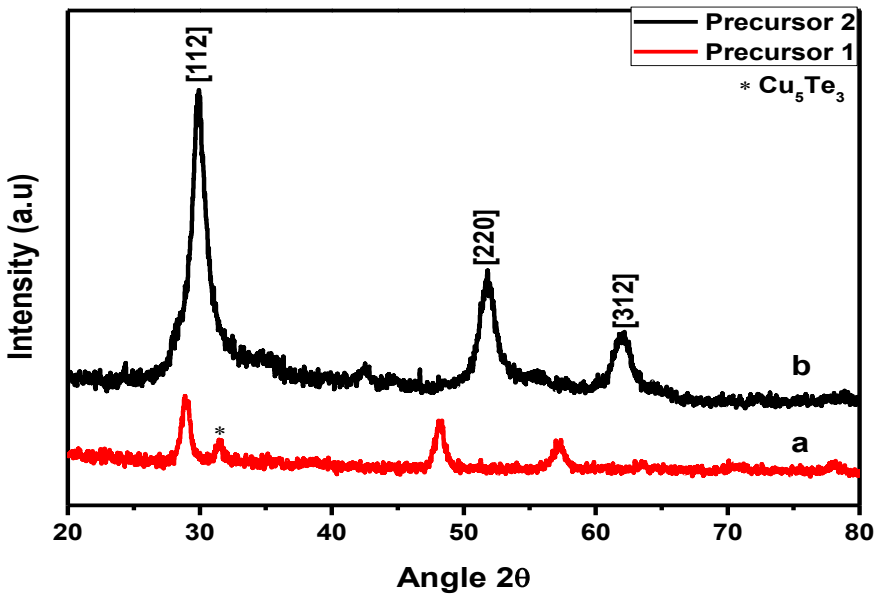


Figure 5.7: XRD patterns of $CuIn_{1-x}Ga_xTe_2$ synthesized with (a) Precursor 1 and (b) Precursor 2.

There is peak shift to high 2θ values observed for precursor 2 with the (112) peak indicating the preferred orientation detected at 29.91° while for precursor 1 it was seen at low 2θ value 28.92°. The shift in (112) peak to high 2θ values is attributed to high Ga content in relative to In [15]. Therefore increasing Ga content will result in a peak shift to high 2θ values. Peak shift for (220) and (312) planes appears to be more significant compared to the (112) plane. The (220) plane shifted from 48.17° to 51.75° while the (312) moved from 57.21° to 62.08°. Contrary to the reports, the detected peaks appear at a slightly high angle compared to the bulk material [48]. The difference in peak positions could be originating from the different

synthetics methods used and processing conditions. For example Aissauoi and colleagues observed the (112) peak at 25.47° for bulk $CuIn_{0.22}Ga_{0.78}Te_2$ [48].

Also noticed is that the experimental molar ratio of In and Ga is lower than the theoretical ratios used during the reaction. The detected In to Ga molar ratios are in agreement with ICP measurements in Table 5.2 though there is a slight decrease. The loss in Ga can further be attributed to $GaCl_3$ hydrolysing as a strong acid when dissolved in OLA forming more $Ga(OH)_3$. Therefore, suggesting that OLA is acting as both solvent and reducing agent. As a reducing agent, OLA and $GaCl_3$ react according to HSAB theory, where strong acid will react readily with strong base [44]. The detected binary impurities can be attributed to the strong affinity of Cu^{+1} ions as soft acids to Te^{-2} ions as soft bases [44]. They react fast and form stronger bonds thus hindering bond formation between indium and tellurium. On the contrary high gallium content was achieved and there no impurities detected in precursor 2. There indicating that precursor 2 shows enhanced synthesis of quaternary $CuIn_{1-x}Ga_xTe_2$ nanocrystals. The variation in molar ratio is further confirmed by high values of lattice parameters **a** and ***c*** in Table 5.3.

Table 5.2: ICP measurements of $CuIn_{1-x}Ga_xTe_2$ synthesized with various precursors

Sample	In:Ga (theo)	Cu at%	In at%	Ga at%	Te at%	In:Ga (cal)
Precursor 1	0.5:0.5	28.00	18.39	3.504	50.10	0.84: 0.16
Precursor 2	0.5:0.5	28.14	5.47	16.41	49.98	0.25: 0.75

Table 5.3: Lattice parameters and shift in peak position of $CuIn_{1-x}Ga_xTe_2$ synthesized in different precursors. .

Sample	(112) peak angle 2θ	*a (A°)*	*c (A°)*
Precursor 1	28.92	6.15[a]	12.30[a]
Precursor 2	29.91	6.05[b]	12.03[b]

a = PDF#:01-082-0449, b = PDF#:01-082-0449

5.3.2.2 Optical properties

The stoichiometry variation in In to Ga ratio was detected by XRD and formation of binary impurities in precursor 1. This indicates variation in the optical properties of both precursors. PL and UV-Vis measurements were conducted to study the optical properties of the synthesized materials and the spectra are presented below in Fig. 8. The band gap energy of the quaternary semiconductor nanocrystals is compositional dependent [49]. Their band gap value can be varied between the values of their ternary counterparts [49]. For example the band gap values may vary from 1.06 eV for $CuInTe_2$ to 1.25 eV for $CuGaTe_2$ [24], therefore allowing band gap engineering for different applications. Based on the obtained results, the absorption band edge varied from 1013 nm to 966 nm for precursor 1 and 2 respectively. The corresponding band gap energy values were 1.22 and 1.28 eV for precursor 1 and 2 respectively. The transitions are due to intrinsic defects [24]. These value are in reasonable agreement with the reported values [24].

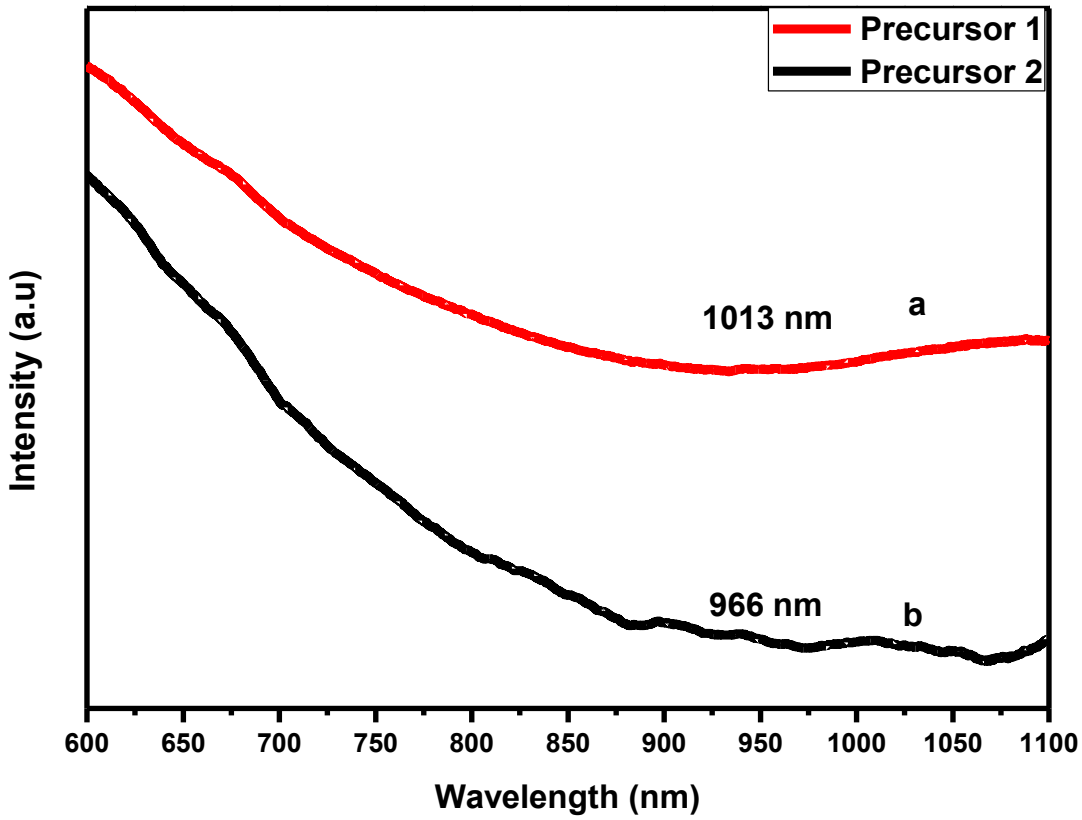


Figure 5.8: UV-Vis absorption spectra of (a) $CuIn_{0.84}Ga_{0.16}Te_2$ synthesized with Precursor 1 and (b) $CuIn_{0.25}Ga_{0.75}Te_2$ with Precursor 2.

PL measurements (Fig. 5.9) exhibit emission values of .1.67 eV for precursor 1 and 1.70 eV for precursor 2. Krustok et al. first reported photoluminescence bands higher than optical band gap of $CuGaTe_2$ [50]. The difference in the emission was attributed to quantum interference between discrete level and continuum [51]. The interference was explained by the resonant acceptor states model in the valence band of the material [51].

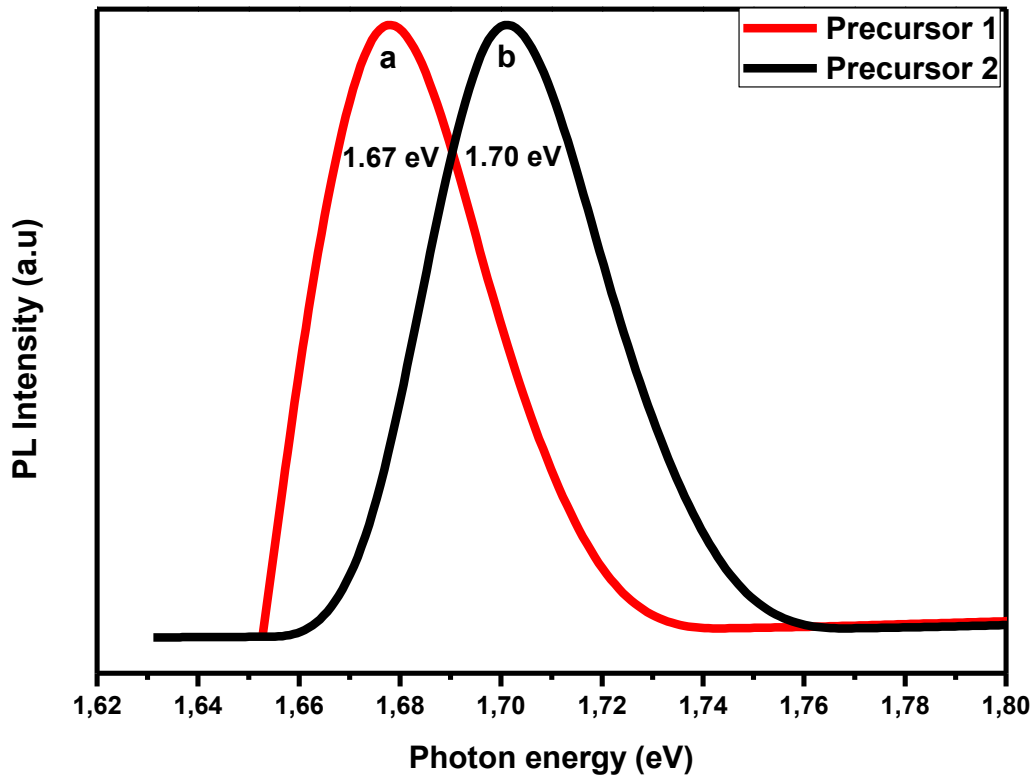


Figure 5.9: PL emission spectra of (a) $CuIn_{0.84}Ga_{0.16}Te_2$ synthesized with Precursor 1 and (b) $CuIn_{0.25}Ga_{0.75}Te_2$ with Precursor 2.

On the other hand high energy transitions at 1.67 eV were first reported by Thwaites et al. from electro-reflectance studies [52]. The high energy transitions where from spin-orbit-split valence band level to the conduction band minimum [52]. Therefore our results are consistent with reports in the literature [52]. Since the synthesized materials are not copper deficient, we can attribute the observed emission to the free-to bound involving V_{cu} and the conduction band. Due to high stoichiometry tolerance of the materials the band gap will be influenced by the interaction d orbital Cu and p level Te [24]. The increased band gap is due to the weak hybridization and reduced d like character above the valence band [24].

5.3.2.3 Morphological properties

Using two different precursors resulted in the formation of different shaped particles (Fig. 5.10). A mixture of spheres and rod structures were achieved when precursor 1 was used. Mixed shaped structures indicate lack of morphology control, which could result from formation of different structural phases. Monodispersed spherical structures were obtained upon changing to precursor 2. However, black lumpy particles were detected indicating particle agglomeration. Precursor 2 shows improved control of over morphology.

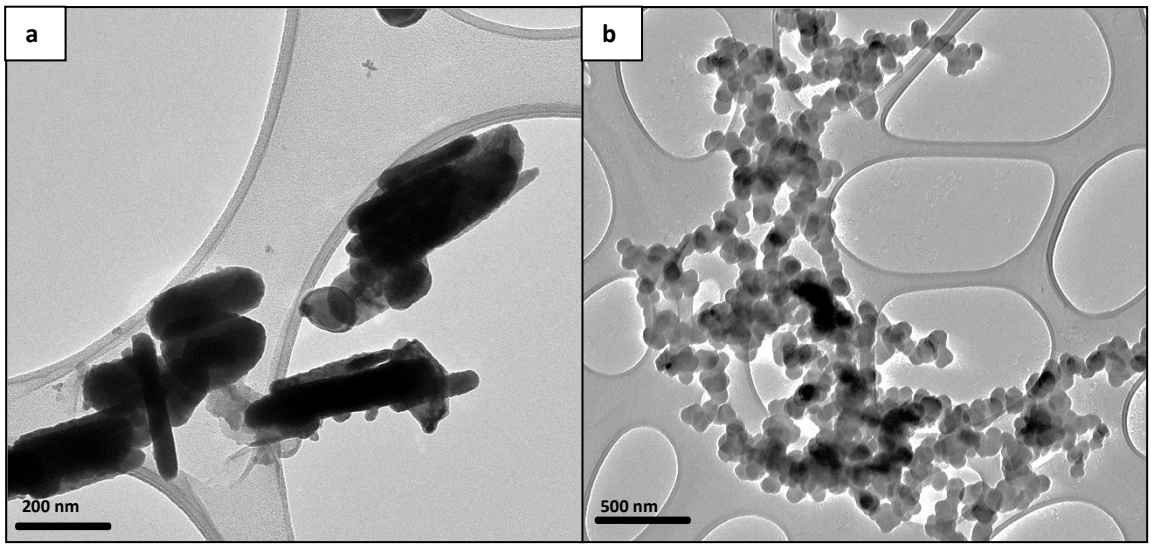


Figure 5.10: TEM micrographs of (a) $CuIn_{0.84}Ga_{0.16}Te_2$ and (b) $CuIn_{0.25}Ga_{0.75}Te_2$ synthesized with Precursor 1 and with Precursor 2 respectively.

5.3.3 The effect of reaction time on CIGT synthesized using precursor 2

5.3.3.1 Structural properties

Since it is known that a slight change in conditions during colloidal synthesis may have a crucial impact on the optical and structural properties of the material, we further investigated the effect of reaction time. As previously reported that thermodynamic and kinetic parameters involved in colloidal growth of nanocrystals are intricately entangled to each other [53].

Therefore, achieving optimum synthesis conditions requires exploring one parameter at a time. We carried synthesis over a short period of 30 min and later extended the reaction time to 60 min. The ratio of In to Ga was kept the same throughout different reaction times. XRD analysis was conducted to study structural properties with a change in reaction time. From the XRD pattern (Fig. 5.11), three main peaks were distinguished corresponding to the chalcopyrite phase. The corresponding reflection indices were (112), (220) and (320) for the reaction at 30 min corresponding to peak positions at angle 2θ 29.56°, 51.60° and 61.94°. There is a shift in peak positions of the material synthesized at prolonged reaction time 60 min. The detected reflection (112), (220) and (320) are observed at angle 2θ 29.79°, 51.96° and 62.17°. The shift in peak positions could be due to change in molar ratio of In and Ga.

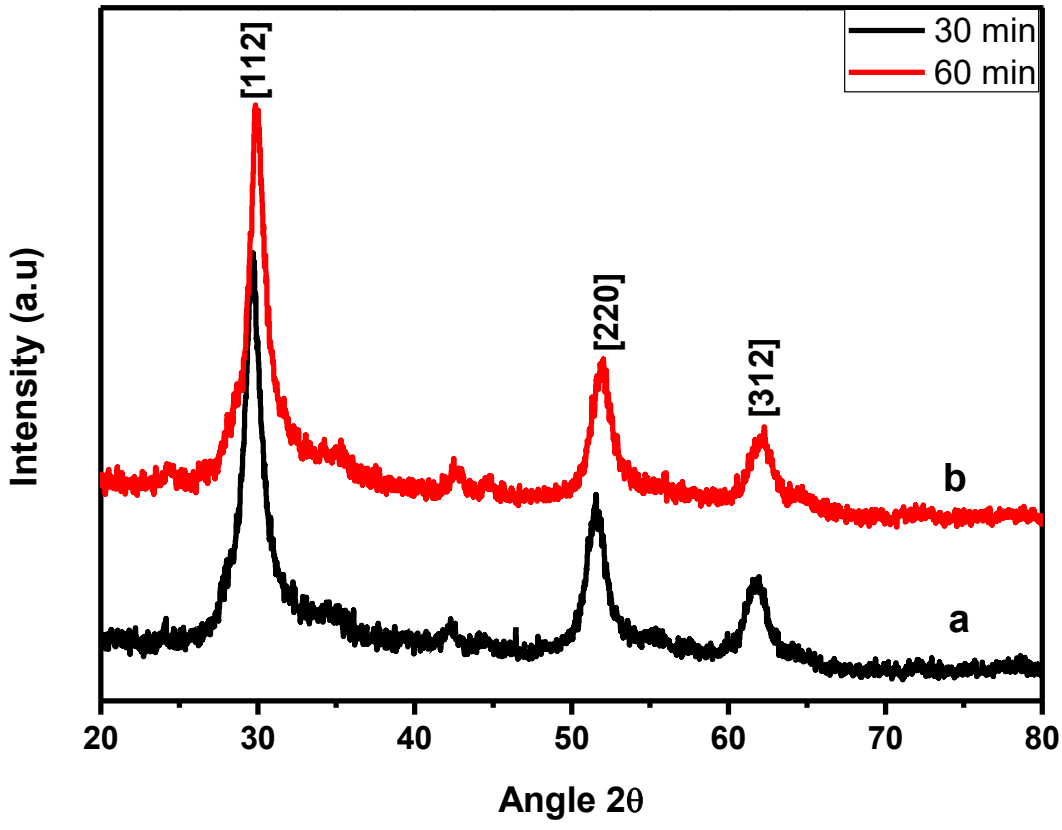


Figure 5.11: XRD patterns of $CuIn_{1-x}Ga_xTe_2$ synthesized at reaction time (a) 30 min and (b) 60 min.

This is consistent with ICP results in Table 5.4. Although the actual In to Ga ratios are lower than the intended ratios, which could be due to $In(acac)_3$ being more reactive than $Ga(acac)_3$ [54]. The (110) peak shows the highest intensity, indicating the preferred growth direction. There was no phase evolution observed with prolonged reaction times. Formation of binary impurities was not detected.

Table 5.4: Composition of $CuIn_{1-x}Ga_xTe_2$ calculated from ICP at different reaction times

Reaction time (min)	Cu at%	In at%	Ga at%	Te at%	In:Ga (cal)	Particle size (nm)	FWHM
30	28.00	11.82	10.07	50.10	0.52: 0.46	45	0.1808
60	28.14	11.61	10.29	49.98	0.53: 0.47	60	0.1368

FWHM = Full Width at Half Maximum

This indicates that there is no post synthesis treatments required for compositional phase enhancement. The particle size increased with increasing reaction time from 45 to 60 nm indicating that particle sintering occurs at prolonged reaction times. Particle sintering suggests that synthesis optimization should be at low reaction times. However, lower reaction times should further be explored to evaluate change in phase composition properties and particle size.

5.3.3.2 Optical properties

Both powdered materials synthesized at different reaction time were dispersed in hexane and the absorption and emission measurements were performed. The obtained spectra are present in Fig. 5.12 and 5.13 respectively and the optical band gap values attained from the graphs

are represented in Table 5.5. Upon prolonging the reaction time, we observe an increase in absorption band edge from 966 nm for reaction at 30 min to 980 nm for 60 min. The corresponding band gap values are 1.28 and 1.26 eV for 30 and 60 min respectively. A change in band gap indicates that optical band gaps are dependent on the duration of synthesis. A decrease in the band gap can be attributed to an increase in particle size. For ternary and quaternary chalcogenides nanocrystals variation in reaction time affects particle size of the nanocrystals. The particle size effects are directly related to nucleation and growth of particles which changes with reaction time thus resulting in larger or smaller particles. [55]. A change in particle size affects the conduction and valence band of the materials which are directly linked to the band gap of the nanocrystals, where small sized particles will result in high optical band gap and vice versa. This is in agreement with XRD results (Fig 5.11).

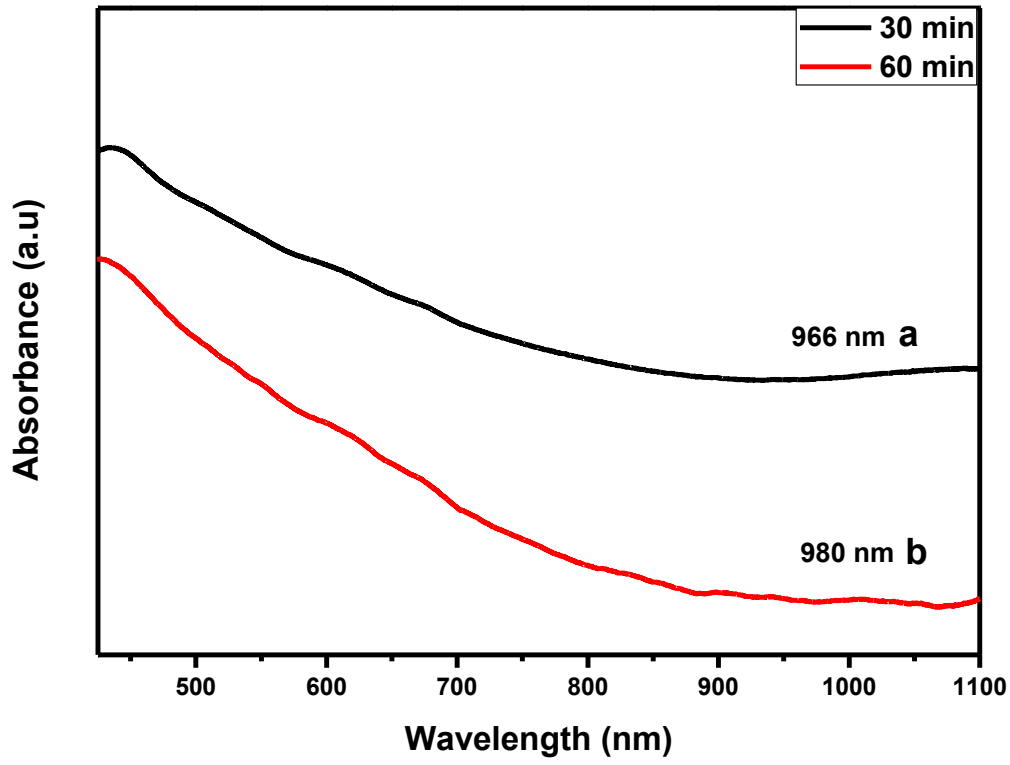


Figure 5.12: UV-Vis absorption spectra of $CuIn_{1-x}Ga_xTe_2$ synthesized at reaction time (a) 30 min and (b) 60 min.

PL spectra in Fig. 5.13 show strong bands for both low and high reaction time. The observed peaks appear to be broad suggesting that high polydispersity in the samples. However, an increase in reaction time resulted in a slight decrease in emission energy of from 168 eV to 1.67 eV which can be ascribed to a change in quantum confinement properties. The emission energy appears to be higher than the absorption by 0.4 eV. This could be due to the unintentional fluctuations often detected by energy dispersive spectroscopy [56], cathodo-[57] or photo-luminescence [58] and capacitance techniques [59]. This could be resulting from either a change in free carrier concentration or localized states [60].

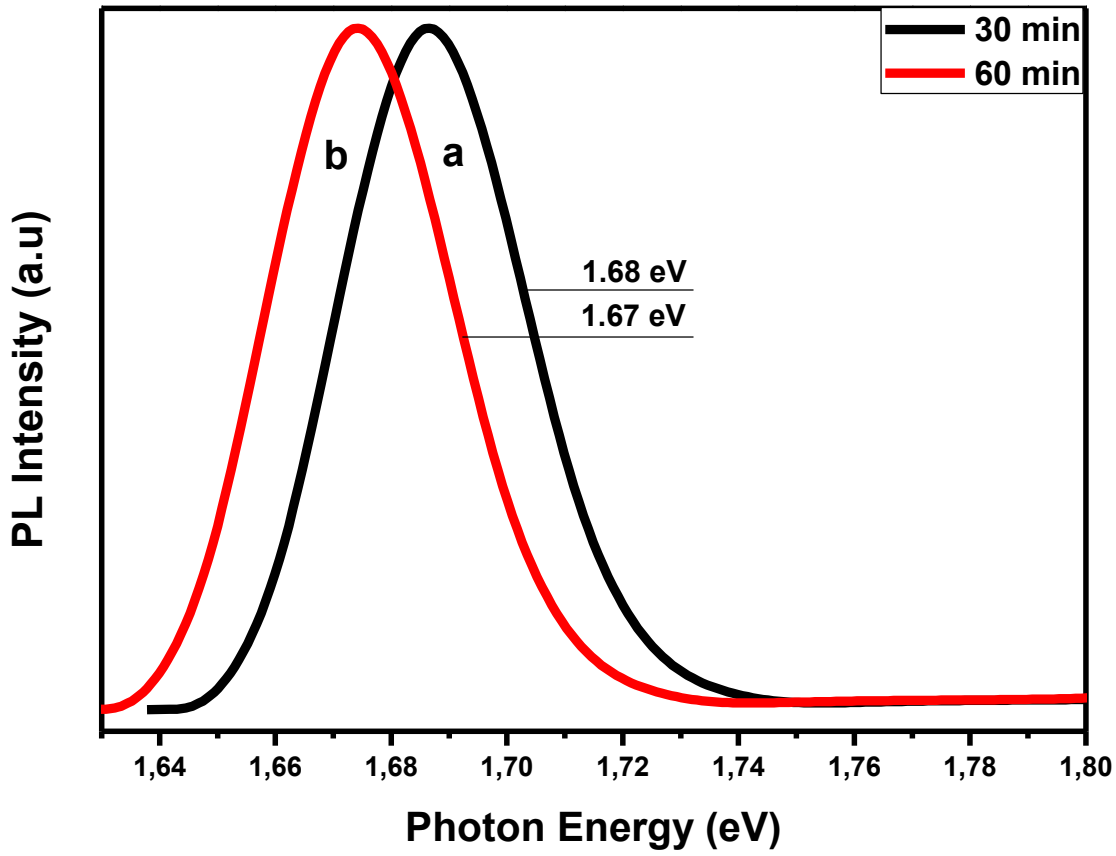


Figure 5.13: PL emission spectra of $CuIn_{1-x}Ga_xTe_2$ synthesized at reaction time (a) 30 min and (b) 60 min.

Table 5.5: Optical properties of $CuIn_{1-x}Ga_xTe_2$ synthesized at various reaction times.

Reaction time (min)	Band edge (nm)	Band gap (eV)	Emission (eV)
30	966	1.28	1.68
60	980	1.26	1.67

5.3.3.3 Morphological properties

Morphological properties of the materials synthesized at various reaction times were analysed by SEM and TEM. TEM and SEM micrographs are illustrated in Fig 5.14 below. The homogenous spherical shaped particles were detected at both high and low reaction time. The spherically shaped particles appear to be fused or attached to each other forming a chain of spheres (inset Fig. 5.14a). The fusion of particles could be due to particles still being trapped in the capping agent or through the oriented attachment mechanism.

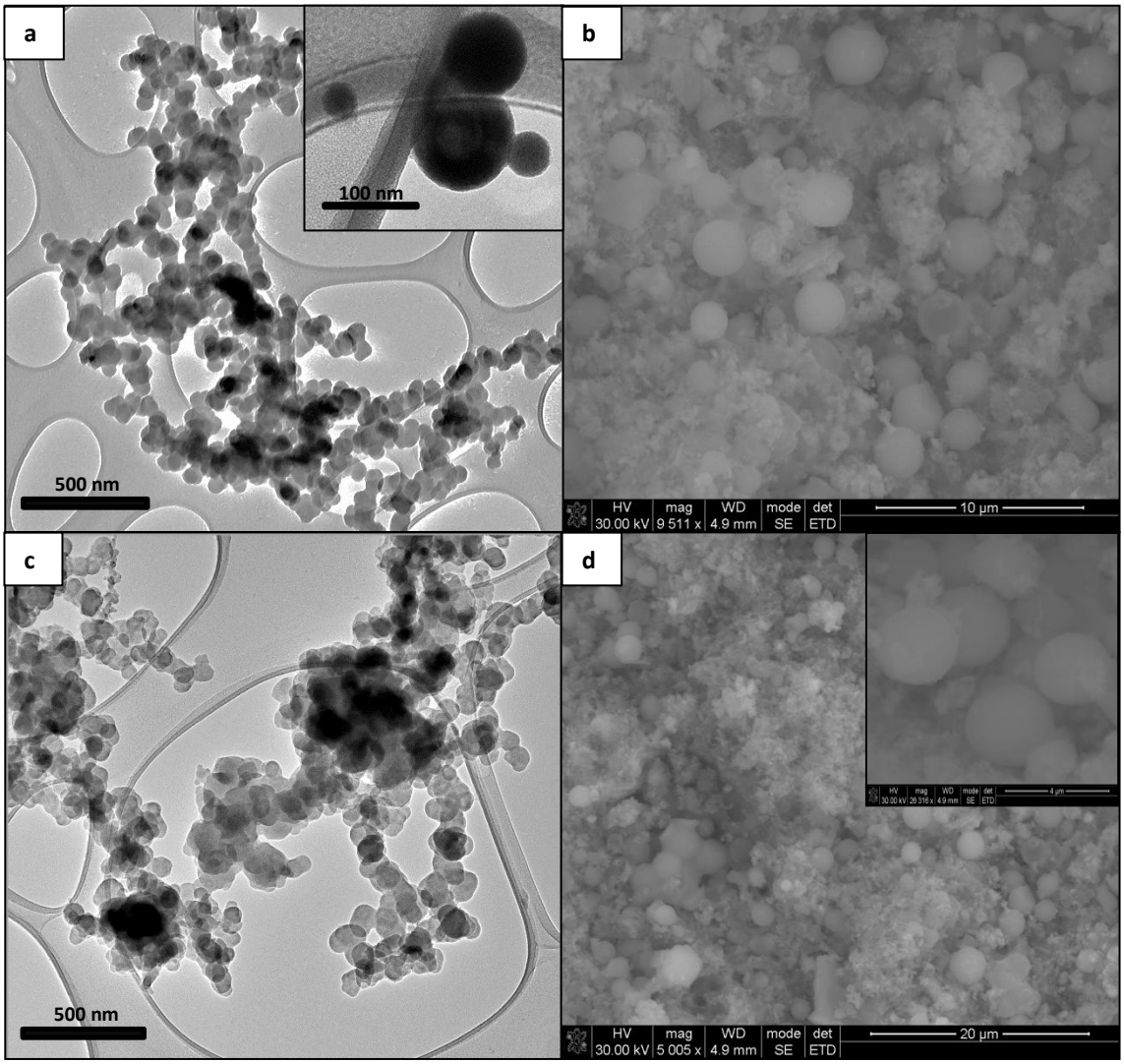


Figure 5.14: TEM and SEM micrographs of $CuIn_{1-x}Ga_xTe_2$ synthesized at reaction time 30 min (a-b) and 60 min (c-d).

We can therefore; attribute formation of black like particles to agglomerated particles. There seems to be no morphology evolution happening with change in reaction time. The spherically shaped particles become bigger with increasing reaction time. The calculated average particle size from the distribution histograms (Fig. 5.15), increased from 45 nm to 60 nm for materials synthesized for 30 and 60 min respectively. Therefore supporting that change in band gap was due to quantum confinement and as a result of Ostwald ripening.

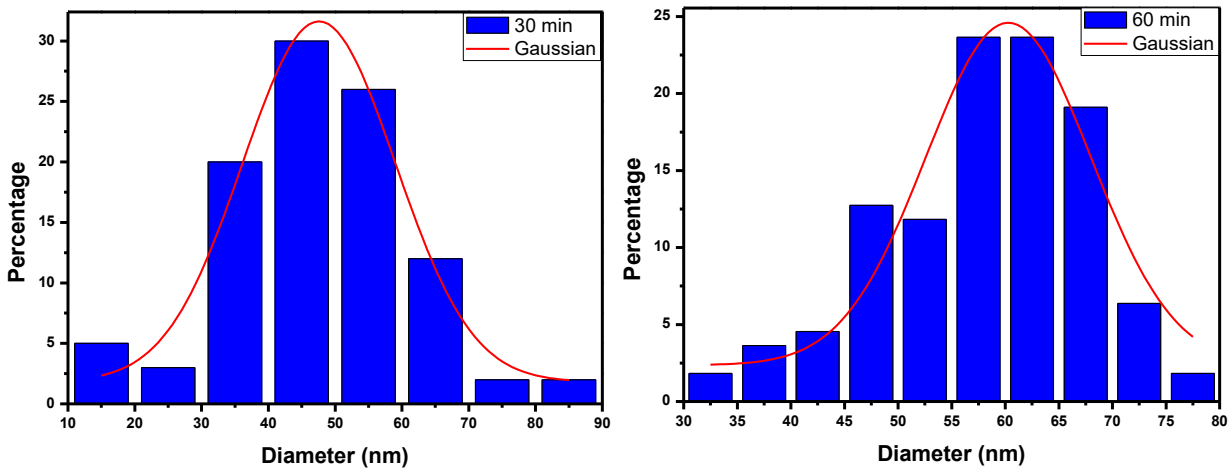


Figure 5.15: Particle size distribution measured from TEM of $CuIn_{1-x}Ga_xTe_2$ synthesized at reaction time 30 min and 60 min.

Elemental analysis of the spherical particles was performed and the spectra are shown in Fig. 5.16. EDS confirmed formation of all elemental constituents of quaternary $CuIn_{1-x}GaTe_2$. From the spectra, In and Ga peak intensity are similar for both particles at 30 and 60 min. This suggests that In to Ga ratios are similar for both particles synthesized at reaction time 30 min and 60 min, this is in good agreement with ICP results. The additional Cu peak at 8 KeV is attributed to the Kα emission line. The O peak suggests that oxidation occurred during synthesis in a partially inert closed system. The detected P is from the TOP solvent used to dissolve Te metal salt.

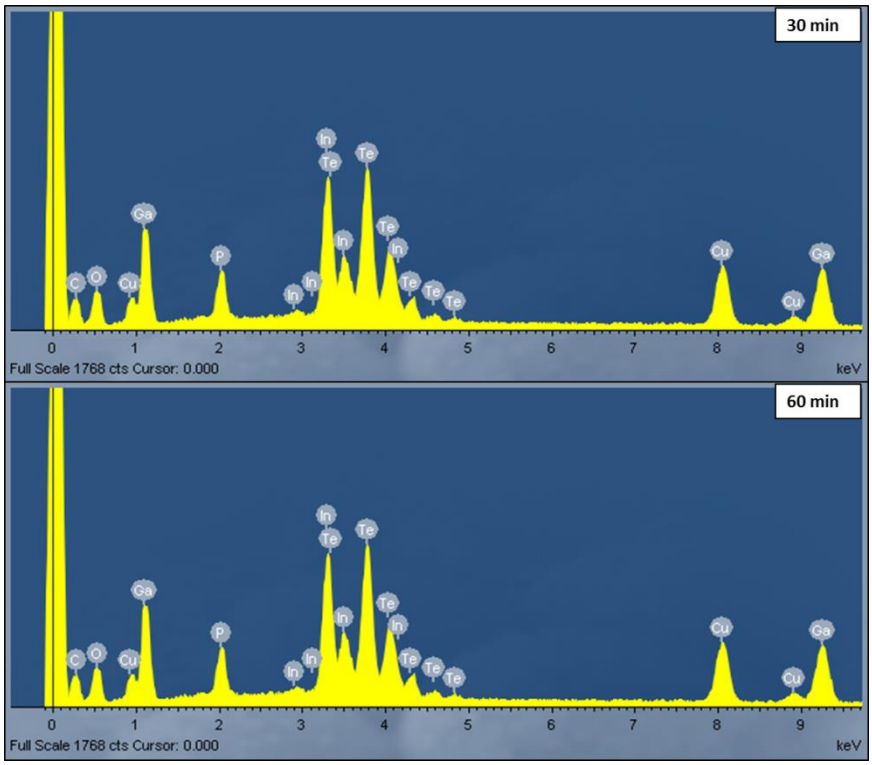


Figure 5.16: EDS spectra of TEM and SEM micrographs of $CuIn_{1-x}Ga_xTe_2$ synthesized at reaction time 30 min and 60 min.

5.3.4 The effect of stoichiometry variation

5.3.4.1 Structural properties

For over decades the birefringence property of ternary chalcopyrites has proven a useful feature as it allowed wide range of optical applications [61]. This was due to the ability of the material's band gap varying with alloy composition [61]. The tailored band gap E_g can be described by equation:

$$E_g(x) = (1-x)\,E_g(CuInTe_2) + xE_g(CuGaTe_2) - bx(1-x) \qquad (5.2)$$

where E_g ($CuInTe_2$) and E_g ($CuGaTe_2$) are the band gaps of the constituents $CuInTe_2$ and $CuGaTe_2$, respectively. The bowing coefficient b which defines the deviation from the linear interpolation and is usually close to a constant for most conventional alloys [61]. Therefore alloying is one of the main means in band-gap engineering to extend the available band-gap

range [61]. Therefore, mixing constituents with chemical mismatch can result in drastically changed physical properties [61]. As such we have also taken interest in exploring the possibility of band gap variation based on composition change of In and Ga. We investigate the crystal structure, morphology and optical properties of $CuIn_{1-x}Ga_xTe_2$. The molar ratio is represented by letter X varying from 0.25, 0.50 and 0.75. The growth time of the nanocrystals was kept at 30 min during synthesis.

Post synthesis, XRD analysis was performed to investigate change in composition and lattice parameters ***a*** and ***c***. Fig. 5.17 shows three similar diffraction patterns, corresponding to a (PDF#: 01-082-0449), (PDF#: 01-082-0448) and (PDF#: 01-082-0447) for a, b and c respectively.

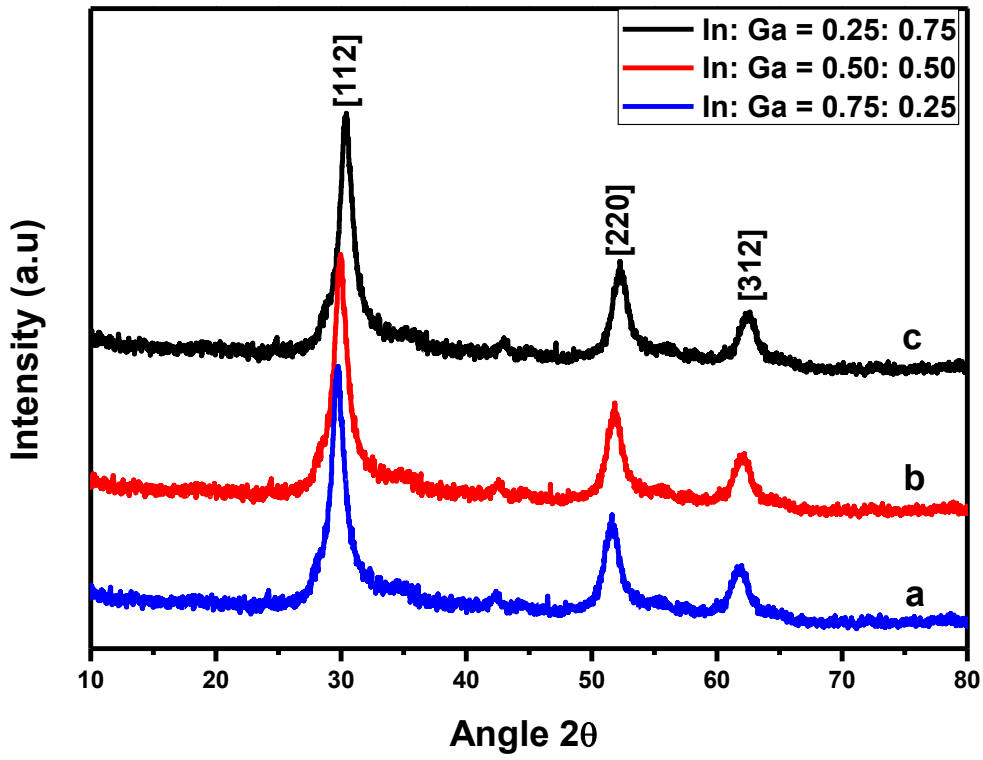


Figure 5.17: XRD patterns of $CuIn_{1-x}Ga_xTe_2$ synthesized from precursor concentrations of In: Ga ratios of (a) 0.75:0.25, (b) 0.50:0.50 and (c) 0.25: 0.75.

The corresponding compositions of the samples according to the JCPD cards are for $CuIn_{0.8}Ga_{0.2}Te_2$, $CuIn_{0.5}Ga_{0.5}Te_2$ and $CuIn_{0.2}Ga_{0.75}Te_2$ for pattern a, b and c (Fig. 5.17) respectively. The three distinguished peaks are indexed to (112), (220) and (320) for quaternary $CuIn_{1-x}Ga_xTe_2$. The (112) peak is the most prominent peak in all the samples indicative of the preferred growth direction. However, there is a slight shift to high 2θ values observed in peak (112) as the x increases. The shift in (112) peak is illustrated in Fig. 5.18. Peak shift to high 2θ values shows change in lattice parameters which could be due to compression or expansion in the unit cell.

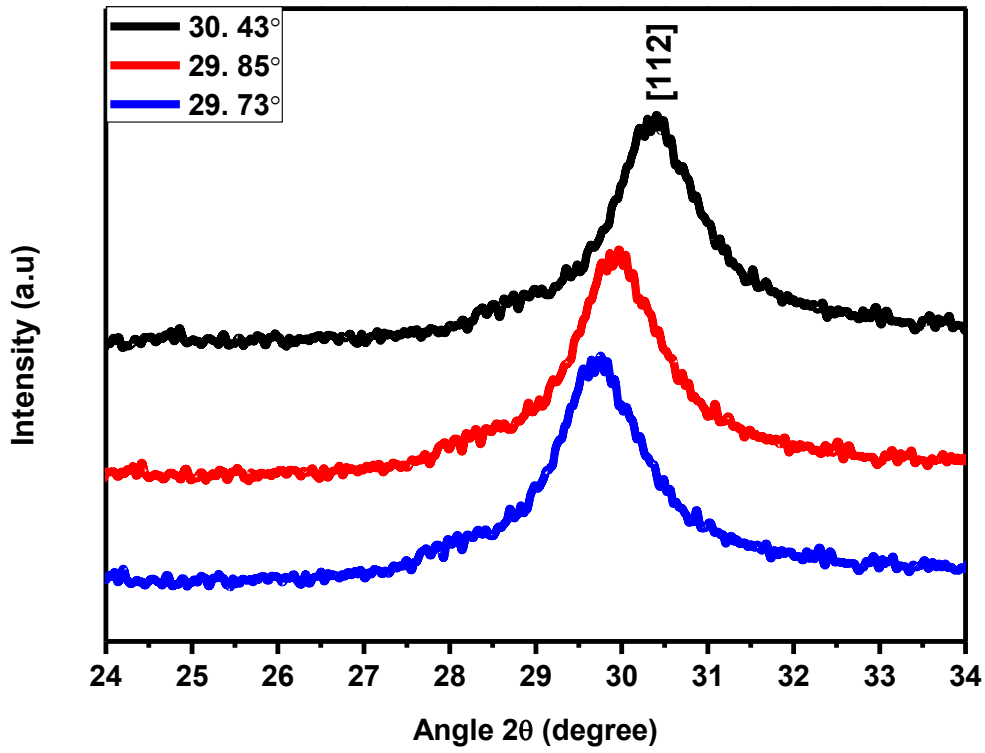


Figure 5.18: (a) XRD patterns showing the expanded view of (111) peak of $CuIn_{1-x}Ga_xTe_2$ synthesized from precursor concentrations of In: Ga ratios of (a) 0.75:0.25, (b) 0.50:0.50 and (c) 0.25: 0.75.

The peak shift to high 2θ values, is indicative of a compression in the unit cell. The compression in the unit cell result from partial substitution of large In atoms with small Ga

atoms. The determined lattice parameters (Table 5.6) show a decrease in lattice parameter *a* and *c* with increasing Ga content which is consistent with compression in the cell. The obtained ***a*** and ***c*** values are in reasonable agreement with the reported values [48]. Furthermore, it was reported by Gabaruci et al. and Grzeta-Plenkovic that the lattice constants in $CuIn_{1-x}Ga_x Te_2$ obey Vergard law which is in agreement with our result [35, 62].

Table 5.6: Lattice parameters and shift in peak position of $CuIn_{1-x}Ga_xTe_2$ with various with various molar ratios of In and Ga

Sample	(112) peak angle 2θ	*a (Å)*	*c (Å)*
$CuIn_{0.8}Ga_{0.2}Te_2$	28.92	6.15[a]	12.30[a]
$CuIn_{0.5}Ga_{0.5}Te_2$	29.42	6.10[b]	12.19[b]
$CuIn_{0.2}Ga_{0.75}Te_2$	29.71	6.05[c]	12.03[c]

a = PDF#: 01-082-0449, b = PDF#: PDF#: 01-082-0448, c = PDF#: 01-082-0447

Further elemental analysis was conducted to confirm atomic percentages. The calculated molar ratios (Table 5.7) of In and Ga were lower than the intended ratios as well as the determined molar ratio from XRD. However, the loss of Ga is greater than that of In which can be attributed to $In(acac)_3$ being more reactive than $Ga(acac)_3$ leading to formation of more In than Ga. Similar trend was reported by Tang and colleagues in the colloidal synthesis $CuIn_{1-x}Ga_xSe_2$ [54]. Therefore reporting that precise composition of ternary and quaternary colloids is only possible when elemental analysis has done, hence most reports of composition in literature are merely estimations. Based on the obtained ICP results, the composition of the synthesized nanoparticles are $CuIn_{0.84}Ga_{0.16}Te_2$, $CuIn_{0.54}Ga_{0.46}Te_2$ and $CuIn_{0.26}Ga_{0.74}Te_2$.

Table 5.7: ICP analysis of $CuIn_{1-x}Ga_xTe_2$ with various molar ratios of In and Ga

In:Ga molar ratio	Cu at%	In at%	Ga at%	Te at%	In:Ga (cal)
0.75: 0.25	28.00	18.39	3.504	50.10	0.84: 0.16
0.50: 0.50	28.14	11.82	10.07	49.98	0.54: 0.46
0.25:0.75	28.09	5.87	16.02	50.02	0.26: 0.74

5.3.4.2 Optical properties

Further analysis was carried out to study the effect of stoichiometry on optical properties. PL and UV-Vis spectra are shown in Fig. 5.19 and 5.20. The optical properties of the synthesized nanocrystals are presented in Table 4.8. From the absorption spectra there is tailing detected in for all materials, suggesting polydispersity in samples. The obtained band edge values are 966, 950, 940 nm for $CuIn_{0.84}Ga_{0.16}Te_2$, $CuIn_{0.54}Ga_{0.46}Te_2$ and $CuIn_{0.26}Ga_{0.74}Te_2$ respectively. The shift to low wavelength in band edge indicates an increase in optical band gap. The corresponding band gap values are 1.28, 1.30 and 1.32 eV for $CuIn_{0.84}Ga_{0.16}Te_2$, $CuIn_{0.54}Ga_{0.46}Te_2$ and $CuIn_{0.26}Ga_{0.74}Te_2$. The band gap is dependent on composition and increases with increasing Ga content. This could also suggest that defect level changes with composition.

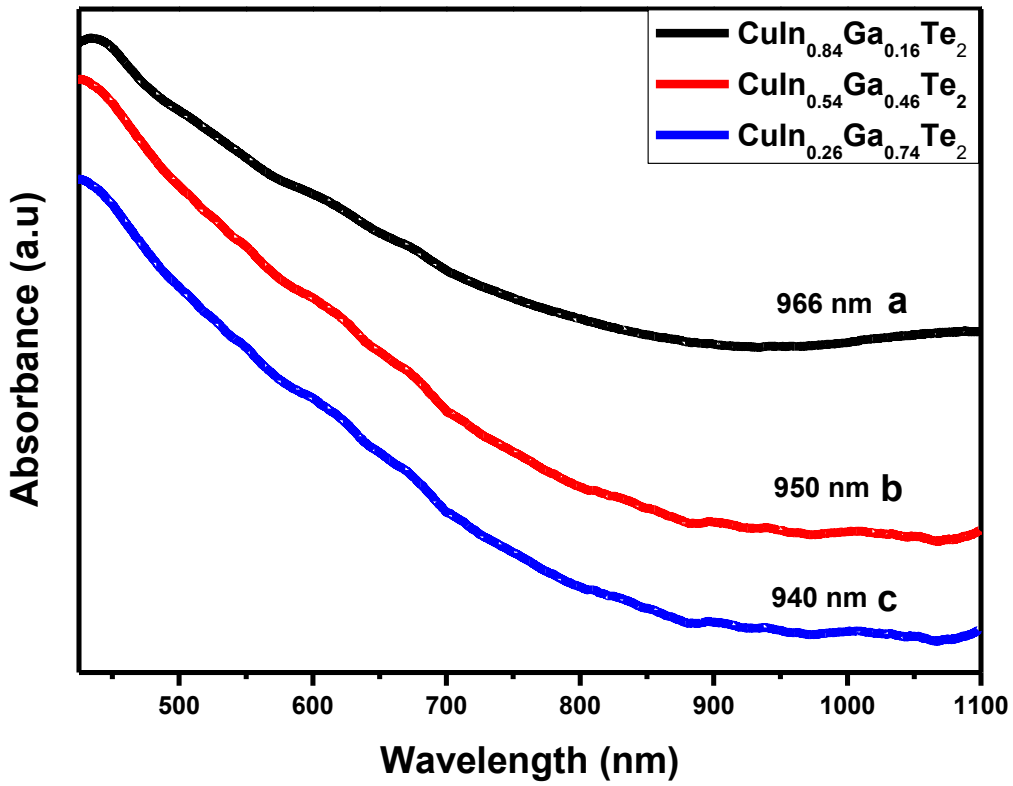


Figure 5.19: UV-Vis absorption spectra of $CuIn_{1-x}Ga_xTe_2$ with precursor concentrations of In: Ga ratios of (a) 0.84:0.16, (b) 0.64:0.48 and (c) 0.28: 0.74 from ICP.

The PL measurements (Fig. 5.20) exhibit increased emission energy upon increasing Ga content. There is a significant increase in emission energy from 1.69 eV to 1.82 eV for $CuIn_{0.84}Ga_{0.16}Te_2$, $CuIn_{0.54}Ga_{0.46}Te_2$. Upon increasing Ga content there is a further increase in emission to 1.87 eV. The detected emissions originate from intrinsic defects as previously indicated. However, the obtained values suggest that high concentration of intrinsic defects occurs when In to Ga molar ratios are equal. There is a deviation in optical band gap and emission energy which can be attributed nano level composition fluctuations which account for variation from bulk properties [60].

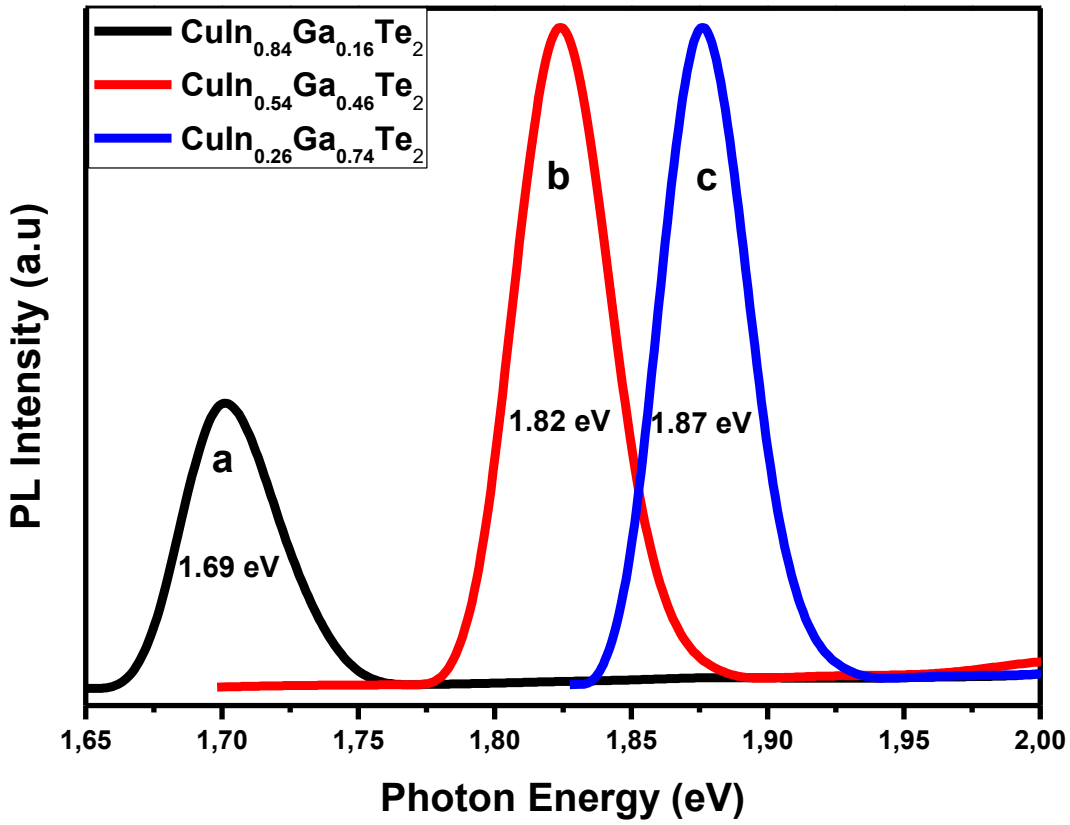


Figure 5.20: PL spectra of $CuIn_{1-x}Ga_xTe_2$ with precursor concentrations of In: Ga ratios of (a) 0.84:0.16, (b) 0.64:0.48 and (c) 0.28: 0.74 from ICP.

Table 5.8: Optical properties of $CuIn_{1-x}Ga_xTe_2$ with various precursor concentrations of In and Ga

Sample	Band edge (nm)	Band gap (eV)	Emission (eV)
$CuIn_{0.84}Ga_{0.16}Te_2$	966	1.28	1.69
$CuIn_{0.54}Ga_{0.46}Te_2$	950	1.30	1.82
$CuIn_{0.26}Ga_{0.74}Te_2$	940	1.32	1.87

5.3.4.3 Morphological properties

Fused spherical shaped particles (Fig. 5.21) were detected for $CuIn_{0.84}Ga_{0.16}Te_2$, $CuIn_{0.54}Ga_{0.46}Te_2$ and $CuIn_{0.26}Ga_{0.74}Te_2$ respectively. The attachment of particles is governed by entropic interaction of large particles due to depletion of small particles in the gap between [63]. It is suspected that if the reaction is prolonged, shape evolution will run to completion. There is a wide particle size distribution with increasing Ga content. The measured particles sizes from TEM are 45, 50 and 60 nm for $CuIn_{0.84}Ga_{0.16}Te_2$, $CuIn_{0.54}Ga_{0.46}Te_2$ and $CuIn_{0.26}Ga_{0.74}Te_2$ respectively.

The EDS spectra (Fig. 5.22) were done to determine the elemental constituents of the quaternary compounds. There is an increase in relative intensity peak of Ga at 9.5 KeV which is consistent with increasing Ga content. On the contrary the relative intensity peak of Cu at 8.0 keV is decreasing with $CuIn_{0.26}Ga_{0.74}Te_2$ the lowest intensity. This could mean that high Ga resulted in Cu deficient materials. Similarly the O and P peaks are also fading except in high Ga content materials. This suggests that there is less impurities in materials with low Ga content.

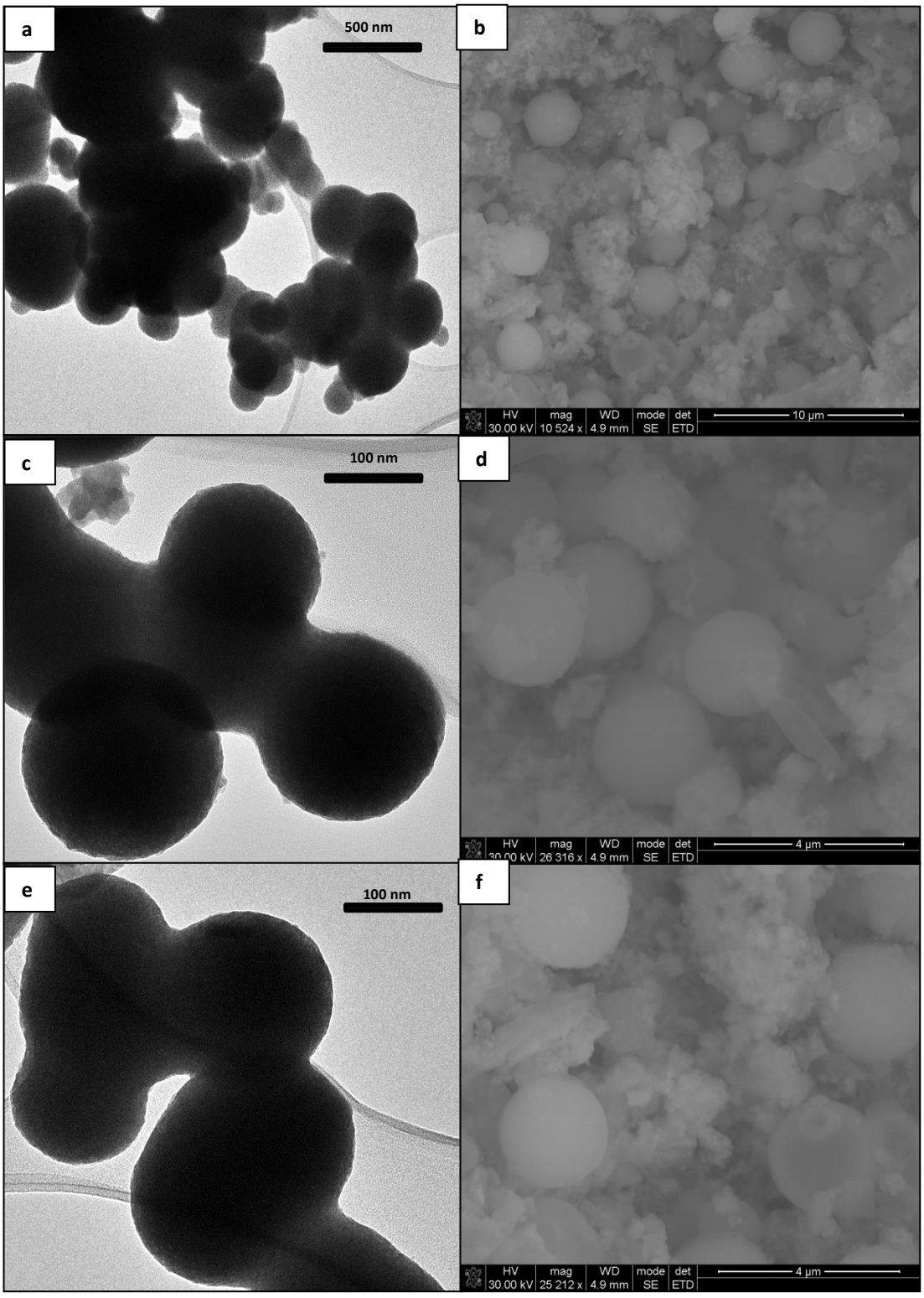


Figure 5.21: TEM and SEM micrographs of $CuIn_{1-x}Ga_xTe_2$ with precursor concentrations of In: Ga ratios of (a-b) 0.84:0.16, (c-d) 0.64:0.48 and (e-f) 0.26: 0.74 from ICP.

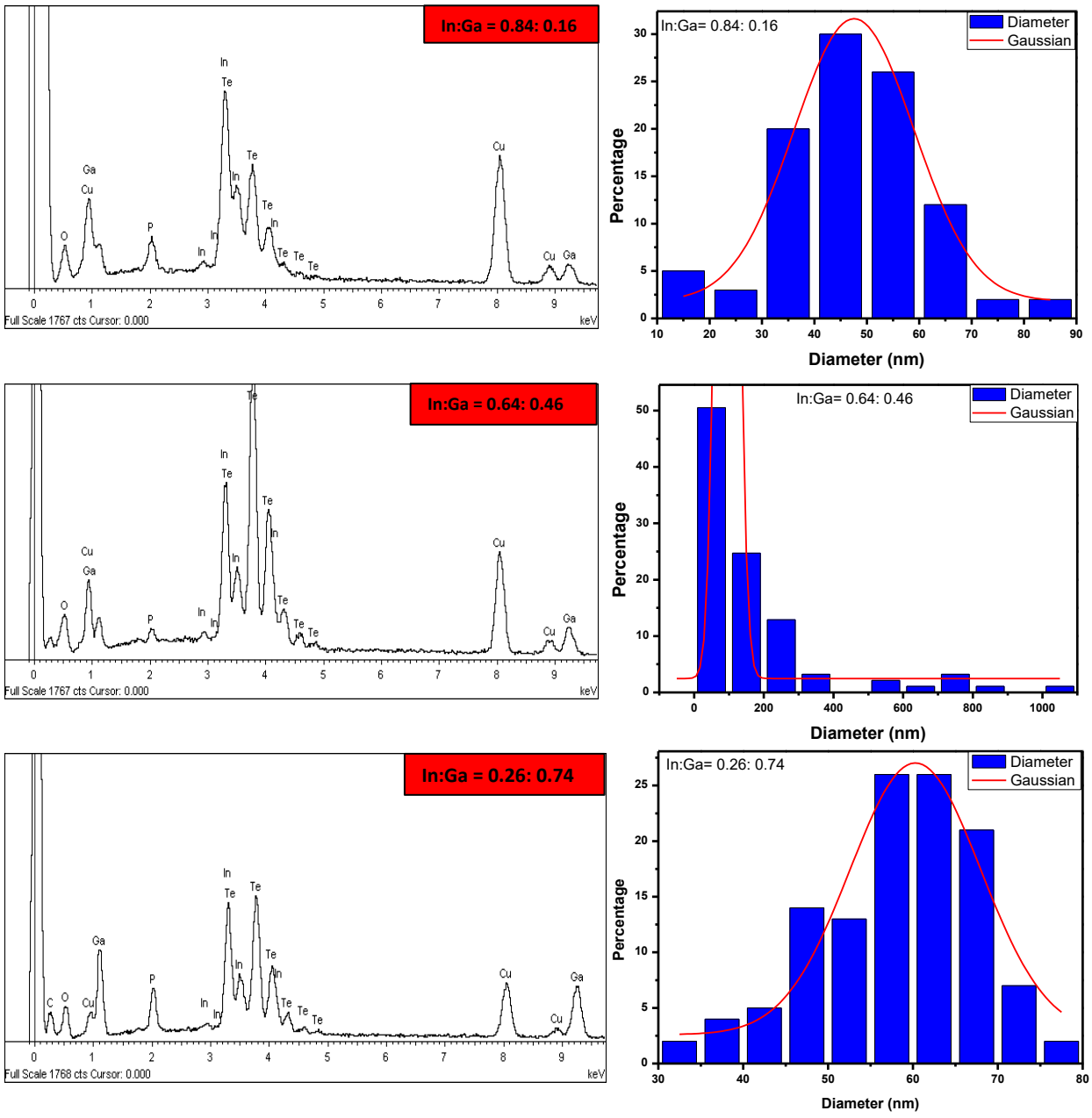


Figure 5.22: EDS spectra of TEM and particle size distribution of $CuIn_{1-x}Ga_xTe_2$ with various concentrations of In: Ga ratios.

5.3.5 The effect of capping agent

5.3.5.1 Structural and morphological properties

The optical properties of colloidal nanocrystals can be tailored by suitably modifying the height, width, and shape of the potential that confines electrons and holes [7]. Control over these parameters is primarily determined by control of nucleation and growth of the nanocrystal. In some instances the use of various surfactants enables control on shape and size. Previously Wang and Li achieved controlled synthesis of a wide range of metals, metal oxides, and bimetallic nanocrystals through the use of octadecylamine (ODA) as a solvent, surfactant, and reducing agent [64]. The use of surfactants is important because of the functional groups present that can coordinate. For example ODA and oleylamine (OLA) display similar basicity and affinity to metals through their NH_2 functional groups and they can produce diverse morphology and crystalline nanoparticles [64].

In the previous section band gap tailoring was achieved through diameter variation by changing reaction times. Herein, we explore diameter and shape control by varying the capping agents. Colloidal quaternary nanocrystals capped with either 1-Dodecanethiol (DDT) or hexadecylamine (HDA) were allowed to growth for a period of 30 min. The molar ratio of In to Ga was kept equivalent with the value of x being 0.50. The XRD measurements were conducted to analyse the effect of solvent on phase composition. The diffraction pattern of quaternary $CuIn_{0.5}Ga_{0.5}Te_2$ particles synthesized in DDT and HDA are presented in Fig. 5.23. The three distinctive $CuIn_{1-x}Ga_xTe_2$ phase peaks were detected for both particles synthesized in DDT and HDA. The DDT particles showed pure crystalline phase while formation of impurities were detected in HDA capped particles. Formation of impurities could suggest that the either reaction was terminated prematurely or higher reaction temperatures are required. However, annealing treatments has been reported to enhance crystallinity. The (220) and

(312) peaks of DDT sample appear at higher 2θ angles compared to HDA capped particles, due to small lattice parameters (Table 5.9).

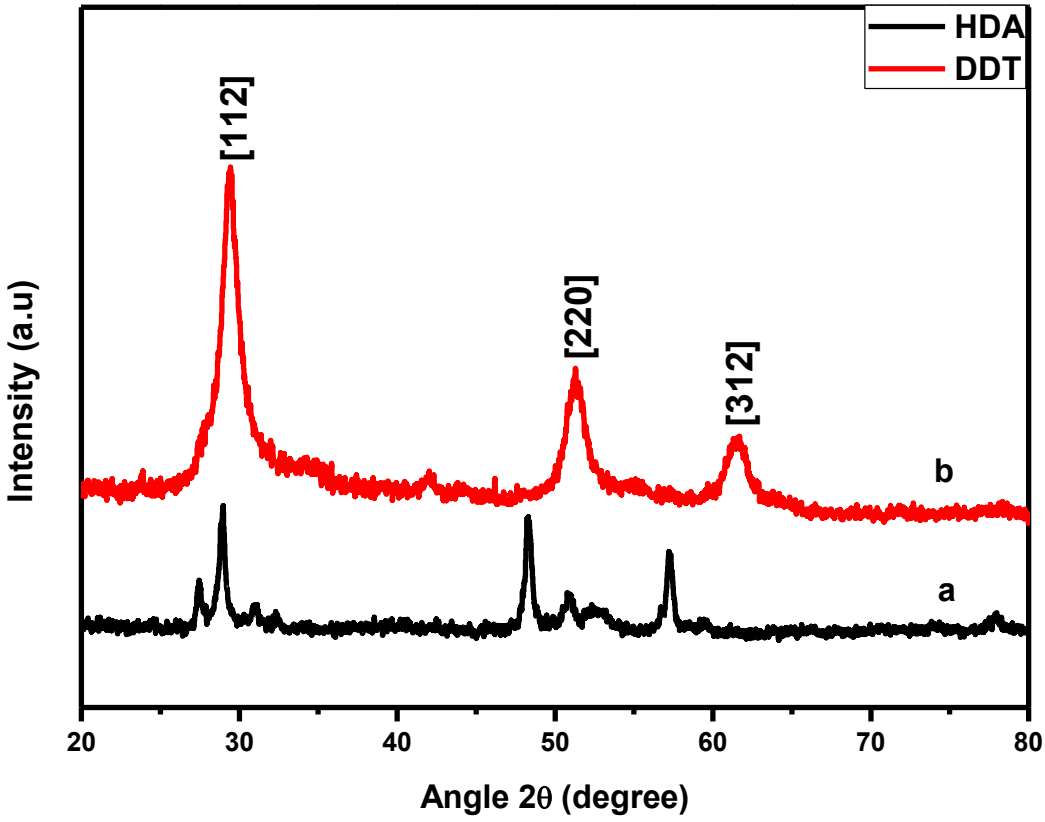


Figure 5.23: (a) XRD patterns of $CuIn_{1-x}Ga_xTe_2$ synthesized from In: Ga ratios of 1:1 in (a) HDA and (b) DDT.

ICP analysis showed (Table 5.10) that the actual molar ratios of In to Ga varied from the intended molar ratios. According to the ICP measurements the quaternary formula could be expressed as $CuIn_{0.57}Ga_{0.43}Te_2$ (HDA) and $CuIn_{0.54}Ga_{0.46}Te_2$ (DDT). There was a decreased observed in actual molar ratios particularly that of the particles synthesized in HDA. This further suggests that there is a weak interaction between HDA and the metal precursor which defies the HSAB principle. In that HDA as hard Lewis base seems to have a weak interaction with Ga^{3+} which is deemed hard Lewis acid. This could partly be due to $In(acac)_3$ being more

reactive than $Ga(acac)_3$. However, more studies need to be conducted to comprehend the reaction mechanism in this case.

Table 5.9: Lattice parameters and shift in peak position of $CuIn_{1-x}Ga_xTe_2$ synthesized in various capping agents

Capping agent	(112) peak angle 2θ	*a (Å)*	*c (Å)*
HDA	29.09	6.13[a]	12.27[a]
DDT	29.42	6.10[b]	12.19[b]

a = PDF#: 01-082-0449, b = PDF#: PDF#: 01-082-0448, c = PDF#: 01-082-0447

Table 5.10: ICP measurements of $CuIn_{1-x}Ga_xTe_2$ synthesized in various capping agents

Capping agent	In:Ga (theo)	Cu at%	In at%	Ga at%	Te at%	In:Ga (cal)
HDA	1:1	28.00	12.48	9.41	50.10	0.57: 0.43
DDT	1:1	28.14	11.82	10.07	49.98	0.54: 0.46

5.3.5.2 Optical properties

Contrary to the established phase composition, the optical properties are not profoundly different. The obtained UV-Vis spectra in Fig. 5.24 show that the absorption band edge of both particles synthesized in HDA and DDT are in the near infrared region. The determined band edge values are 961 and 950 nm corresponding to band gap values of 1.29 and 1.30 eV for HDA and DDT respectively. The measured band gap of particles synthesized in HDA is close to that of the DDT capped particles, suggesting that the particles might have similar morphologies in spite of the impurities present in the HDA sample. The measured emission energy (Fig 5.25) was higher in $CuIn_{0.54}Ga_{0.46}Te_2$ (HDA) with 1.82 eV and lower in

$CuIn_{0.57}Ga_{0.43}Te_2$ (DDT) with the value of 1.80 eV. This emission maximum is blue shifted from the absorption band edges, a common phenomenon in quaternary nanocrystals caused by the heterogeneity of the samples resulting in the introduction of defects.

Table 5.11: Optical properties of $CuIn_{1-x}Ga_xTe_2$ synthesized in various capping agents

Capping agent Sample	Band edge (nm)	Band gap (eV)	Stokes shift (nm)	Emission (eV)
HDA-$CuIn_{0.57}Ga_{0.43}Te_2$	961	1.29	272	1.80
DDT-$CuIn_{0.54}Ga_{0.46}Te_2$	950	1.30	268	1.82

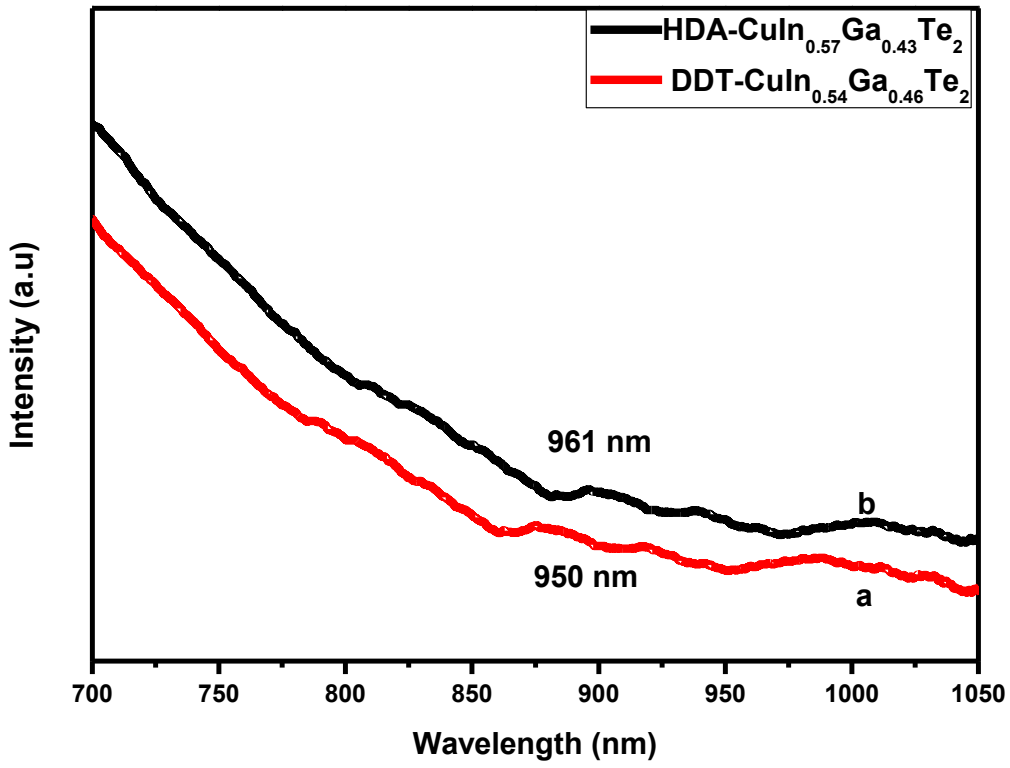


Figure 5.24: UV-Vis absorption spectra of $CuIn_{1-x}Ga_xTe_2$ with In:Ga actual ratios of (a) 0.57:0.43 in HDA and (b) 0.54:0.48 in DDT.

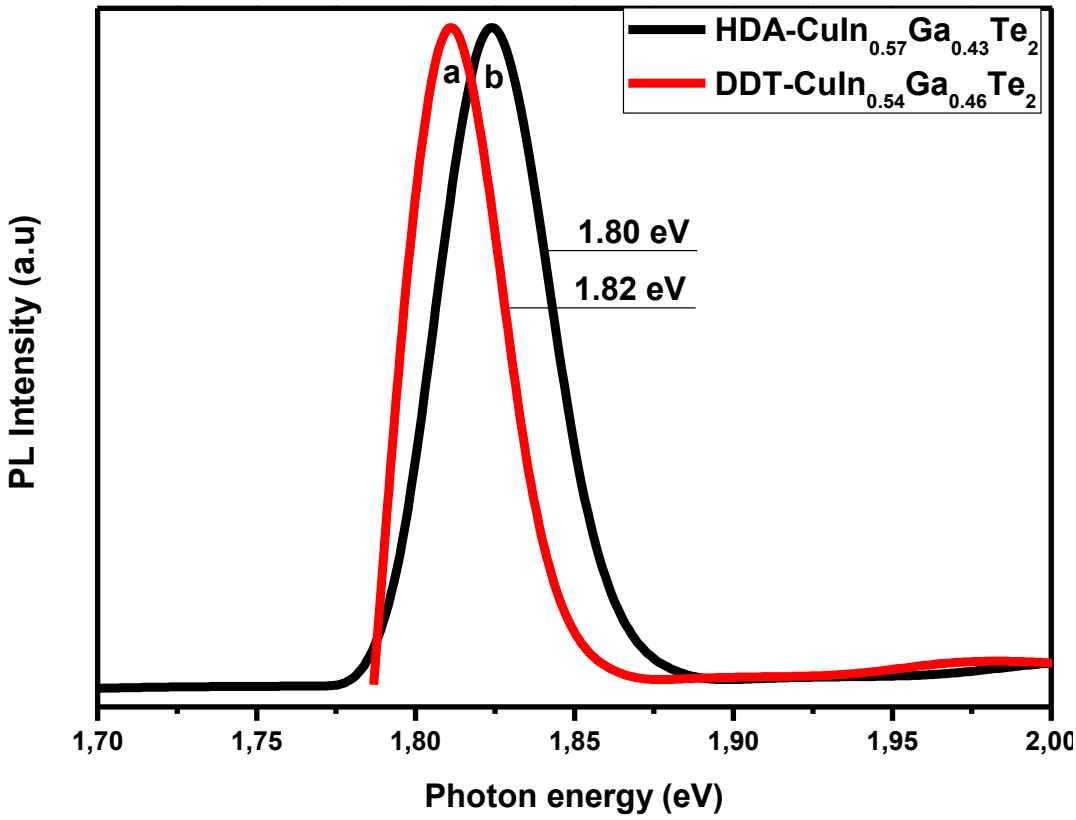


Figure 5.25: PL emission spectra of $CuIn_{1-x}Ga_xTe_2$ with In:Ga actual ratios of (a) 0.57:0.43 in HDA and (b) 0.54:0.48 in DDT.

5.3.5.3 Morphological properties

Spherical shaped particles are seen for both HDA and DDT capped particles as shown in Fig. 26. The HDA capped nanocrystals show similar morphologies as other CIGT materials where large fused spheres are observed. The DDT capped nanocrystals show small particles as well as few large fused spheres. From the TEM (Fig. 5.26c), a large population of spheres that are very small with particle size distribution of 7 nm was observed. This confirms that the attained band gap values were due to quantum confinement. In Fig. 5.26d large truncated shaped particles are observed amongst the large population of small sized particles. This suggest that the sample is not homogeneous hence is in agreement with the observed blue shift in PL.

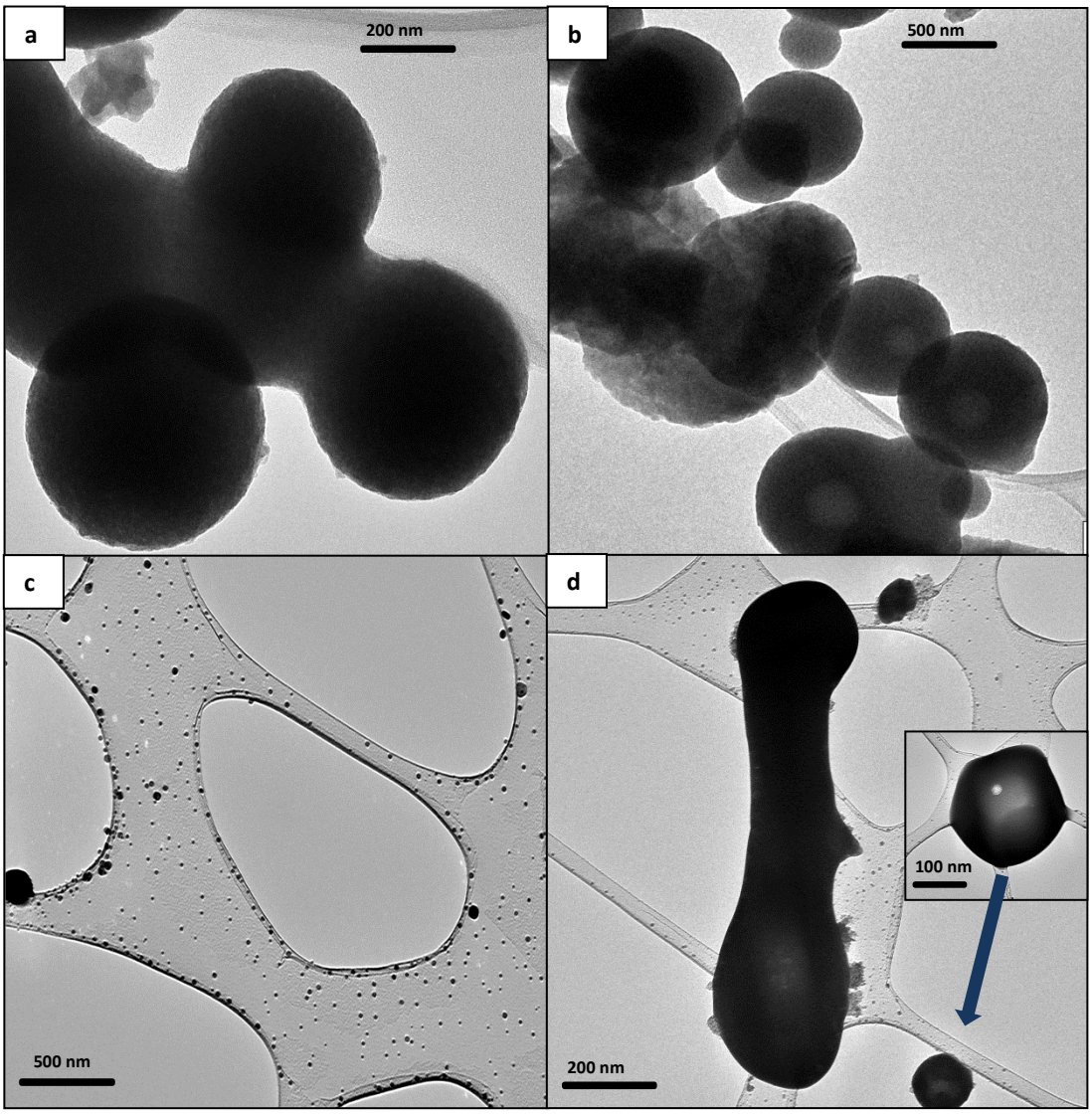


Figure 5.26: TEM micrographs of $CuIn_{1-x}Ga_xTe_2$ with In:Ga actual ratios of (a-b) 0.57:0.43 in HDA and (c-d) 0.54:0.48 in DDT.

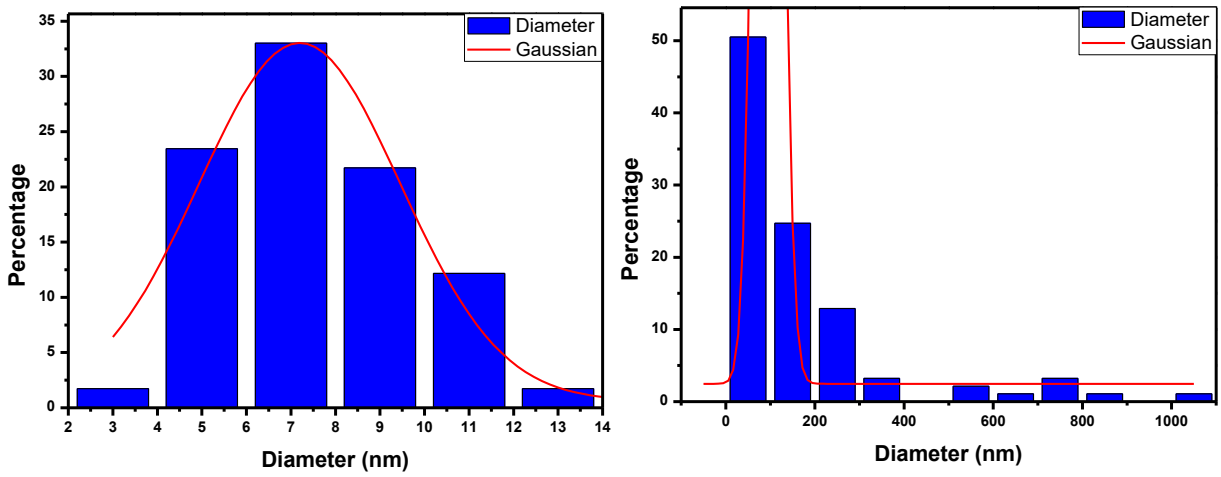


Figure 5.27: Particle size distribution of $CuIn_{1-x}Ga_xTe_2$ with precursor concentrations of In: Ga ratios of .57:0.43 in HDA and 0.54:0.48 in DDT.

5.4 Conclusions

Formation of colloidal quaternary $CuIn_{1-x}Ga_xTe_2$ could be achieved through precursor 1. The quaternary $CuIn_{1-x}Ga_xTe_2$ phase could be distinguished by three diffraction peaks indexed as (112), (220) and (312). The (112) peak was the most prominent peak while high angle peaks had low intensity. High Ga content was attained when precursor 2 was used. High Ga content resulted in a shift to high 2θ angle. Variation in reaction time resulted in a decrease in band gap energy due to wide particle size distribution measured at prolonged reaction time (60 min). Change in molar ratios of In and Ga exhibited change in lattice parameters a and c. Increasing Ga content resulted in a decrease in lattice parameters due to partial substitution of large In atoms with small Ga atoms. Stoichiometry control was challenging as we evidenced a difference with the actual molar ratios being lower than the intended ratios. Lack of stoichiometry control could be attributed to reactivity of the precursor used. For example $GaCl_3$ as a strong acid hydrolysed easily leading to loss in Ga. Furthermore, $In(acac)_3$ is more reactive than $Ga(acac)_3$ which prevents full Ga doping. However, band gap engineering was

attained with change in stoichiometry. The significant band gap increase from 1.69 eV to 1.82 eV for nearly equivalent molar ratios of In and Ga ($CuIn_{0.54}Ga_{0.46}Te_2$) is obatined. There was no morphology evolution observed with change in stoichiometry rather large fused spherical particles were observed from TEM and SEM. Dramatic reduction in particle size was achieved by changing to DDT solvent from HDA.

5.5 References

1. W. Van Der Stam, A. C. Berends and C. de Mello Donega, *ChemPhysChem*, 2016.
2. S. Fiat, P. Koralli, E. Bacaksiz, K. Giannakopoulos, M. Kompitsas, D. Manolakos and G. Çankaya, *Thin Solid Films*, 2013, **545**, 64-70.
3. A. H. Bushra, *Al-Mustansiriyah Journal of Science*, 2011, **22**, 211-221.
4. C. Jiang, W. Liu and D. V. Talapin, *Chemistry of Materials*, 2014, **26**, 4038-4043.
5. Y. Zou, X. Su and J. Jiang, *Journal of the American Chemical Society*, 2013, **135**, 18377-18384.
6. C. Burda, X. Chen, R. Narayanan and M. A. El-Sayed, *Chemical reviews*, 2005, **105**, 1025-1102.
7. A. P. Alivisatos, *The Journal of Physical Chemistry*, 1996, **100**, 13226-13239.
8. J. Avon, K. Yoodee and J. Woolley, *Il Nuovo Cimento D*, 1983, **2**, 1858-1868.
9. P. Grima, M. Quintero, C. Rincón, G. Peres and J. C. Woolley, *Solid state communications*, 1988, **67**, 81-83.
10. J. Boyle, B. McCandless, W. Shafarman and R. Birkmire, *Journal of Applied Physics*, 2014, **115**, 223504.
11. J. Jaffe and A. Zunger, *Physical Review B*, 1984, **29**, 1882.
12. S. H. Wei and A. Zunger, *Journal of Applied Physics*, 1995, **78**, 3846-3856.
13. M. Quintero and J. C. Woolley, *Journal of applied physics*, 1984, **55**, 2825-2829.

14. S.-H. Wei, S. Zhang and A. Zunger, *Applied physics letters*, 1998, **72**, 3199-3201.

15. S. Fiat, P. Koralli, E. Bacaksiz, K. P. Giannakopoulos, M. Kompitsas, D. E. Manolakos and G. Çankaya, *Thin Solid Films*, 2013, **545**, 64-70.

16. K. Subbaramaiah and V. S. Raja, *Materials Letters*, 1994, **20**, 29-33.

17. M.-Y. Chiang, S.-H. Chang, C.-Y. Chen, F.-W. Yuan and H.-Y. Tuan, *The Journal of Physical Chemistry C*, 2011, **115**, 1592-1599.

18. J. E. Bernard and A. Zunger, *Physical Review B*, 1987, **36**, 3199-3228.

19. M. Kaelin, D. Rudmann, F. Kurdesau, H. Zogg, T. Meyer and A. N. Tiwari, *Thin Solid Films*, 2005, **480**, 486-490.

20. W. N. Shafarman and J. Zhu, *Thin Solid Films*, 2000, **361–362**, 473-477.

21. F. O. Adurodija, J. Song, I. O. Asia and K. H. Yoon, *Solar Energy Materials and Solar Cells*, 1999, **58**, 287-297.

22. J. C. Ho, T. Zhang, K. K. Lee, S. K. Batabyal, A. I. Tok and L. H. Wong, *ACS applied materials & interfaces*, 2014, **6**, 6638-6643.

23. M. Wang, S. K. Batabyal, H. M. Lim, Z. Li and Y. M. Lam, *Journal of Alloys and Compounds*, 2015, **618**, 522-526.

24. O. Aissaoui, L. Bechiri, S. Mehdaoui, N. Benslim, M. Benabdeslem, X. Portier, H. Lei, J.-L. Doualan, G. Nouet and A. Otmani, *Thin Solid Films*, 2009, **517**, 2171-2174.

25. M. Wang, S. K. Batabyal, H. M. Lim, Z. Li and Y. M. Lam, *Journal of Alloys and Compounds*, 2015, **618**, 522-526.

26. M. G. Panthani, V. Akhavan, B. Goodfellow, J. P. Schmidtke, L. Dunn, A. Dodabalapur, P. F. Barbara and B. A. Korgel, *Journal of the American Chemical Society*, 2008, **130**, 16770-16777.

27. Q. Guo, G. M. Ford, H. W. Hillhouse and R. Agrawal, *Nano Letters*, 2009, **9**, 3060-3065.

28. A. Pein, M. Baghbanzadeh, T. Rath, W. Haas, E. Maier, H. Amenitsch, F. Hofer, C. O. Kappe and G. Trimmel, *Inorganic chemistry*, 2010, **50**, 193-200.

29. S. L. Castro, S. G. Bailey, R. P. Raffaelle, K. K. Banger and A. F. Hepp, *Chemistry of Materials*, 2003, **15**, 3142-3147.

30. S. N. Malik, S. Mahboob, N. Haider, M. A. Malik and P. O'Brien, *Nanoscale*, 2011, **3**, 5132-5139.

31. Y.-S. Fu and P.-Y. Lin, *CrystEngComm*, 2013, **15**, 1454-1459.

32. W. Yue, S. Han, R. Peng, W. Shen, H. Geng, F. Wu, S. Tao and M. Wang, *Journal of Materials Chemistry*, 2010, **20**, 7570-7578.

33. M. Venkatachalam, M. Kannan, S. Jayakumar, R. Balasundaraprabhu and N. Muthukumarasamy, *Thin Solid Films*, 2008, **516**, 6848-6852.

34. K. Yoshino, H. Yokoyama, K. Maeda and T. Ikari, *Journal of crystal growth*, 2000, **211**, 476-479.

35. D. Gaburici, M. Lazarescu, A. Manea and V. Sandu, *Crystal Research and Technology*, 2000, **35**, 265-270.

36. S. Sugan, K. Baskar and R. Dhanasekaran, *Current Applied Physics*, 2014, **14**, 1416-1420.

37. C. Rincón, S. Wasim, G. Marın, E. Hernández and J. Galibert, *Journal of Physics and Chemistry of Solids*, 2001, **62**, 847-855.

38. C. Rincon and F. Ramirez, *Journal of applied physics*, 1992, **72**, 4321-4324.

39. D. Sridevi and K. Reddy, *Thin Solid Films*, 1986, **141**, 157-164.

40. Y. Aparna, P. S. Reddy, B. S. Naidu and P. J. Reddy, *physica status solidi (a)*, 1991, **125**, K39-K42.

41. F. B. Dejene, *Advances in Materials Science and Engineering*, 2014, **2014**, 6.

42. J. H. Boyle, B. E. McCandless, W. N. Shafarman and R. W. Birkmire, *Journal of Applied Physics*, 2014, **115**, 223504.

43. M. Yarema, R. Caputo and M. V. Kovalenko, *Nanoscale*, 2013, **5**, 8398-8410.

44. J. van Embden, A. S. Chesman and J. J. Jasieniak, *Chemistry of Materials*, 2015, **27**, 2246-2285.

45. R. G. Pearson, *Journal of the American Chemical Society*, 1963, **85**, 3533-3539.

46. R. G. Pearson, *J. chem. Educ*, 1968, **45**, 581.

47. Y. Yin and A. P. Alivisatos, *Nature*, 2005, **437**, 664-670.

48. O. Aissaoui, S. Mehdaoui, L. Bechiri, M. Benabdeslem, N. Benslim, A. Amara, A. Otmani, K. Djessas and X. Portier, *Journal of Luminescence*, 2011, **131**, 109-113.

49. A. Shaukat, *Journal of Physics and Chemistry of Solids*, 1990, **51**, 1413-1418.

50. J. Krustok, M. Grossberg, A. Jagomägi, M. Danilson and J. Raudoja, *Thin solid films*, 2007, **515**, 6192-6195.

51. U. Fano, *Physical Review*, 1961, **124**, 1866-1878.

52. M. Thwaites, R. Tomlinson and M. Hampshire, *physica status solidi (b)*, 1979, **94**, 211-214.

53. Y. Xia, X. Xia and H.-C. Peng, *Journal of the American Chemical Society*, 2015, **137**, 7947-7966.

54. J. Tang, S. Hinds, S. O. Kelley and E. H. Sargent, *Chemistry of Materials*, 2008, **20**, 6906-6910.

55. J. Hu, L.-s. Li, W. Yang, L. Manna, L.-w. Wang and A. P. Alivisatos, *Science*, 2001, **292**, 2060-2063.

56. Y. Yan, R. Noufi, K. Jones, K. Ramanathan, M. Al-Jassim and B. Stanbery, *Applied Physics Letters*, 2005, **87**, 121904.

57. M. J. Romero, K. Ramanathan, M. A. Contreras, M. M. Al-Jassim, R. Noufi and P. Sheldon, *Applied physics letters*, 2003, **83**, 4770-4772.

58. L. Gütay, C. Lienau and G. H. Bauer, *Applied Physics Letters*, 2010, **97**, 052110.

59. J. T. Heath, J. D. Cohen, W. N. Shafarman, D. Liao and A. Rockett, *Applied Physics Letters*, 2002, **80**, 4540-4542.

60. I. Repins, L. Mansfield, A. Kanevce, S. A. Jensen, D. Kuciauskas, S. Glynn, T. Barnes, W. Metzger, J. Burst and C.-S. Jiang, *Wild Band Edges: The Role of Bandgap Grading and Band-Edge Fluctuations in High-Efficiency Chalcogenide Devices: Preprint*, NREL (National Renewable Energy Laboratory (NREL), Golden, CO (United States)), 2016.

61. T. Tinoco, M. Quintero and C. Rincón, *Physical Review B*, 1991, **44**, 1613.

62. B. Grzeta-Plenkovic and B. Santic, *Journal of Applied Crystallography*, 1983, **16**, 576.

63. G. M. Rodríguez-Liñán, Y. Nahmad-Molinari and G. Pérez-Ángel, *PloS one*, 2016, **11**, e0156153.

64. L. Brus, *Applied Physics A: Materials Science & Processing*, 1991, **53**, 465-474.

Chapter 6: Heterojunction ZnO/CIT and ZnO/CIGT solar cells

6.1 Introduction

Third generation solar cells were developed to circumvent high production costs of silicon-based solar technology [1]. Escalated production costs in silicon-based solar cells were mainly due to rigorous requirements for materials and processing [1]. However, thin film photovoltaic devices have proven to be advantageous over the conventional silicon wafer based devices [1]. Production of these devices require minute thicknesses of the absorbance layer [1]. The devices can be manufactured by a variety of deposition methods such as co-evaporation, sputtering and printing on various types of substrates such as Mo-coated or transparent conducting oxide on glasses [2-3]. The recorded efficiency of 21.7% has been reported for the polycrystalline chalcopyrite $Cu(In,Ga)(Se,S)_2$ (CIGS) solar cells [1]. In addition the devices are highly stable, durable and lack toxic metals making them the most promising thin-film technology [4]. The required vacuum based techniques in achieving high quality CIGS films means that fabrication costs are still an obstacle [1].

Alternatively non-vacuum deposition techniques were developed. A variety of solution-processed approaches such as electro-chemical deposition, spray pyrolysis, blade coating, printing and spin coating have been employed [5-8]. A power conversion efficiency of 15.2% which is close to that of the vacuum fabricated devices (21.7%) has been reported by Mitzi and co-workers [9]. The devices were fabricated via hydrazine solution processing, in which the hydrazine complex was used to dissolve binary compounds which were Cu_2S, In_2Se_3 and Ga_2Se_3. S and Se were also added [10]. The introduction of the elemental compounds in the form of chalcogenides aided in avoiding the formation of undesired impurities such as C, O, Cl which are detrimental to the device performance [1]. The hydrazine forms

metal−chalcogenide networks, in which metal chalcogenide anions are separated by hydrazinium cations ($N_2H_5^+$) [1]. This creates a stable and homogeneous transparent precursor solution [1]. The weakly bound hydrazine is removed through decomposition by thermal treatment. Moreover, thermal treatments are said to be beneficial for enhanced electrical properties [1]. They result in structural rearrangement which eliminates defects that decreases the carrier charge concentration and hence resistivity and capacitance [11]. In bulk $CISe_2$, thermal treatment resulted in the increased Se content, therefore shifting the photoluminescence (PL) band maximum to higher values of energy [12, 13].

Despite the facile Ga doping through the hydrazine solution processing, the method still lacks fine tuning of Ga composition grading [1]. For example, in vacuum based processing, Ga grading is easily achieved through a multiple stage process by carefully monitoring deposition parameters [14]. High Ga content is necessary as it pushes the electrons away from the Mo back contact and prevents recombination [15]. The front Ga grading controls the separation and collection of photo-generated charge carriers and enhances the open circuit voltage [16]. The off stoichiometry of the film composition which results in segregation of secondary phases during the growth process may have a negative impact on the performance of the device [17].

To achieve stoichiometry control in non-vacuum techniques, the absorber layer can be separately synthesized prior deposition onto the substrate. Many synthetic approaches for obtaining high quality nanocrystal absorbing layers have been employed [18]. Amongst the adopted methods, the vapour and solid phase have fallen short due to instrumental and precursor limitations [18]. The liquid phase approach proved to be efficient for fine control synthesis of high quality nanostructured absorbing layers [18]. Moreover, the stable

suspensions offer an advantage for direct application in solution techniques such as spin-coating, inkjet printing, and roll to-roll casting [19]. While much of the work has been conducted on $CuInS/Se_2$ and $Cu(In.Ga)S/Se_2$ thin film solar cells, less work has been carried out on the $CuInTe_2$ (CIT) and $CuIn_{1-x}Ga_xTe_2$ (CIGT) thin films [20]. It has been reported that obtaining single crystals of good quality with tellurides through vacuum deposition is challenging making them less desirable [21]. Aissaoui and colleagues reported the near stoichiometric polycrystalline $CuIn_{1-x}Ga_xTe_2$ bulk films [20]. The flash evaporated $CuIn_{1-x}Ga_xTe_2$ thin films demonstrated that variation in Ga content allowed the achievement of the absorber layer with large gaps [22]. There are however, few reports on the solution fabrication of $CuIn_{1-x}Ga_xTe_2$.

There are many solar cell designs based on semiconductor nanocrystals. The Schottky junction solar cells have in particular attracted a lot of attention due to their ease of fabrication however they have a number of limitations [23]. While large short circuit currents (Jsc) of over 20 mA/cm^2 can be achieved, the open circuit voltage (Voc) is low compared to the band gap energy. The maximum Voc obtainable in Schottky geometry is limited to Eg/2q, where q is the charge of an electron. The low Vocs typically reported are attributed to Fermi-level pinning at the metal/semiconductor junction. Because the Schottky junction forms at the back electrode opposite from where light is shone, minority carriers (electrons) recombine or are trapped at defect sites before they reach the negative electrode [24].

To overcome the above limitations, a heterojunction solar cell with a transparent n-type metal oxide layer and a p-type PbS QD layer has been reported. In this type of device, minority carriers flow toward the metal oxide while holes are extracted at the high work function back contact. In this structure, the Voc is determined by the difference in the quasi-Fermi levels in

the PbS QD and ZnO layers [25]. Herein, we report on the fabrication of ZnO/ CIT and CIGT solar cell devices through a simple solution process. The effect of chemical surface treatment through ligand exchange on the device performance was studied. The influence of the annealing treatment on the photovoltaic properties of the device was also be explored.

6.2 Experimental

6.2.1 Materials

Acetone, isopropanol, toluene, acetonitrile, zinc acetate, 2-methoxyethanol, ethanol amine and ethanedithiol (EDT), lithium perchlorate ($LiClO_4$), tin doped-indium oxide (ITO) glass substrate were all purchased from Sigma-Aldrich.

6.2.2 Fabrication of the hybrid solar cells

The structure of the devices consisted of the following layers of films: ITO/ZnO/CIT or CIGT/Au. The substrates were routinely cleaned by sequential ultrasonication in acetone, isopropanol, and de-ionized water and then dried in air for 20 min. The ZnO layer was synthesized using a sol-gel method. About 2 g of zinc acetate, 20 mL of 2-methoxyethanol and 568 µL of ethanol amine were mixed together and sonicated for 30 min. About 2-3 drops of the syringe filtered sol-gel solution was spin-coated onto an ITO substrate at 3000 rpm and annealed at 200 °C for 30 min. This procedure was repeated. About a drop of 30 mg/mL of the CIT/CIGT nanoparticles dissolved in toluene was spin-coated on top of the ZnO layer, followed by a drop of toluene. This was allowed to stand for 20 sec. The process was repeated 15 times to build a thin film of approximately 100 nm. For the EDT a treated thin film, about 5 drops of 2% EDT acetonitrile solution was added after the nanoparticle solution, followed by cleaning with acetonitrile and toluene. This was also done 15 times. The top Au

contacts were sputtered through a shadow mask to generate an array of patterned electrodes. The Au was deposited by thermal evaporation in high vacuum of better than 5×10^{-5} Pa at a rate of about 0.2 nm/s. The final area of each device was 1 cm^2 and was defined by the overlap between the top ITO and bottom Au electrode. For annealing, the devices were annealed in air at 300, 400 and 500 °C.

6.2.3 Characterization

For the characterization of ZnO nanoparticles, a Varian Cary Eclipse (Cary 50) UV-VIS spectrophotometer was used to carry out the absorption measurements and a Varian Cary Eclipse EL04103870 fluorescence spectrophotometer with a medium PMT voltage at an excitation wavelength of 200 nm was used to measure the photoluminescence (PL) of the samples. For both spectral analyses, the scraped powders were dissolved in water and placed in quartz cuvettes (1cm path length). The film absorbance was determined on UV-Visible spectroscopy (Analytik-Jena SPECORD 50). The surface morphology of the thin films was analyzed through by scanning electron microscopy (SEM). The SEM images were recorded using FEI Nova Nanolab 600 microscope. Electrochemical measurements were performed in a CHI 660B electrochemical work station (CH Instruments Inc., USA), equipped with a conventional one-compartment three-electrode cell. A glassy carbon (GC) electrode with an active area of 0.07 cm^2 was used as a working electrode, a silver/silver chloride electrode (Ag/AgCl) was employed as a reference electrode and a platinum coil was adopted as a counter electrode. The CIGT particles were dispersed in toluene and drop casted on the glassy carbon electrode. All the measurements were carried out in a N_2-saturated acetonitrile solution containing 0.1 M lithium perchlorate ($LiClO_4$), and the scan rate was 50 mV/s. The device performances were characterized under AM1.5G 100 mW/cm^2 illumination in a laminar flow cabinet.

6.3 Results and discussion

6.3.1 Optical properties of sol-gel ZnO thin films

The ZnO in heterojunction solar cells acts an n-type layer. It has a double function where it acts as an electron transporting layer as well as a hole blocking layer. Herein, ZnO is synthesized via a simple, well known sol-gel method where a gel is formed at room temperature and spin-coated onto the ITO substrate. The substrate is then heated at 200 °C to form the desired ZnO as shown in Fig. 6.1 (R is ethanol amine) [50].

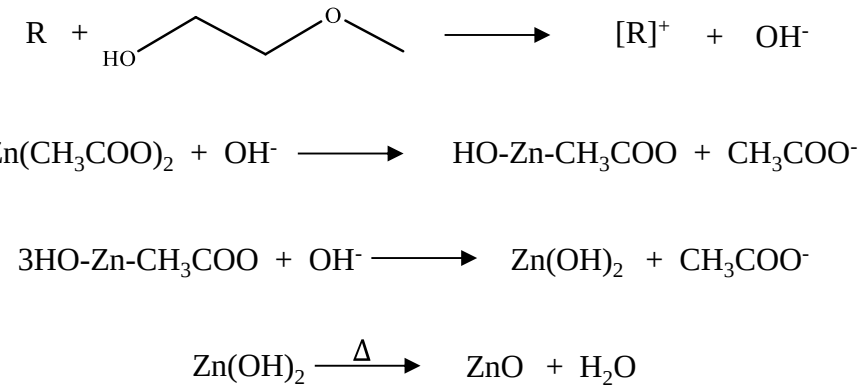


Figure 6.1: Scheme of Synthesis of ZnO via the sol-gel method.

To ascertain that the ZnO layer was indeed formed, the optical studies were performed. Fig. 6.2 shows the absorption and photoluminescence (PL) spectra of the synthesized ZnO. The band edge is located at 349 nm corresponding to an optical band gap of 3.55 eV which is slightly blue-shifted from the bulk band gap of 3.37 eV. This suggests that the particle sizes are small and they experience quantum confinement. The PL emission maximum is located at 375 nm, depicting a slight red-shift from the absorption band edge. The near band edge emission suggests that there are few defects hence fewer traps in the ZnO. This is desirable for solar cells.

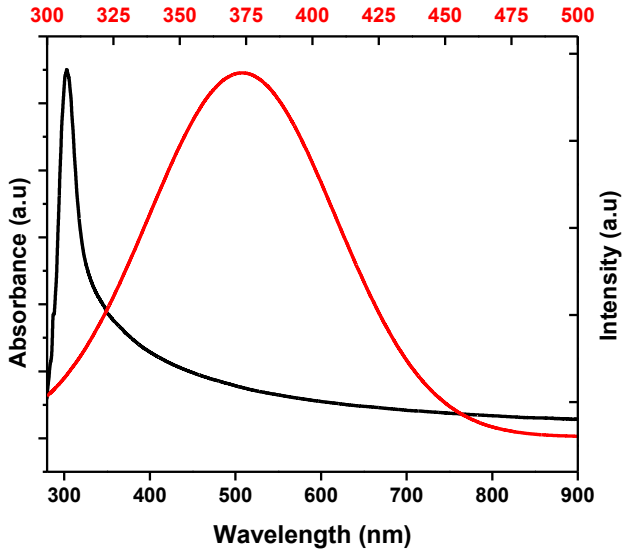


Figure 6.2: UV-Vis absorption and photoluminescence spectra of ZnO.

6.3.2 Cyclic voltammetry measurements

In order to fulfil the energy requirements of the device, knowledge of electronic energy levels is essential [23]. This is due to the fact that electron transfer from the donor to the acceptor requires that the lowest unoccupied molecular orbital (LUMO) level of the donor be above that of the acceptor [23]. The highest occupied molecular orbital (HOMO) level be above that of the acceptor for hole transfer [23]. The electrochemical process is said to be an effective approach for evaluating the position of the HOMO and LUMO energy levels and the optical band gap of films because it entails charge injection and transportation [23]. The oxidation process in cyclic voltammetry measurements provides information about the energy needed to extract an electron from the HOMO energy level, while reduction process determines the energy required to inject an electron on the LUMO [24]. The electron transfer between the energy level of the working electrode and the molecular energy levels of the materials generates current. The recorded cyclic voltammogram of the $CIGTe_2$ material is illustrated in Fig. 6.3.

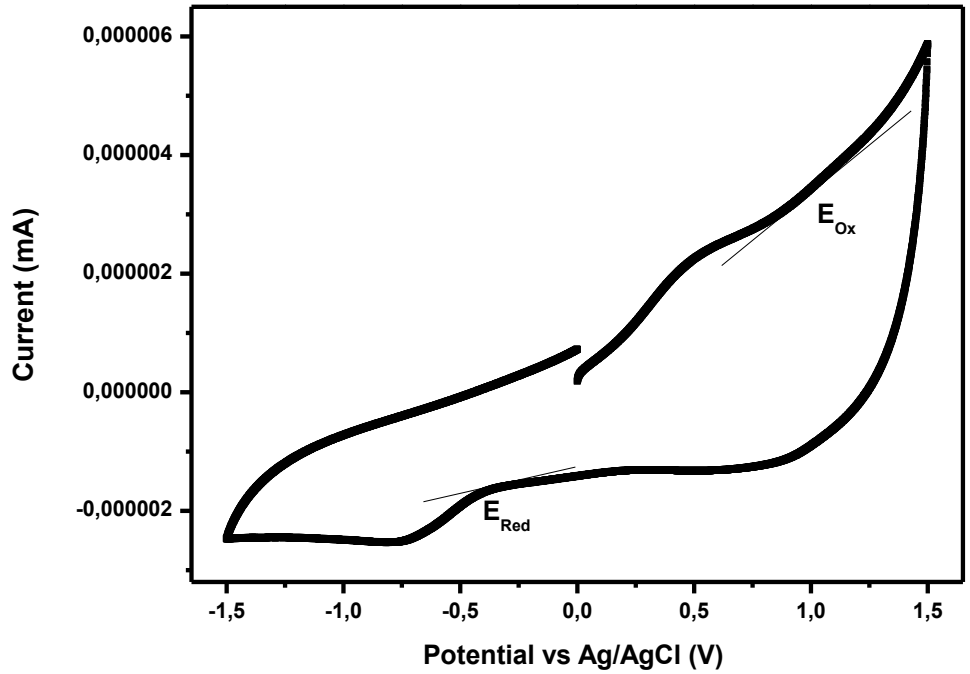


Figure 6.3: Cyclic voltammogram of HDA capped $CuIn_{0.25}Ga_{0.75}Te_2$ synthesized using precursor 2.

The $CIGTe_2$ particles were dispersed in toluene and added dropwise on the glassy carbon (GC) electrode. Cyclic voltammetry measurements of the $CIGTe_2$ particles were recorded at the scan rate 50 mVs^{-1} by immersing GC electrode in an electrolyte solution of N_2-saturated acetonitrile containing 0.1 M lithium perchlorate ($LiClO_4$). The onset potentials of oxidation and reduction of a material are determined from the intersection of the two tangents. The energy levels were calculated using empirical equations (6.1) and (6.2) which uses ferrocene as a known reference with the value of -4.4 eV.

$$E\ (HOMO) = -E_{ox}^{onset} - 4.4 \quad (6.1)$$

$$E\ (LUMO) = -E_{red}^{onset} - 4.4 \quad (6.2)$$

The onset potential for oxidation of the material is observed at 1.06 eV while the reduction potential is at -0.33 eV. The resulting HUMO and LUMO values are -5.46 eV and -4.07 eV respectively. The calculated electrochemical band gap is 1.39 eV which is higher than the

band gap range (0.96-1.35 eV) of bulk material [22]. The attained band gap seems to be 0.9 eV higher than the measured optical band from UV-Vis-NIR. Other authors attributed the variation in band gap to the resulting binding energies of excitons generated in both optical and electrochemical environment which are different [25]. The influence of the stabilizing ligands on the charge injection process between the nanocrystals and the working electrode in CV measurements could also be a contributing factor. The CV measurement for the CIT particles was not reported as no clear reduction peak was obtained.

6.3.3 Photovoltaic properties of CIT solar cell device

A solar cell is characterized by a current versus voltage measurement. This results in a curve shown in Fig. 6.4. From this graph a few important performance parameters can be extracted, mainly the open circuit voltage (V_{OC}), short circuit current (J_{SC}), fill factor (FF), and maximum power (Pmax). The open circuit voltage is the voltage the cell produces when no current is flowing and represents the maximum voltage of the cell. The short circuit current is the current the cell can produce when the two electrodes are shorted together (i.e. V = 0).

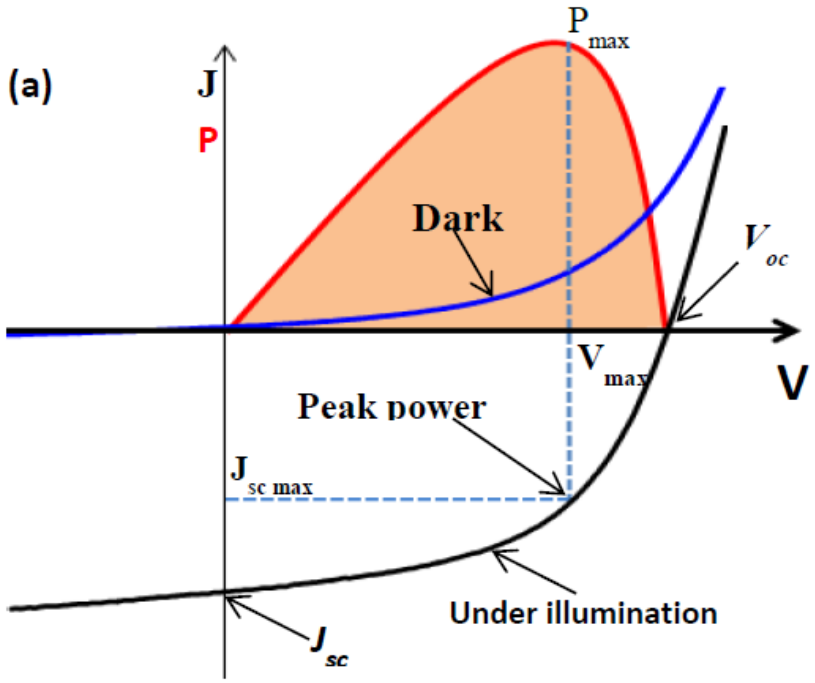


Figure 6.4: I-V curve showing the important parameters.

Because power is the product of voltage and current, the point on the graph that forms the largest rectangle with the two axes represents the point of maximum power output. The fill factor can be calculated from the ratio of the actual maximum power to the ideal maximum power, that is:

$$FF = \frac{J_{max}V_{max}}{J_{sc}V_{oc}} \qquad (6.3)$$

The power conversion efficiency is therefore the quotient of the maximum power output over the power of the incident light:

$$\eta = \frac{P_{max}}{P_{in}} = \frac{J_{sc}V_{oc}FF}{P_{in}} \qquad (6.4)$$

The solar cell devices were fabricated through a simple solution process. Once the devices were fabricated, the photovoltaic measurement of the CIT solar cell device was conducted. The schematic solar cell structure showing the inverted heterojunction solar cell with an n-

type ZnO and a p-type CIT/CIGT is shown in Fig 6.5 (a). Fig. 6.5 (b) shows a schematic of the equilibrium band diagram. Photogenerated minority carriers in the CIT/CIGT layer can either be swept into the ZnO layer and transported to the anode or swept into the back metal cathode, thus leading to opposing currents. Holes are majority carriers and, therefore, should be extracted at the metal cathode but experience a hole-injection barrier at both the ZnO and metal interfaces.

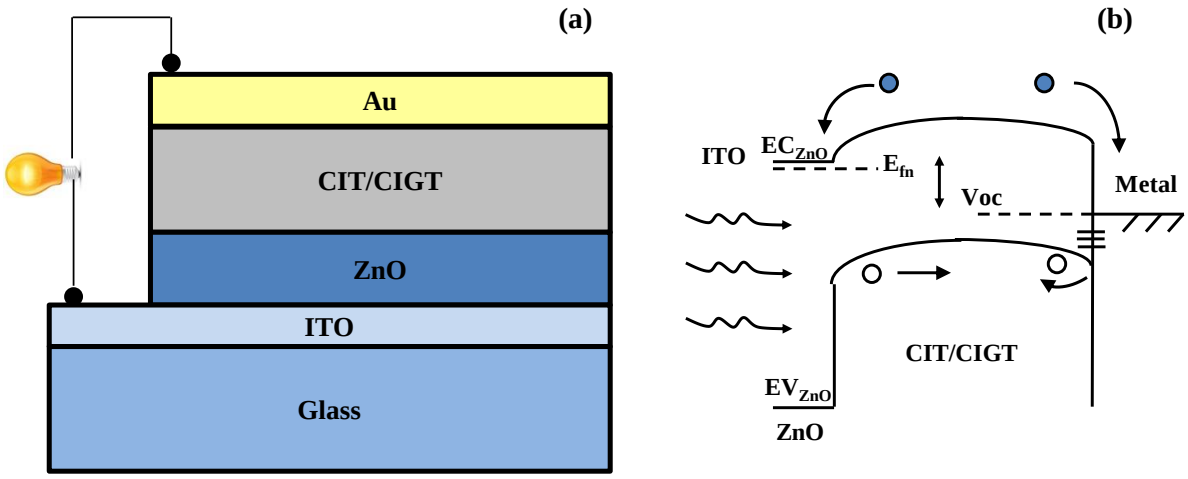


Figure 6.5: (a) Schematic of the solar cell structure ITO/ZnO/CIT or CIGT/Au and (b) device band structure under illumination. Holes meet the barrier height at the Au electrode, and electrons ca flow in either of two opposite directions to electrodes.

Fig. 6.6 displays the I-V characteristics of the ITO/ZnO/CIT/Au device in the dark and under illumination. EDT capped CIT nanosheets were chosen as the active layer due to the nanosheets ability to overlap hence forming a continuous network. Hence the expectation is that this type of nanostructure will result in a better performing device. The performance parameters of the CIT device are listed in Table 6.1. The obtained short circuit current (J_{SC}) and open circuit voltage (V_{OC}) values of the CIT are 0.49 mA/cm^2 and 880 mV. The high V*oc* can be attributed to the improved passivation of the defective nanocrystal surface [28]. The low (J_{SC}) suggests that there are high interface defects present causing recombination

loss especially at the back Schottky boundary between the CIT layer and the Au metal [25]. Despite achieving high open circuit voltage, a modest fill factor of (FF) of 0.60 and efficiency of 0.26% were recorded.

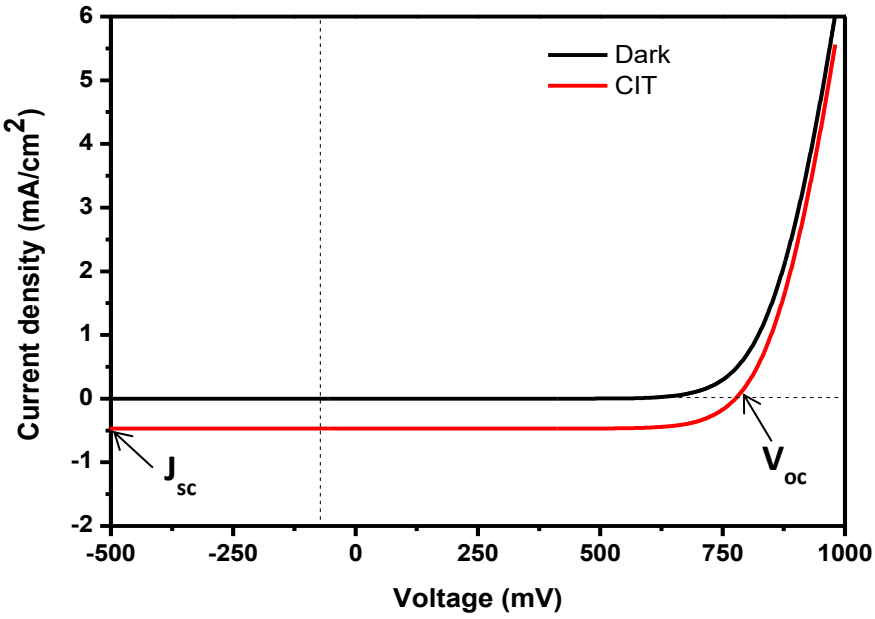


Figure 6.6: I-V curve of the EDT capped $CuInTe_2$ nanosheets.

Table 6.1: Solar cell parameters of the EDT capped $CuInTe_2$ nanosheets

Sample	V_{OC} (mV)	J_{SC} (mA/cm^2)	FF	Ƞ (%)
CIT	880	0.49	0.60	0.26

6.3.4 The effect of chemical surface treatment on the $CIGTe_2$ solar cell devices

Whilst the electron transfer capability of the active layer plays a decisive role in attaining high solar conversion efficiency, interface properties of a semiconductor are key to improving the performance of a device [26]. Charge transports in these systems occur by various mechanisms including electron tunnelling in which hopping distance is significantly small. Therefore, indicating that the inter-nanocrystal separation in deposited films is critical

for efficient charge transfer [26]. A number of studies have been conducted on how to adjust the inter-nanocrystal separation in deposited films [27, 28]. The use of short-chain organic cross-linking molecules have been reported to enhance the electrical and optical properties of nanostructured based thin films [29, 30]. The enhanced properties were attributed to the short inter-particle distance induced by replacement of long hydrocarbon chains with short chain surface ligands [26], therefore resulting in aggregation of the dispersed semiconducting nanocrystal layer [31]. In addition it altered the charge carrier concentration of the quantum dot film [32]. Klem and colleagues reported the use of ethanedithiol (EDT) molecules in the fabrication of PbS NC-based photovoltaic devices [32]. It was established that the EDT linkers enabled the fabrication of high quality nanocrystals films on textured, high surface area electrodes [32]. Furthermore power conversion efficiencies of 1.3% in the near-infrared was attained [32]. However, it was argued that the enhanced electrical transport between neighbouring PbS nanocrystals for deposited PbS nanocrystal/dithiol films was due to dithiol bridging or decreased inter-nanocrystal distance. In other studies high carrier mobility was reported for hydrazine-treated [26].

Different deposition approaches of thin film surface modification have been proposed [33-35]. In some studies surface modification was employed with particles capped with long-chain stabilizers, while others performed deposition of particles capped with short-chain ligands such as thioglycolic acid (TGA) and 3-mercaptopropionic acid (MPA) [34-36]. It was thought that direct deposition of aqueous quantum dots capped with short chain molecules simplifies fabrication of the device [33]. Mispelon et al. prepared ZnO nanocrystal films with 1,2-benzenedithiol added to ZnO nanocrystal dispersions and suggested it may be a simple method for preparing photoelectrodes for DSSCs with enhanced light scattering [34].

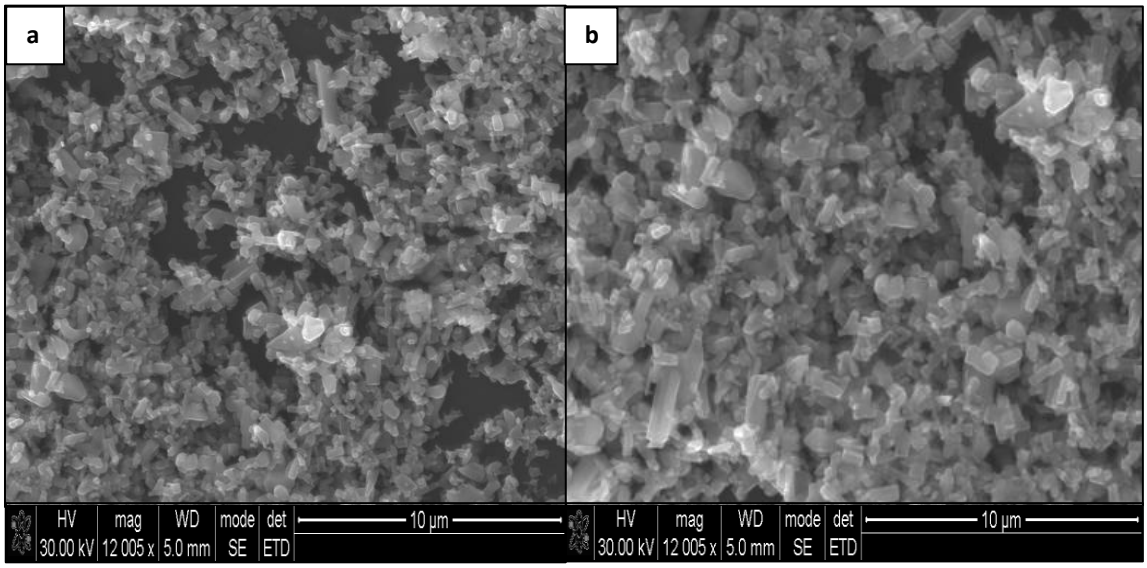


Figure 6.7: SEM images of the HDA capped $CuIn_{0.25}Ga_{0.75}Te_2$ synthesized using precursor 2 and EDT treated $CuIn_{0.25}Ga_{0.75}Te_2$ solar cells.

In this study, EDT treatment was done on the surface of CIGT film while the untreated films constitutes of the CIGT particles capped with OLA. The EDT treatment was done by spin coating film with 2% solution of EDT in acetonitrile. The scanning microscope (SEM) images of the treated and untreated films are presented in Fig. 6.7. The SEM images exhibit formation of voids in both treated and untreated films. However, the treated CIGT film has high packing fraction than those without treatment. It has been reported that overtreatment can lead to stress resulting in formation cracks [40]. In other studies formation of voids was attributed to reduced inter-particles space, in which more deposition was recommended to fill the voids to avoid pinholes and islands of isolated nanocrystals [32]. Literature shows that the sizes of thiols defined in terms of the S to S distance and the pK_a values determines the linking or bridge capabilities of these ligands [31]. The smaller the size and the lower the pKa value of the ligand, the greater the aggregation [31]. The ability of bifunctional thiols to trigger aggregation was reported by Mispelon [31]. In their study, they demonstrated that the addition of 1-hexanethiol did not significantly trigger aggregation of ZnO dispersion while

1,2-ethanedithiol immediately triggered aggregation of ZnO dispesion [31]. They further indicated that the ligand structure of the bifunctional thiols is essential, in that 1,2-benzenedithiol showed superior aggregation ZnO dispersions [31].

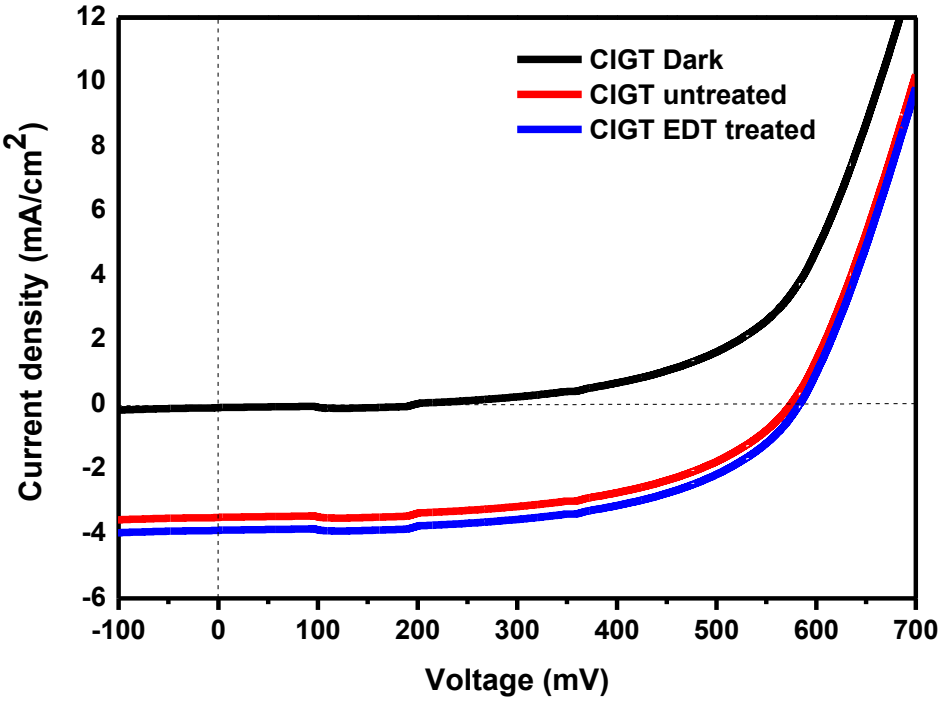


Figure 6.8: I-V curves of HDA capped $CuIn_{0.25}Ga_{0.75}Te_2$ synthesized using precursor 2 and EDT treated $CuIn_{0.25}Ga_{0.75}Te_2$ solar cells.

The electrical properties of the CIGT films were obtained and are presented in Fig. 6.8 and Table 6.2 summarizes the parameters from the I–V characteristics including the open circuit potential (V_{OC}), short-circuit current density (J_{SC}), fill factor (FF) and power conversion efficiency (η). The FF and Voc values of the EDT treated CIGT devices are lower than that of the CIT. The FF decreased from 0.60-0.55 while the Voc was reduced to 880 mV-578.27 mV. The decreased Voc may have resulted from the recombination at the interface. The Voc in the heterostructure device is not only determined by the difference in equilibrium junction potential but by the total recombination within the device [37]. As a result recombination at the interface significantly limits the Voc [38]. It was proposed that hole-injection barrier can

be corrected by choosing high work function metal which will minimize the hole injection barrier or establish a heavily p-doped surface layer in order to enable the tunnelling of holes through the barrier height [38].

Table 6.2: Solar cell parameters of HDA capped $CuIn_{0.25}Ga_{0.75}Te_2$ synthesized using precursor 2 and EDT treated $CuIn_{0.25}Ga_{0.75}Te_2$

Sample	V_{OC} (mV)	J_{SC} (mA/cm^2)	FF	Ƞ (%)
CIGT untreated	573.66	3.40	0.40	0.78
CIGT EDT-treated	578.27	3.92	0.55	1.25

The efficiency however increased significantly from 0.26-1.25% and high J_{SC} values (0.49-3.92 mA/cm^2) are obtained. The EDT treated CIGT devices showed superior performance in comparison to the untreated films. Superior performance of the treated device may be attributed to increased mobility of charge carriers with a decrease in the inter-particle distance. The space-filling network structure on the surface of the untreated devices is responsible for obtaining Voc of 573.66 mV and 3.40 mA/cm^2, suggesting that the mobility of charge carriers maybe disrupted thus poor performance.

5.2.5.2 The effect of thermal treatment on the $CIGTe_2$ thin films

It should be noted that the ligand exchange does not lead to reduction in inter-particle distance but also induces doping on the active layer [26]. However, thermal annealing promotes doping leading to change in the type of defects [26]. Other studies further showed that thermal annealing smoothies out the film surface and improve contact with the electrodes [26]. Doping the active layer leads to the formation of surface traps [26]. For example,

uncompensated surface ions (cations or anions) trapping free charge carriers act as donors if holes are trapped or as acceptors if electrons are trapped [26]. The degree and type of doping is imperative as it greatly influences the operation of the photovoltaic devices [26]. The difference between the number of hole- and electron trapping defects determines the degree of doping. The cu-poor n-type CIS becomes p-type could be converted to n-type by thermal treatment in a Se low-pressure environment [39]. This effect is believed to originate from the selenium vacancy acting like a donor [39]. Similarly n-type PbSe QD films changed to p-type conductivity upon thermal annealing [29]. It was thought that oxides on the surface of the QDs acted as p-type dopants [32].

However, the reports have shown that conventional furnace heating leads to doping impurity diffusion due to long cycle time [4]. Furthermore, it has high budget which increases costs in large diameter wafers [4]. On the other hand rapid thermal heating enables control of the annealing profile [4]. Miyazaki et al. reported efficiency increase of about 3.9% improvement from 7.3% to 11.2% for the CIGS thin film after rapid annealing treatment [40]. The performance enhancement was ascribed to the reduction of recombination at the CdS/CIGS interface [40]. Chung et al. found that the optical transmittance of CdS thin film had a slight increase at short wavelength after annealing [41]. The efficiency of the cell had about 0.6% absolute improvement from 15.87% to 16.47% when the annealed CdS/CIGS thin film was fabricated into a solar cell [41].

Although thermal treatments can be performed both prior to and after depositing the metallic electrode, post annealing showed much more improved efficiency [42]. Efficiency of CdSe QDs/PCPDTBT solar cells increased dramatically when thermal annealing was performed post deposition of aluminium cathode [42]. It was assumed that diffusion of aluminium may

have occurred or there are chemical reactions that happened during annealing which improved contact between the photoactive material and cathode [42]. In this study the fabricated films were annealed prior deposition of the Au electrode at temperature 300, 400 and 500 °C. The surface of the EDT treated and thermally treated films under SEM are shown in Fig. 6.9. From the SEM images, thermally treated films appear to be highly aggregated compared to the EDT treated films. Therefore, indicating the reduced inter-particle distance which will increase charge transport in the device. As the annealing temperature is increased to 400 and 500 °C, the surface of the films appear to be highly aggregated with voids. This indicates that high annealing temperatures promote the formation of voids. However, more studies are recommended to determine the type of defects present.

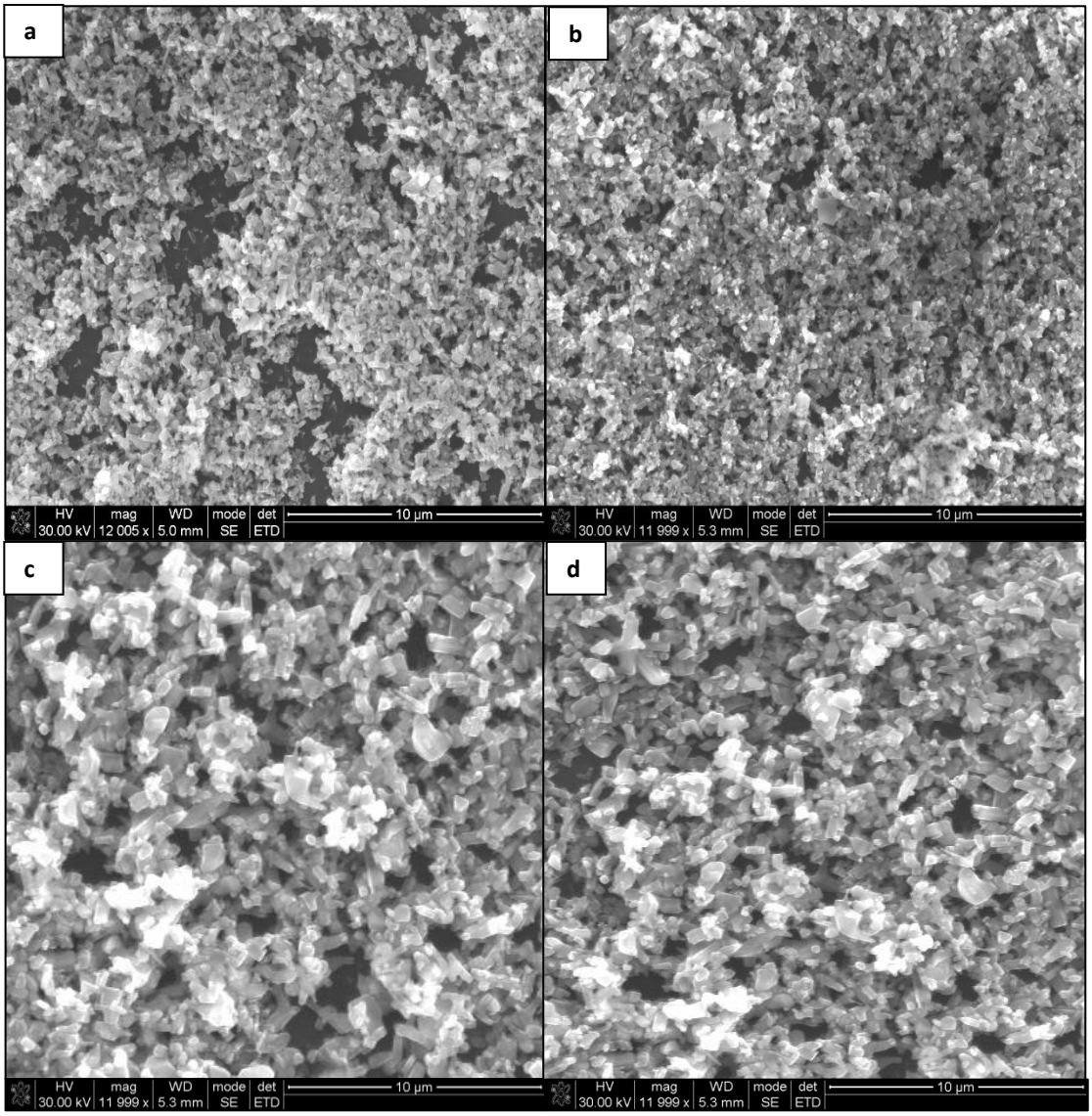


Figure 6.9: SEM micrographs of (a) EDT treated $CuIn_{0.25}Ga_{0.75}Te_2$ and annealed films at (b) 300, (c) 400 and (d) 500 °C.

To evaluate the effect of annealing treatment in the device, I-V measurements were conducted. Fig. 6.10 exhibit the I-V curves of the annealed devices at temperatures 300, 400 and 500 °C and are compared to the EDT treated device. Thermal annealing enhanced performance of the device with the highest efficiency of 2.14% was recorded for the device annealed at 300 °C. This suggests that thermal annealing reduces recombination. As the annealing temperature increases to 400 °C, the performance of the device begins to degrade

with the obtained efficiency of 1.20%. A further increase in annealing temperatures resulted in poor performance with the device annealed at 500 °C exhibiting the lowest efficiency of 0.089%.

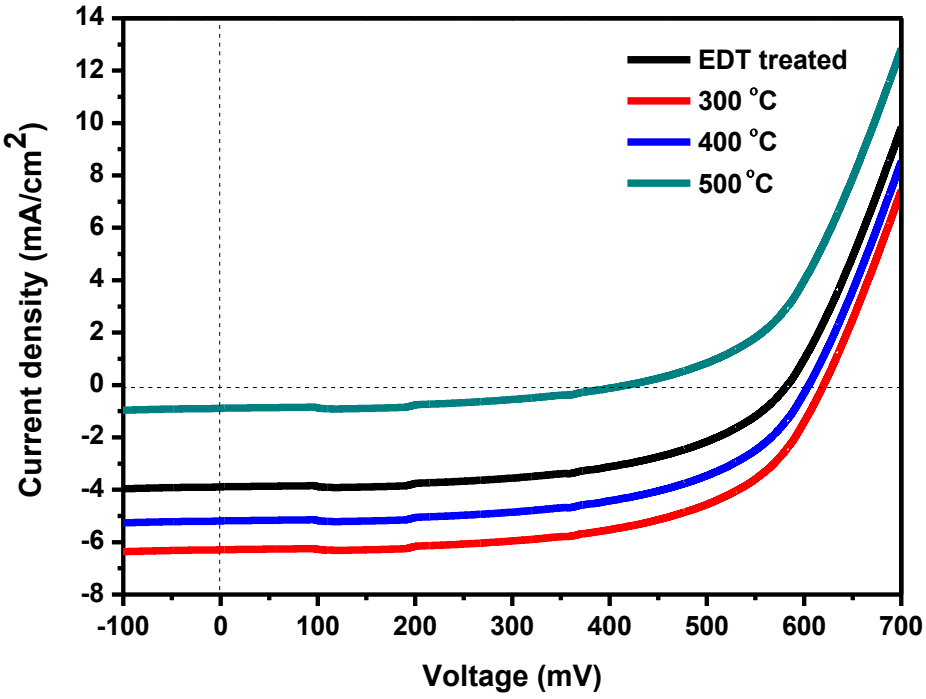


Figure 6.10: I-V curves of EDT treated $CuIn_{0.25}Ga_{0.75}Te_2$ and annealed films at 300, 400 and 500 °C.

Table 6.3: Solar cell parameters of EDT treated $CuIn_{0.25}Ga_{0.75}Te_2$ and annealed films at 300, 400 and 500 °C

Sample	V_{OC} (mV)	J_{SC} (mA/cm^2)	FF	Ƞ (%)
CIGT EDT-treated	578.27	3.92	0.55	1.25
Annealed at 300 °C	618.89	6.40	0.54	2.14
Annealed at 400 °C	600.81	5.27	0.38	1.20
Annealed at 500 °C	406.88	0.843	0.26	0.089

The decreasing efficiency trend with increasing temperature is shown in Fig. 6.11. Wi et al. attributed device performance degradation at high annealing temperatures to diffusion of Zn layer from the ZnO into the absorber layer in CIS or CIGS [43, 44]. More studies further demonstrated that in the CIGS devices diffuse out to the surface of the CIGS film [47]. It was understood that Ga prevents the Zn diffusion [47]. The Zn diffusion length in the CIGS film was shorter than that in the CIS film and these are some of the factors that contributes to the lower loss of efficiency in the CIGS solar cell at high temperature [45].

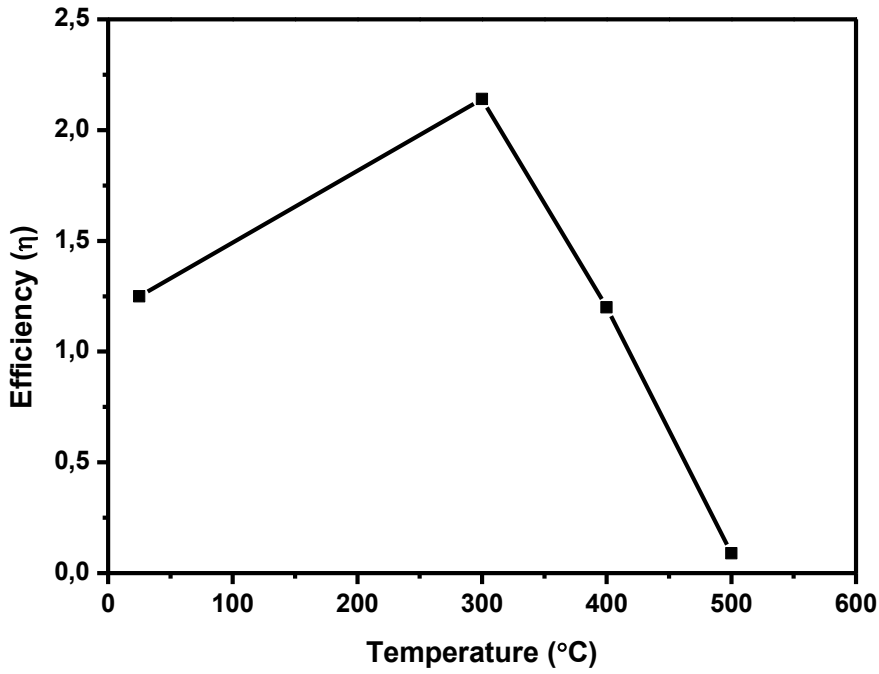


Figure 6.11: Efficiency trend for the annealed devices.

6.4 Conclusions

The colloidal CIGT and CIT nanocrystals can be applied to thin film photovoltaic devices. The HUMO and LUMO determined from CV measurements confirmed that the CIGT as an active layer can transfer the electrons to the ZnO n-type layer. A simple solution-processing approach allowed fabrication of both CIGT and CIT solar cell devices. The low efficiency of

0.26% was recorded for CIT devices though high Voc of 880 mV was achieved. The untreated untreated CIGT solar cell devices showed increased efficiency of 0.78% in comparison to CIT devices. The surface treatment through bifunctional thiol was necessary for in the CIGT devices for reducing inter-particle spacing hence increased aggregation on the surface. The EDT treated CIGT devices exhibited improved efficiency from 0.78-1.25% though the Voc decreased to 573.66 mV. Thermal treatment further enhanced the conversion efficiency of the device with the highest efficiency of 2.14% recorded for the device annealed at 300 °C. A further increase in annealing temperature resulted in loss of efficiency with the lowest being 0.0089% for the device annealed at 500 °C.

6.5 References

1. T. Zhang, Y. Yang, D. Liu, S. C. Tse, W. Cao, Z. Feng, S. Chen and L. Qian, *Energy & Environmental Science*, 2016, **9**, 3674-3681.
2. P. Jackson, D. Hariskos, E. Lotter, S. Paetel, R. Wuerz, R. Menner, W. Wischmann and M. Powalla, *Progress in Photovoltaics: Research and Applications*, 2011, **19**, 894-897.
3. T. Nakada, Y. Hirabayashi, T. Tokado, D. Ohmori and T. Mise, *Solar energy*, 2004, **77**, 739-747.
4. C. Dong-Sheng, Y. Jie, X. Fei, Z. Ping-Hua, D. Hui-Wei, S. Jian-Wei, Y. Zheng-Shan, Z. Yu-Hong, B. Bartholomeusz and M. Zhong-Quan, *Chinese Physics B*, 2013, **22**, 018801.
5. W. Wang, Y.-W. Su and C.-h. Chang, *Solar Energy Materials and Solar Cells*, 2011, **95**, 2616-2620.
6. R. Bhattacharya, W. Batchelor, J. Hiltner and J. Sites, *Applied Physics Letters*, 1999, **75**, 1431-1433.

7. D.-Y. Lee, S. Park and J. Kim, *Current Applied Physics*, 2011, **11**, S88-S92.

8. M. Park, S. Ahn, J. H. Yun, J. Gwak, A. Cho, S. Ahn, K. Shin, D. Nam, H. Cheong and K. Yoon, *Journal of Alloys and Compounds*, 2012, **513**, 68-74.

9. S.-p. Cu, *Progress in Photovoltaics*, 2013, **21**, 82-87.

10. Y. Oh, W. Yang, J. Kim, K. Woo and J. Moon, *ACS applied materials & interfaces*, 2015, **7**, 22570-22577.

11. K. Senthil, D. Nataraj, K. Prabakar, D. Mangalaraj, S. K. Narayandass, N. Udhayakumar and N. Krishnakumar, *Materials chemistry and physics*, 1999, **58**, 221-226.

12. J. F. Guillemoles, P. Cowache, A. Lusson, K. Fezzaa, F. Boisivon, J. Vedel and D. Lincot, *Journal of applied physics*, 1996, **79**, 7293-7302.

13. V. Alberts, J. Bekker, M. Witcomb, J. Schön and E. Bucher, *Thin Solid Films*, 2000, **361**, 432-436.

14. A. M. Gabor, J. R. Tuttle, D. S. Albin, M. A. Contreras, R. Noufi and A. M. Hermann, *Applied Physics Letters*, 1994, **65**, 198-200.

15. T. Dullweber, O. Lundberg, J. Malmström, M. Bodegård, L. Stolt, U. Rau, H.-W. Schock and J. H. Werner, *Thin Solid Films*, 2001, **387**, 11-13.

16. A. Chirilă, S. Buecheler, F. Pianezzi, P. Bloesch, C. Gretener, A. R. Uhl, C. Fella, L. Kranz, J. Perrenoud and S. Seyrling, *Nature materials*, 2011, **10**, 857-861.

17. M. Islam, A. Yamada, T. Sakurai, S. Ishizuka, K. Matsubara, S. Niki and K. Akimoto, *Advances in OptoElectronics*, 2011, **2011**.

18. J. Chang and E. R. Waclawik, *RSC Advances*, 2014, **4**, 23505-23527.

19. J. Y. Kim, O. Voznyy, D. Zhitomirsky and E. H. Sargent, *Advanced Materials*, 2013, **25**, 4986-5010.

20. O. Aissaoui, S. Mehdaoui, L. Bechiri, M. Benabdeslem, N. Benslim, A. Amara, A. Otmani, K. Djessas and X. Portier, *Journal of Luminescence*, 2011, **131**, 109-113.

21. M. Leon, R. Diaz, F. Rueda and M. Berghol, *Solar energy materials and solar cells*, 1992, **26**, 295-307.

22. O. Aissaoui, L. Bechiri, S. Mehdaoui, N. Benslim, M. Benabdeslem, X. Portier, H. Lei, J.-L. Doualan, G. Nouet and A. Otmani, *Thin Solid Films*, 2009, **517**, 2171-2174.

23. L. Leonat, G. Sbârcea and I. V. Branzoi, *UPB Sci Bull Ser B*, 2013, **75**, 111-118.

24. Ş. Antohe, *Materiale si dispozitive electronice organice*, Editura Universitatii Bucuresti, 1996.

25. M. P. Kalenga, University of the Witwatersrand, 2015.

26. L. Nikolenko and V. F. Razumov, *Russian Chemical Reviews*, 2013, **82**, 429.

27. E. J. Klem, D. D. MacNeil, P. W. Cyr, L. Levina and E. H. Sargent, *Applied physics letters*, 2007, **90**, 183113.

28. J. M. Luther, M. Law, Q. Song, C. L. Perkins, M. C. Beard and A. J. Nozik, *ACS nano*, 2008, **2**, 271-280.

29. D. V. Talapin and C. B. Murray, *Science*, 2005, **310**, 86-89.

30. D. Yu, C. Wang and P. Guyot-Sionnest, *Science*, 2003, **300**, 1277-1280.

31. A. Mispelon, J. Yan, A. H. Milani, M. Chen, W. Wang, P. O'Brien and B. R. Saunders, *RSC Advances*, 2015, **5**, 18565-18577.

32. E. J. Klem, H. Shukla, S. Hinds, D. D. MacNeil, L. Levina and E. H. Sargent, *Applied Physics Letters*, 2008, **92**, 212105.

33. X. Lin, C. Wang, S. Xu and Y. Cui, *Journal of Physics D: Applied Physics*, 2013, **47**, 015103.

34. D. F. Watson, *The Journal of Physical Chemistry Letters*, 2010, **1**, 2299-2309.

35. C. Luan, A. Vaneski, A. S. Susha, X. Xu, H.-E. Wang, X. Chen, J. Xu, W. Zhang, C.-S. Lee, A. L. Rogach and J. A. Zapien, *Nanoscale Research Letters*, 2011, **6**, 340.

36. *Chemistry Letters*, 2007, **36**, 712-713.

37. B. A. Gregg and M. C. Hanna, *Journal of Applied Physics*, 2003, **93**, 3605-3614.

38. J. Gao, J. M. Luther, O. E. Semonin, R. J. Ellingson, A. J. Nozik and M. C. Beard, *Nano letters*, 2011, **11**, 1002-1008.

39. H. Neumann and R. Tomlinson, *Solar Cells*, 1990, **28**, 301-313.

40. H. Miyazaki, R. Mikami, A. Yamada and M. Konagai, *Japanese journal of applied physics*, 2004, **43**, 4244.

41. Y.-D. Chung, D.-H. Cho, N.-M. Park, K.-S. Lee and J. Kim, *Current Applied Physics*, 2011, **11**, S65-S67.

42. Y. Zhou, M. Eck, C. Veit, B. Zimmermann, F. Rauscher, P. Niyamakom, S. Yilmaz, I. Dumsch, S. Allard and U. Scherf, *Solar Energy Materials and Solar Cells*, 2011, **95**, 1232-1237.

43. J.-H. Wi, T. G. Kim, J. W. Kim, W.-J. Lee, D.-H. Cho, W. S. Han and Y.-D. Chung, *ACS applied materials & interfaces*, 2015, **7**, 17425-17432.

44. J. H. Wi, W. J. Lee, D. H. Cho, W. S. Han, J. H. Yun and Y. D. Chung, *physica status solidi (a)*, 2014, **211**, 2172-2176.

45. J.-H. Wi, D.-H. Cho, W.-J. Lee, W. S. Han and Y.-D. Chung, *Solar Energy*, 2016.

Chapter 7: Conclusions and Recommendation

7.1 Conclusions

Chapter 2: showed various types of Cu-based chalcogenide semiconductor materials. The most intriguing part was how colloidal synthesis enabled fine-tuning of the optical and electrical properties of the materials. Achieving high-quality Cu chalcogenides nanostructures through colloidal synthesis entailed careful control of parameters such as reaction temperature, reaction time, use of capping agents, precursors, and variation in stoichiometry. Through monitoring reaction parameters, high-quality nanostructures of different size and morphology can be obtained. The sizes of these materials are directly linked to the band gap. The ability to engineer or tune electrical and optical properties of these materials makes the desirable for applications in solar cells.

Chapter 3: Colloidal method was employed to synthesize ternary $CuInTe_2$ nanocrystals. It was established that reaction temperature was imperative as the semiconductor materials could not be attained at temperatures lower than 250 °C. However, the formation of binary impurities was evidenced at 250 °C, suggesting that formation of pure $CuInTe_2$ follows a certain crystallization mechanism. By changing the order of precursor addition, pure $CuInTe_2$ nanocrystals were obtained. Based on the order of precursor addition it was established that crystallization of pure $CuInTe_2$ follows HSAB principle.

Chapter 4: The use of various capping agent resulted in the formation of different morphologies of $CuInTe_2$. Morphology varied from rods, cubes, conical branched structures and hexagonal sheets. The optical properties varied with morphology with the highest optical band gap of 1.22 eV measured for 1D rods. A change in reaction time resulted in morphology transition from 1D rods to 3D hexagonal sheets. It was postulated that morphology evolution occurs through the self-ripening mechanism.

Chapter 5: colloidal synthesis of quaternary $CuIn_{1-x}Ga_xTe_2$ nanocrystals was achieved through the use of different precursors. However, precursor 2 gave pure $CuIn_{1-x}Ga_xTe_2$ nanocrystals. By varying reaction time while utilizing precursor 2 band gap of the material changed. The high band gap was measured at low reaction time and it was linked to small sized particles. A change in the stoichiometry of In and Ga enhanced the optical properties of the material. The improved optical properties could be attributed to reduced lattice parameters resulting from a partial substitution of In atoms with small Ga atoms. However, the intended concentration of In and Ga varied from the actual concentration resulting from a loss of material during synthesis. Formation of impurities was evidenced upon changing capping agent from DDT to HDA. The HDA capped particles exhibited band gap of 1.80 eV which is close to that of DDT capped particles. This was attributed to small sized particles obtained with HDA.

Chapter 6: the hybrid ZnO/CIT and ZnO/CIGT solar cell devices were fabricated through a solution process approach. High Voc of 880 mV was obtained for CIT devices but low efficiency of 0.60 % was recorded. There was an improvement in efficiency from 0.26-0.78% but the Voc drastically decreased from 880 to 578.27 mV, suggesting there is high interface recombination in the CIGT devices. Surface modification through ligand exchange was necessary for reducing the inter-particle distance thus improving the mobility of charge carrier. This was clear from the improved performance in which the efficiency increased from 0.78% for the untreated CIGT devices to 1.25% for the treated devices. Thermal treatment further enhanced the efficiency to 2.14% for devices annealed at 300 °C. A further increase in annealing temperatures lead to the deterioration of the performance of the device with the lowest efficiency of 0.089% recorded at 500 °C, attributed to the leaching of In and Ga to the ZnO layer.

7.2 Recommendations

It is recommended that synthesis of $CuIn_{1-x}Ga_xTe_2$ with more capping agents be explored to achieve various morphologies which may be beneficial for solar cell devices. Synthesis of $CuIn_{1-x}Ga_xTe_2$ should be conducted at various reaction time particularly low reaction times as it could result in decreased particle size thereby enhancing the optical properties of these materials. Optimization of heterojunction ZnO/CIT and ZnO/CIGT devices is highly recommended as it may improve device performance. The use of other bifunctional thiols should further be explored as high surface aggregation may be established resulting in more reduction in inter-particle spacing. Thermal treatments post-Au deposition should be conducted as it may increase metal contact between the active layer and Au, resulting in reduced recombination and high charge carrier mobility. Other n-type semiconductors such as TiO_2 and different metal contacts should be explored.